Characterization of Soft Gels with 2P Microrheology, a Novel, Active Paired-Particle Method

Dissertation

Presented in Partial Fulfillment of the Requirements for the Degree Doctor of Philosophy in the

Graduate School of the Ohio State University

By

David Gutschick, M.S.

Materials Science and Engineering

The Ohio State University

2018

Dissertation committee:

Heather Powell, Advisor

Peter Anderson, Co-Advisor

Gregory Lafyatis

Abstract

The mechanics of a material will deviate from macroscopic values as the probe length scale approaches that of structural features in the material. This divergence of properties at small length scales can have major implications, such as for inter-cell communication in bio-matrices. Microrheology is well-situated to measure micromechanics in soft materials, but the state of the art has not been developed sufficiently to fully characterize micromechanics. This dissertation presents 2P active microrheology, a novel method to measure the micromechanics of soft gels versus particle separation distance. Findings from use of the 2P method are shown for polyacrylamide gels, agarose gels, and collagen gels with and without addition of non-collagenous proteins. These findings include previously unobserved relationships to single-particle microrheology and macroscopic results.

Acknowledgements

I would like to thank:

- My wife, Yi Li, for helping me work through technical challenges and providing support at key times.
- Dr. Heather Powell for actively participating in experimental work, for moderating the interactions of the project group, and work working tirelessly to never be the weak link.
- Dr. Peter Anderson for providing a theoretical perspective and constantly striving for physically insightful models and understanding of mechanisms.
- Dr. Gregory Lafyatis for providing advice on subtleties of optical traps and for support to complete the project.
- Tyler Heisler-Taylor for developing the LabVIEW code used to operate the optical trap apparatus, and for first teaching me the methodology of optical trap measurements.
- David Yeung, Ph.D., for his collaboration in data taking and for helping troubleshoot the optical trap apparatus.
- Vasile Negrescu, Kevin Buno, Kim Lachell, and Chuanzhe Hu for working with me as undergraduate assistants.
- The members of Dr. Powell's group for addressing my frequent requests for experimental advice and the location of obscure lab equipment/supplies.
- The member of Dr. Anderson's group for help in making and modifying finite element models with ABAQUS.

Vita

2008 ..... B.S in Mechanical Engineering

California Institute of Technology

2014 ..... M.S. in Materials Science and Engineering

The Ohio State University

2014-Present..... Ph.D. Candidate in Materials Science and Engineering

The Ohio State University

Fields of Study

Major Field: Materials Science and Engineering

Table of Contents

List of Tables

List of Figures

Chapter 1 : Introduction

Intersection of Biology and Materials Science

Many tissues within the body provide a mechanical function from protecting our internal organs to facilitating motion. While the macroscopic mechanical properties of tissues like bone and muscle have been studied for centuries, the importance of microscale mechanics, specifically within the extracellular matrix, have more recently been discovered to play a significant role in tissue development and maintenance. The mechanical environment immediately surrounding a cell has been shown to control cell differentiation and communication. For example, high levels of local matrix stiffness have been associated with osteogenic differentiation.[1] Additionally, models of inter-cell communication through stress transmission have suggested that such communication over greatly increased distances in biological matrices is a result of the fibrillar networks in those matrices.[2] Though the ability to assess the biological outcomes of different mechanical environments is fairly advanced, most studies rely on macroscale techniques to assess the mechanical properties of the surrounding matrix despite the local (i.e. meso to microscale) nature of the problem.

The micromechanics of materials, especially natural materials like the extracellular matrix, can be very different than macroscopic mechanics of the same material. Structural features and their relative length scales can lead to behavior inconsistent with macroscopic constitutive models. For example, macroscopic mechanical analyses of collagen hydrogels fail to predict behaviors at the microscopic level. Microscopically, cells cultured within or on top of collagen gels were found to communicate mechanically over distances much greater than was possible between cells of the same type on/in homogenous, linear elastic gels like polyacrylamide (PAA).[3–

[5] Models of cells contracting on top of hyperelastic gels, which qualitatively match strain stiffening observed in macroscopic analyses of collagen gels, showed little change in potential mechanotransductive communication distance.[6] However, when models were made with a network of discrete, interconnected fibrils, stress and strain localization greatly increased the maximum distance over which mechanotransductive communication could potentially be achieved.[5,7] Images of collagen gels with aligned, densified regions between cell clusters (Figure 1.1) corroborated this explanation of long distance communication, as did the disintegration of those cell clusters when those densified regions were severed.[8] Despite numerous reports indicating the importance of local matrix properties, experimental data collected at the microscale has been very limited. Unfortunately, few methods are available for advanced micromechanical characterization within the undisturbed interior of soft materials.

Figure 1.1: Images of collagen gels with aligned, densified regions forming between mammary acini over the course of 24 hours.[8]

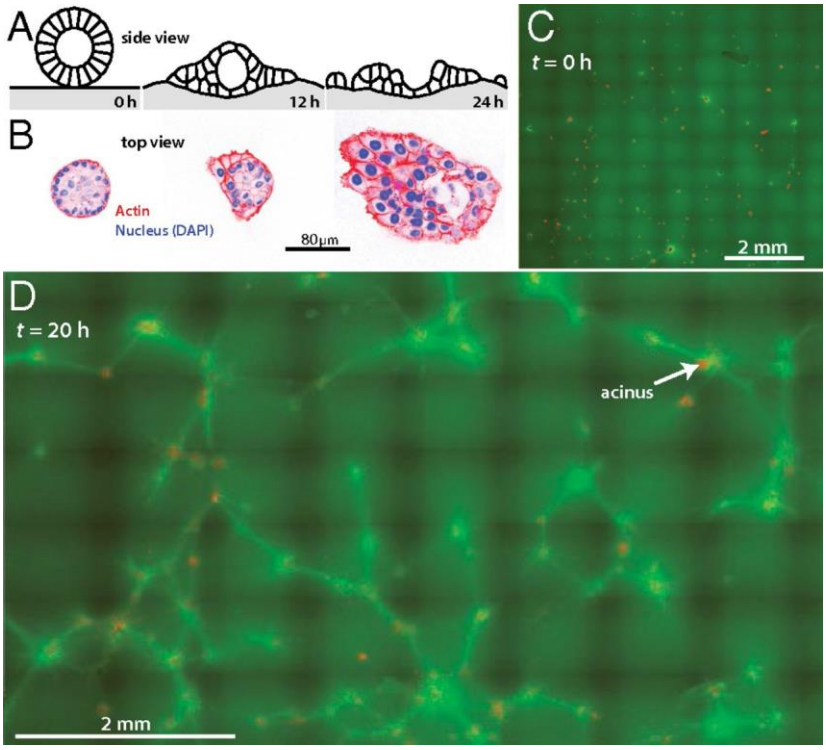

Micromechanical characterization methods

Though a range of micromechanical characterization techniques exist for surface micromechanical analysis, almost none are able to probe micromechanics in the interior of a 3D matrix. Atomic force microscopy, for example, is a mature method for micromechanical characterization, yet is limited to probing the surface of a matrix, which may have different properties than the interior.[3] To facilitate analysis of the interior, gels may be cut into cross-section and subsequently assessed. Unfortunately, the sectioning process can induce damage to the structure and skew outcomes. Some knowledge of fibril mechanics has been obtained through micro tensile tests of individual fibrils, but it is difficult to combine this knowledge with other existing methods to

fully define local micromechanics of the matrix.[9] Thus a technique that can directly probe mechanical properties within a 3D matrix with minimal disturbance to the microstructure is needed.

State of the art in microrheology

Microrheology is the study of mechanics within liquid and soft solids through the active or passive motion of microscale probe particles. Over the course of almost 100 years, microrheology has advanced from basic studies of protoplasm mechanics using iron filings and a magnet to a field of research capable of examining aspects of molecular dynamics and complex microstructures.[10–12] The majority of recent studies utilize passive particle motion, measuring displacements resulting from thermal fluctuations in the material of interest. Microrheology is often referred to as a passive, thermal method, ignoring the branch of the field in which dynamic force is applied in a control manner to probe particles.[13] Although active microrheology, using optical or magnetic driving forces, constitutes a very small fraction of microrheological work, it has the capability to more fully characterize micromechanical properties of soft materials including recent discoveries demonstrating the relationship between collagen fibril density and local modulus (Figure 1.2), and anisotropic and nonlinear force-displacement response of beads embedded in collagen gel (Figure 1.3).[14,15] Passive microrheology methods rely on uncontrolled sub-pN forces of passive methods which typically lead to requirements of ~1 million time points to obtain a single data point, thus the research presented here focuses on active microrheology.[16]

Figure 1.2: Shear storage and loss moduli versus local density of collagen fibrils.[14]

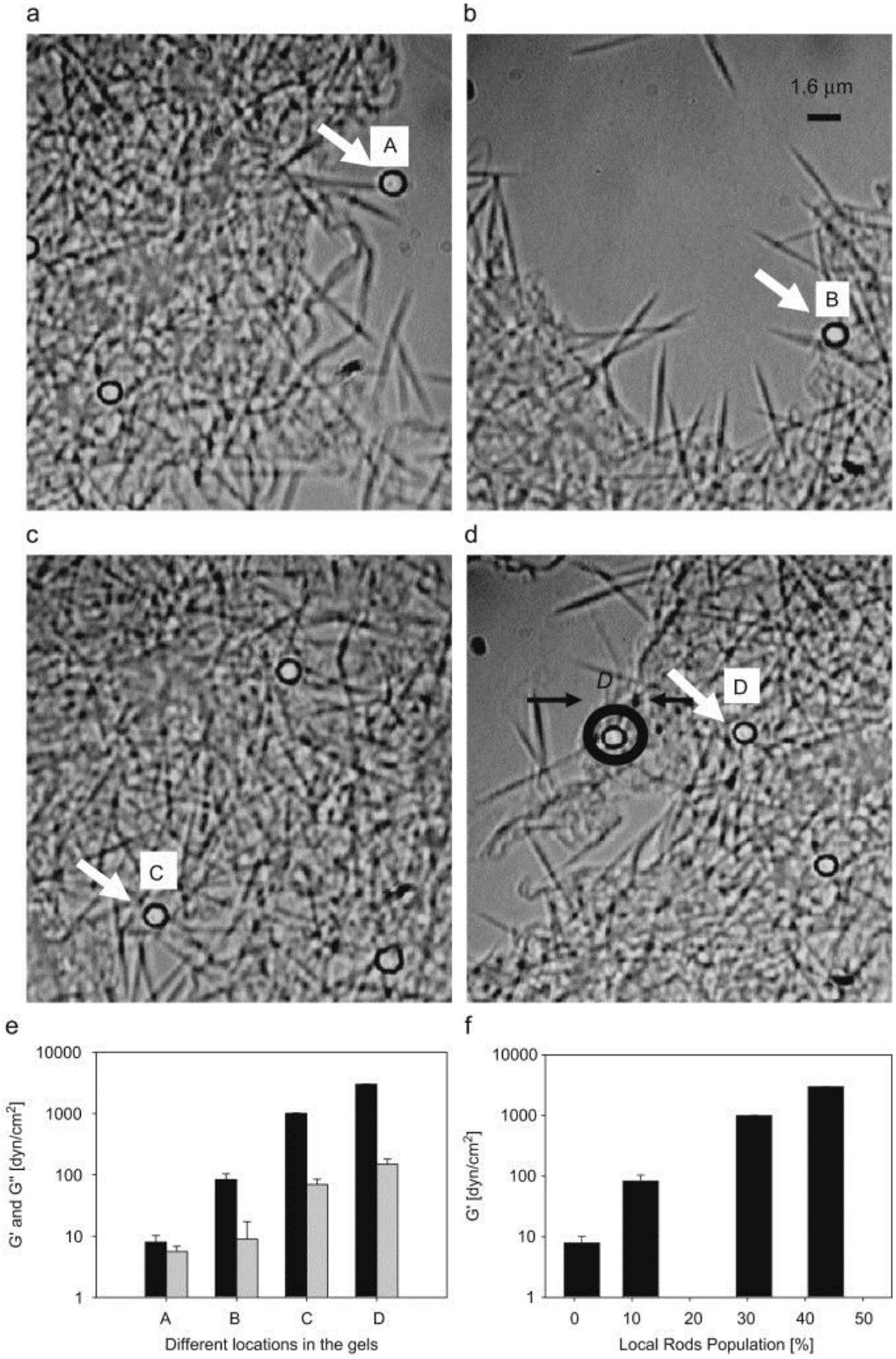

Figure 1.3: Trajectory maps of a bead embedded in collagen with displacement of an optical trap equal magnitudes at equally spaced angles.[17]

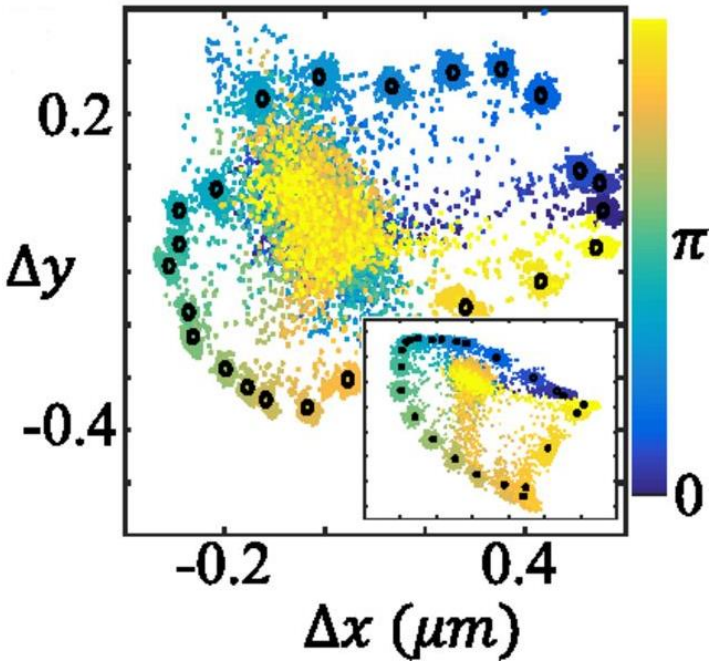

Single Particle versus Multi-particle Active Microrheology

Dynamic control over a probe embedded within a material makes active microrheology uniquely well-suited for probing micromechanics inside of 3D matrices like collagen gels, but its use in characterization of these types of materials has been limited. A major, but entirely self-imposed, limitation has been a widespread preference for single-particle microrheology (SPMR), rather than multi-particle microrheology (MPMR). In SPMR, the only particle observed is the particle to which force is being applied. Perhaps the most severe drawback to SPMR is that there are frequently interface effects between the particle and material which bias any measurements taken. Local alteration in materials properties surrounding the bead were reported almost 20 years ago.[16,18] This issue can be avoided through use of MPMR, in which particles beyond the one being

driven are observed. Figure 1.4 is a schematic illustration of the difference between SPMR and MPMR. In addition to producing measurements insensitive to the interface effects which undermine SPMR measurements, a prototype MPMR method was used by Schmidt et al. in 1996 to make basic measurements of Poisson's ratio, which is impossible with SPMR.[11] Unfortunately, the demonstration of MPMR's ability to collect an expanded set of mechanical data, did not lead to extensive use of MPMR. Possible reasons for the lack of adoption may include that the driving source was magnetic and thus indiscriminately applied force to every ferromagnetic particle in the sample. In addition, magnetically induced MPMR required physically rotating the sample within a cumbersome array of magnetic coils to define the elastic constants of an isotropic material. Though not widely adopted following its development, the MPMR methodology described by Schmidt *et al.* represented a significant advance in micromechanical measurement allowing quantification of properties not possible with single-particle practitioners.

Figure 1.4: Conceptual schematic of single-particle microrheology (SPMR) versus multi-particle microrheology (MPMR). In both methods, bead displacement is related to force applied to a single particle to determine material properties. However, in SPMR, the force and displacement being related are for the same bead, while in MPMR the force is applied to one bead and the displacement of another bead is measured.

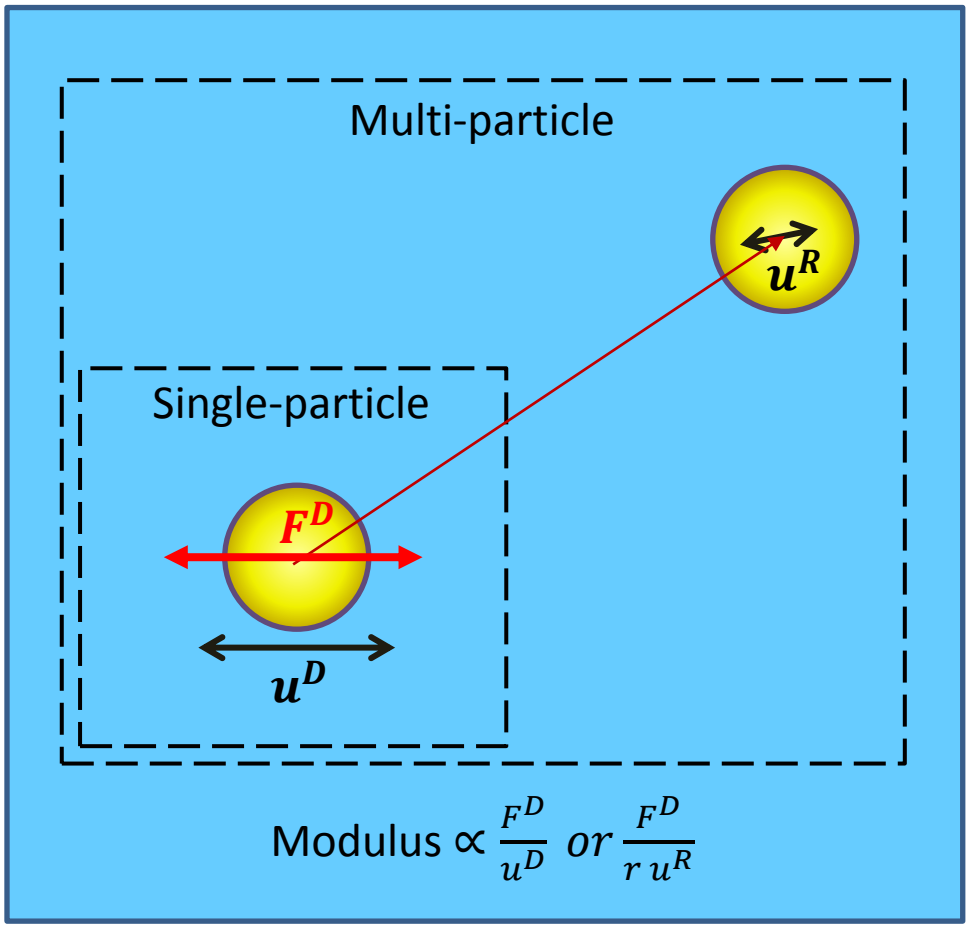

Advances in Multi-particle Microrheology

The seminal work by Schmidt et al. provided the framework for MPMR however the use of magnetically driven beads was significantly challenging. Optical trapping provides a more flexible methodology for applying a force on the beads within the matrix because: it does not require the sample to be surrounded by magnets, because 2D trap steering is achieved by adding widely available steered mirrors to the beam path, and because driven

beads can be individually chosen by the operator. The type of optical trapping relevant to microrheology involves focusing a laser beam through a high numerical aperture lens such that the beam waist intersects a dielectric sphere (bead), as shown in Figure 1.5.[19–21] Roughly speaking, the bead is pulled toward a point along the beam axis slightly past the waist essentially as if the bead center was connected to that point by a linear spring over a limited range of bead-trap offsets. The trap can be steered in two or three dimensions with readily available optical hardware inserted into the beam path to make a system which can precisely apply a controlled force vector to a single, chosen probe bead within a gel, and with no need for the cumbersome arrangement of magnetic coils involved in magnetic microrheometry. One drawback is that the peak forces applied by optical traps are smaller than what can be applied in magnetic microrheology, usually on the order of 10 pN. The desire to stay within the limited span of linear force versus bead-trap offset, commonly assumed to extend about 100 nm in either direction limits the magnitude of applied force; however, improvements in trap force calibration could allow significantly greater magnitudes of applied force and thus bead displacement. Additionally, a switch to optical trap microrheology allows a single chosen bead to be driven in 2D using mirrors along the trap beam path, and a method for mapping the trap force at higher bead-trap offsets would allow application of larger peak forces.

Figure 1.5: Schematic of a dielectric bead in a gradient force optical trap. The bead is in an energy well centered along the beam axis just past the beam waist. Any displacement of the bead relative to this point is "climbing" the energy well, resulting in a force pulling the bead back towards the trap center.

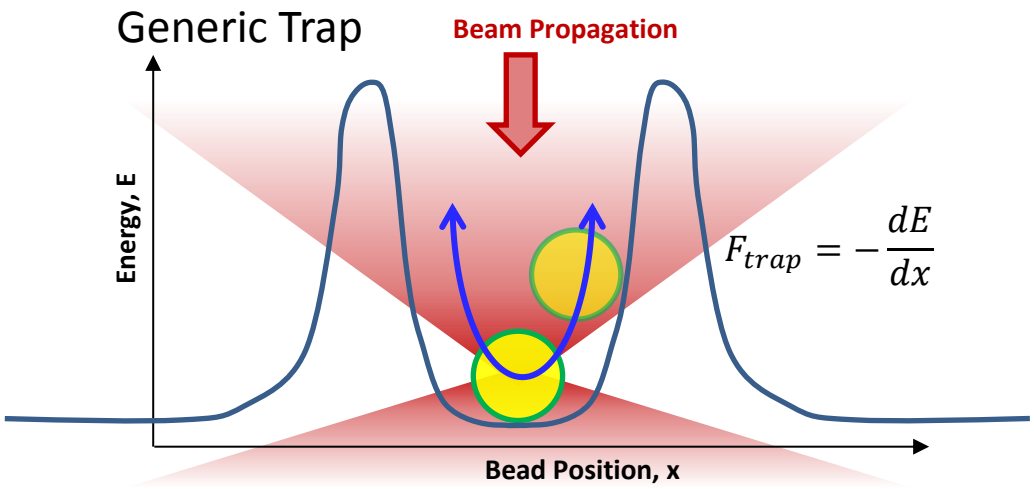

In most MPMR studies, beads have been tracked using a centroid tracking algorithm which identifies a rough position for each bead in each frame, and computes the brightness centroid of a circular region around that position to determine the location of that bead in that frame. This algorithm, described by Crocker and Grier in 1996, has been shown to have lower precision than other particle tracking methods For MPMR, receiver bead displacements fall off rapidly with distance, making precision in bead tracking a key determinant of performance. A more precise method, such as an optimized variant of the correlation method tested by Cheezum *et al.*, could maximize performance with distant beads and limited peak force amplitude.[22] A high force optical trap with optimized displacement measurements represents a major opportunity for producing high quality data from which to extract micromechanical properties.

New Optical Platform for Robust MPMR

Presented in this document are: the 2P optical trap microrheology method which provides a host of micromechanical properties using a high force optical trap; the innovations necessary to create that method; and novel results from use of the method. Several key innovations are briefly described in Table 1.1. A method for mapping trap force across a larger span of bead-trap offsets provides precise knowledge of force at larger offsets than is traditionally used, allowing larger trap displacements to be used for generation of larger forces while maintaining a known force amplitude. Use of a CCD camera allows multiple beads to be tracked simultaneously, enabling 2P data collection in addition to the inherently available single-particle (1P) data. Star driving, in which force is successively applied to a single "driven" bead in several directions, provides a variety of 2D force vectors from which a 2D relationship can be established for distant "receiver" bead displacement versus force on the driven bead. The relationships are expressed as "coupling matrices", from which material mechanical properties can be directly obtained. Generation of full Fourier spectra for bead displacement with sinusoidal driving force application provides not only the strong noise rejection of Fourier analysis, but also information about nonlinearity through harmonics and uncertainty in amplitude values via analysis of non-harmonic frequencies. As Fourier analysis can provide phase information, phase lag between force application and bead displacement can be used to define viscoelasticity. All of the properties available from use of these innovations can then be plotted against bead separation to provide information about length scale-related effects, such as the strain localization of collagen gels which greatly enhances inter-cell communication. Finally, numerical models were used to probe and quantify the interface effects causing bias in single-particle measurements. Taken together, the host of advancements creates a powerful method capable of quantifying many mechanical properties versus bead separation.

Table 1.1: Key innovations made in the development of the 2P method.

Innovation	Description	Impact
Trap force mapping	A method was developed to quickly map optical trap force over a large span of bead-trap offsets.	Specifies the force applied at any trap-bead offset. Allows quantification of nonlinearity in trap shape and/or extraction of an effective spring constant.
Large optical trap displacements	The use of large optical trap displacements to generate large bead displacements.	Larger bead displacements at a given laser power increase the signal-to-noise ratio.
Simultaneous 1P and 2P	The simultaneous collection of 1P & 2P data.	Allows comparison of the two data types for each sample and sample type.
Star driving	Star driving is the process of incrementing the angle of force applied to a driven bead.	Observing X and Y bead displacement with varied ratios of X and Y force enables quantification of a 2D relationship between force and bead displacement.
Generation of full Fourier spectra	Generation of full Fourier spectra with phase information for bead displacement along each axis while using sinusoidal force application.	Harmonics allow quantification of nonlinearity, which enabled detection of soft sheaths around beads. Non-harmonic frequencies allow quantification of displacement noise.
Force-displacement coupling matrices	Definition of a force-displacement coupling matrix for each driver-receiver bead pair.	These matrices fully define isotropic viscoelastic material properties, anisotropic orientation and magnitude for 1P data, and could be used to define anisotropic material orientation and properties.
Viscoelastic characterization	Viscoelasticity was quantified in 1P and 2P data through phase lag with respect to the trap force, including phase lag dependence on force-displacement coupling mode.	Complex modulus is the standard result of microrheology, but dependence of viscoelastic constants on whether the coupling mode is direct or transverse has not been studied before, to the author's knowledge.
Material properties versus bead separation	Examination of all measured properties versus bead separation.	Exposes length scales of heterogeneity through trends in the mean value or scatter of each value.
Sheath models	Numerical models of a (visco)elastic medium containing a bead encased in a soft or stiff sheath.	These models allowed predictions of the properties of sheaths which are known to bias G in 1P data.

Chapter 2 : The Foundation and Goals for 2P Active Microrheology

The purpose of this chapter is to provide a reference point for the advances made in developing the 2P method and describe the goals which drove its development. The foundation was an inherited apparatus and an incomplete microrheology method, both of which were modified and added to in the development of the 2P method. Properties of the inherited method are highlighted in Table 2.1, highlighting both positive features and shortcomings which needed to be addressed during development. Goals for the method were shaped by the multi-particle nature of the inherited method and shortcomings identified in other methods within the literature.

Foundation for the 2P active microrheology method

The 2P method was built off of an inherited foundation comprised of a physical apparatus with associated computer programs and a method. The inherited method measured bead displacement associated with either: force applied to a bead embedded in a gel via periodic displacement of an optical trap; or from stage displacement applying drag force to a bead in a stationary trap in water. CCD videos of the bead displacement were reduced into position lists by the correlation method of particle tracking. The method defined an effective spring constant for the trap force versus bead-trap offset, but was not yet capable of reporting material properties using the relationship between trap force and bead displacement within a gel. Microrheology with active laser trapping had been chosen for the precise control of applied force to the probe beads, and for the

large signal-to-noise ratio compared to passive methods. A single beam trap had been chosen as extra traps would complicate the analysis of bead displacement within the gels without providing a clear benefit. Finally, the correlation method of particle tracking was chosen because it was shown to have lower noise than the more widely-used centroid tracking described by Crocker and Grier.[22,23] There are many other variants of microrheology with some differentiators including thermal versus active force application, magnetic or optical trapping, single particle, paired particle or statistical ensemble bead displacement, and photodiode, centroid, or correlation particle tracking.[24] The inherited apparatus and method represent a single variant of microrheological methodology and apparatus, with each aspect chosen for the characterization of comparatively stiff gels using paired particles.

As a totality, the inherited method drove an individual bead in a gel sample through the periodic displacement of an optical trap with calibrated force, and produced a final product of Fourier spectra defining X and Y displacement for each bead (both drive and non-driven) within a chosen field of view. The inherited system primarily consisted of the optical trap apparatus (Figure 2.1) combined with LabVIEW, μ-Manager, and MATLAB code to operate the apparatus and analyze the resulting data.[25] Three LabVIEW programs were provided, the first for controlling the apparatus during force calibration experiments, the second for centering the trap on a chosen bead within a gel, and the third for generating oscillatory displacement of the trap. A corresponding μ-Manager configuration file enabled video capture during both types of trials. Finally, a MATLAB script analyzed the resulting videos and logs from LabVIEW to calculate bead positions and time stamps for each video frame, from which it generated a Fourier spectrum with phase information for each bead along both the X and Y directions. Taken together, the inherited components provided abilities for calibration of trap force, driving beads in gel samples, and obtaining bead displacement data which would be necessary for calculations of force-displacement relationships.

Table 2.1: Properties of the optical trap apparatus and method which formed the starting point for development of the 2P method. Green-shaded significance entries are positive features, while red-shaded significance entries are shortcomings which are addressed in the chapter noted within that entry.

Property	Description	Significance
Active periodic driving	Trap position was dynamically controlled to produce periodic displacement.	Active driving generates large bead displacements which can be measured with Fourier analysis.
CCD video capture	Videos of fluorescent beads were captured with a CCD camera during active driving.	Video is necessary for measuring driven and receiver bead position simultaneously.
Apparatus calibration	Apparatus calibration was performed, but did not consider direction dependence, nonlinearity, time lag, or precision.	Uncertain relation between inputs and outputs can cause systematic biases in measurements.
		Scatter from imprecision could not be distinguished from heterogeneity.
Correlation bead tracking	A large rectangular area surrounding each bead in the first frame is correlated with subsequent images to define bead position in those images.	Higher precision than state-of-the-art centroid tracking.
		The large rectangle lead to performance issues for correlation at image edges.
Fourier analysis	Bead position from correlation tracking is multiplied by a sin or cos to determine amplitude and phase angle of bead displacement at a given frequency.	Fourier analysis allowed isolation of bead displacement at a specific frequency.
		Mismatches between camera frame rate and driving frequency caused biases in measured amplitudes.
Trap force calibration.	Bead displacement resulting from the drag force of water was used to define trap force versus bead-trap offset as a linear, isotropic spring.	Large trap displacements are necessary to generate large bead displacements. Trap force is known to become nonlinear with sufficiently large bead-trap offsets.
Calculation of material properties using bead displacement versus applied force.	Bead displacement was reported, but not paired with force to determine material properties.	Microrheology is not a complete technique if bead displacement is not paired with applied force to determine material properties.

Figure 2.1: Recent photo of the optical trap apparatus with major components labeled.

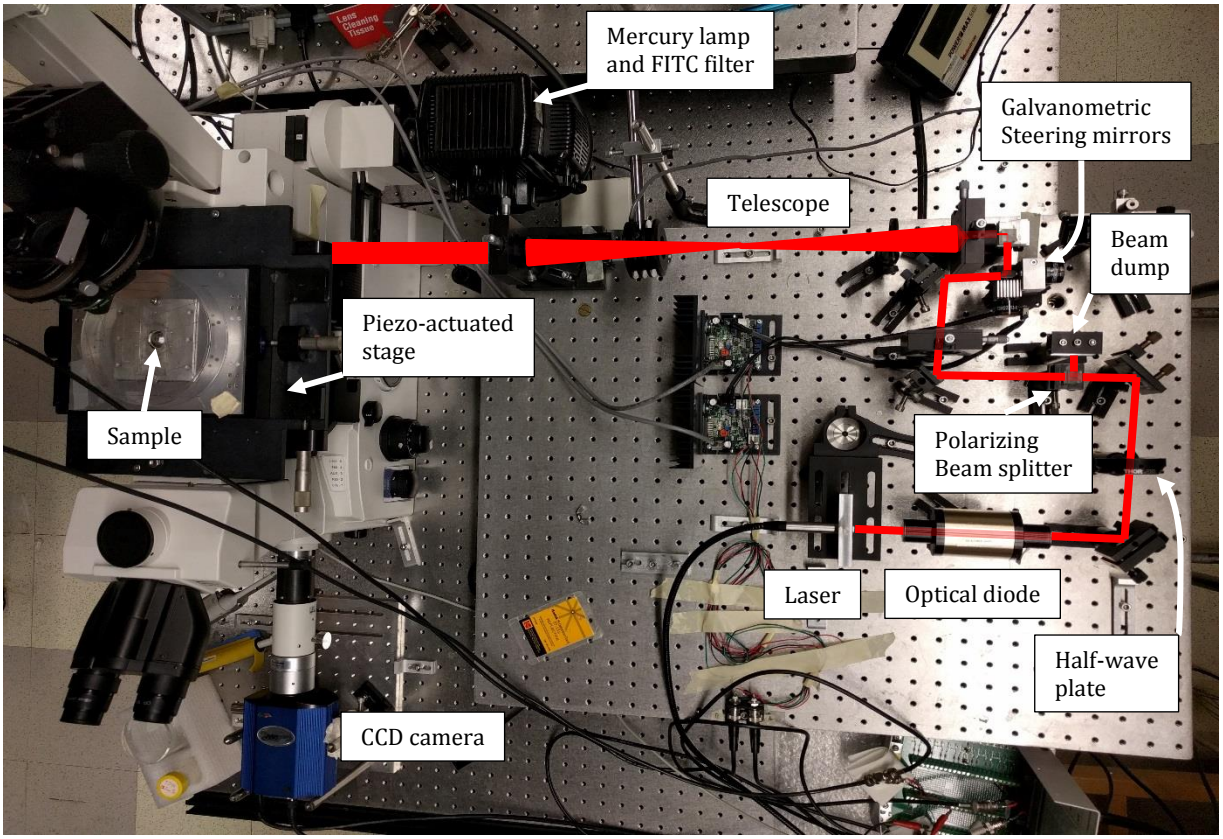

Figure 2.2: Schematic of the apparatus, including optical paths inside the microscope.

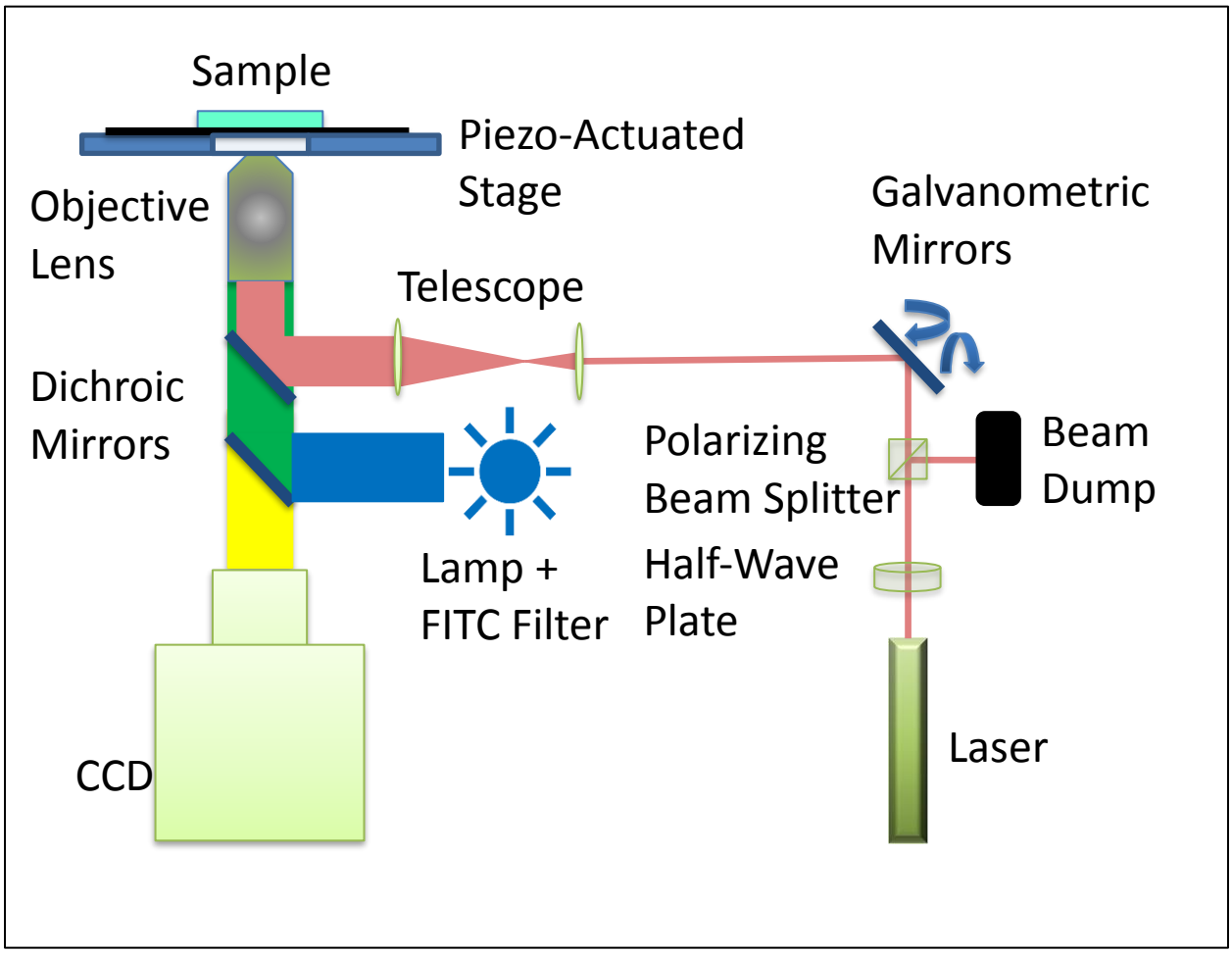

Basic Apparatus Calibration

Several aspects of the system were calibrated using scalar values in the inherited method. These aspects included pixel size, stage displacement versus commanded stage displacement, and trap displacement versus commanded trap displacement. Pixel width of the CCD camera through which all trial videos were collected had been calibrated using images of a stage micrometer and found to be approximately 75 nm per pixel. Stage displacement versus commanded stage displacement had been calculated by analyzing video of 2 µm diameter

yellow-green fluospheres (ThermoFisher Scientific, Waltham MA), henceforth referred to as “beads”, fixed to a coverslip while commanding a specific stage displacement. It was found that peak stage displacement was approximately 1.25 times as large as commanded stage displacement. Laser trap displacement versus commanded trap displacement was calculated in a similar manner, except that instead of observing a bead, the trap beam was observed reflecting off the coverslip surface with laser filters removed. Trap displacement amplitude was found to be approximately 90% the amplitude of commanded trap displacement. These calibrations provided a scalar calibration of key parameters of the apparatus, with potential shortcomings in assuming linearity, isotropy, and lack of phase lag in stage and laser displacement, as well as an absence of rotational misalignment between key components.

Trap Force Measurement

Like other apparatus parameters, trap force versus bead-beam offset was assumed to be linear and was calibrated using a single effective trap stiffness, often referred to as a spring constant. This was the state of the art, with several variations each using a single amplitude of measured bead displacement and a single amplitude of known force to calculate a spring constant.[17,26,27] In the inherited method, calibration was performed on a bead trapped in water within a chamber which had a precision #1.5 coverslip on the side facing the microscope objective lens. Stage displacement was used to generate fluid flow over the bead and hence a drag force on the sphere which could be calculated by Stokes’ law. Stokes’ law is shown in Equation 2.1, where F_d is the drag force, η the dynamic viscosity of the water, a the radius of the bead, and v the velocity of the water relative to the bead. A triangle wave was specified for microscope stage displacement, which would nominally produce periods of constant velocity and corresponding drag force with alternating sign. Video of the trials was captured using μManager, then analyzed in MATLAB with the correlation tracking method to extract bead position versus time.[25] Bead position versus time during one such test is shown in Figure 2.3. Measurements of the bead displacement range were made using a ruler held to the computer screen, then plugged into Stokes' law to calculate trap stiffness according to Equation 2.1. Two measurements of trap

stiffness along each axis were averaged to generate a single value. The result of the trap force calibration procedure was a single effective spring constant, as defined in Equation 2.2, for bead-beam offset within the focal plane.

$$F_d = 6\pi\eta a v \tag{2.1}$$

$$K_{trap} = \frac{2F_d}{x_{bead,max} - x_{bead,min}} \tag{2.2}$$

Figure 2.3: Measured bead displacement during a trap force calibration trial using the inherited method. Drag force was imposed on the bead through triangle wave displacement of the stage, which generated nominally square wave stage velocity with respect to time. Bead displacement was estimated visually.

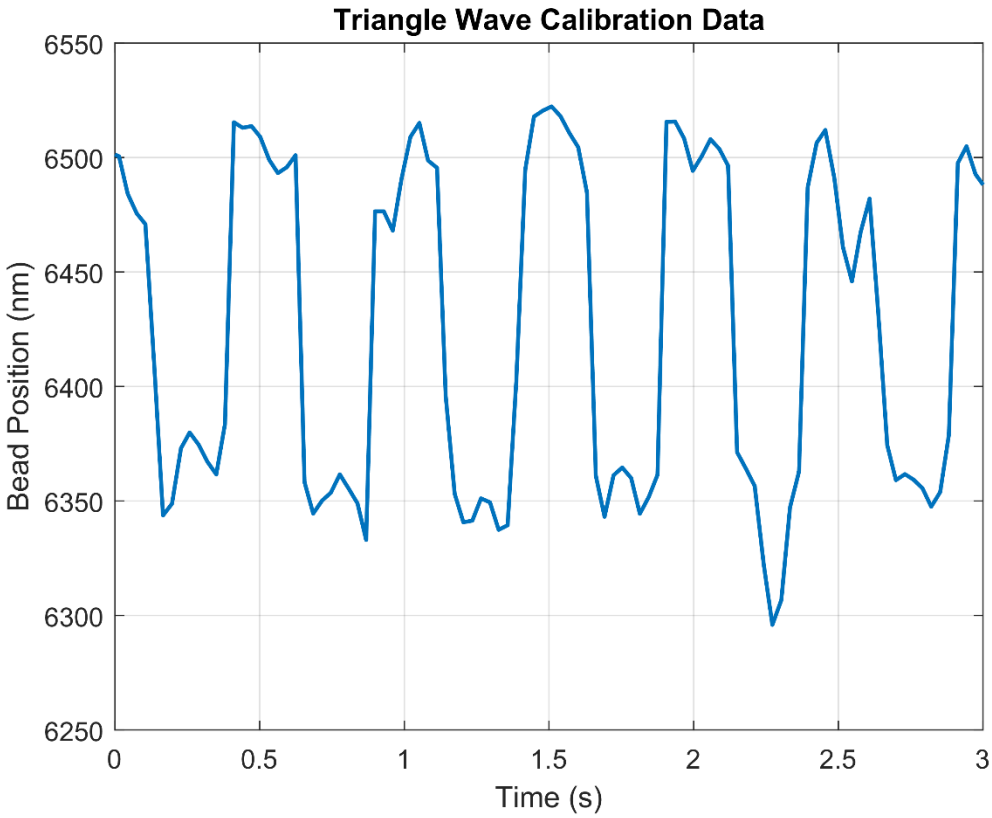

Inherited Data Collection Process in Gels

The inherited method included a protocol for collecting data of bead displacement in gels during active driving of a single "driven" bead. The protocol made use of two LabVIEW programs towards this purpose, the first for centering the trap on a chosen bead within a gel, and the second for generating oscillatory displacement of the trap. The essential steps were:

1. **Sample placement**: Place a cover slip with a gel sample on the stage. The mercury lamp and laser should both be powered on and at thermal equilibrium, but not emitting light into the sample to minimize photo bleaching of the beads. Both LabVIEW programs should be open in preparation for running them when a suitable geometry is identified. μManager should be open and displaying the field of view in live view mode.[25]
2. **Rough identification of trap location**: Adjust the laser power to 0.1 watts. Remove the laser filter from the microscope to make the spot of the laser trap beam visible in μManager via the CCD camera. Focus the trap beam on the cover slip surface so it appears as a small bright spot and mark the center of the spot in μManager.[25] Replace the laser filter.
3. **Identifying a set of beads**: Scan through the sample using manual stage controls to find a suitable arrangement of beads, all of which should be in the field of view and in focus. Choose one bead to be the driven bead and roughly center it on the mark in μManager indicating the trap location. Reduce the captured field of view until it contains the entire bead arrangement plus a border or buffer region of approximately one bead diameter. The smaller the field of view, the larger the effective frame rate.
4. **Precisely identifying the trap location**: Draw a circle centered on the driven bead, remove the laser filter, and move the focal plane so the trap beam spot appears on the cover slip. Move the

circle so that it is perfectly centered on the beam spot. Replace the laser filter and move the focal plane back to the bead arrangement.

5. **Verifying settings**: Verify/update all parameters in the bead driving LabVIEW program and µManager. In the bead driving program, this includes amplitude and frequency of trap displacement, angle of trap displacement, trap displacement pattern, and driven bead number. In µManager, this includes exposure time, time between frames, and total number of frames.
6. **Centering the trap on the driven bead**: Use the fine position adjustment LabVIEW program to center the driven bead in the circle. Stop the fine position adjustment program.
7. **Setting final trap power**: Set the laser to the desired power. Stop live view mode in µManager.
8. **Image acquisition during bead driving**: Start the bead driving LabVIEW program. Start image acquisition in µManager. Save the TIFF stack with a name matching the files generated by LabVIEW when the trial is complete.
9. **Repetition**: Repeat steps 3-8 until done collecting data.

Inherited Method for Extracting Bead Positions and Displacement Amplitudes

Videos of bead displacement were analyzed to extract bead positions versus time and generate corresponding Fourier spectra, with emphasis on peaks at the driving frequency of the trap (2 Hz). The videos were captured with µManager as a TIFF stack, with an associated metadata file specifying time stamps for each frame.[25] A MATLAB program, written largely by Prof. Greg Lafyatis and Tyler Heisler-Taylor, extracted bead positions within the image plane for each video frame using the correlation method with paraboloid fitting described by Cheezum et al.[22] The final outputs of the MATLAB program were sinusoidal and cosinusoidal Fourier spectra in X and Y for the displacement of each bead.

The correlation method of particle tracking (Figure 2.4) specifies particle position by using comparison of a "kernel", an image region in the first frame containing a bead, to a region of a different image frame which is expected to contain the same bead. The strength of correlation is calculated for a particular positioning of the kernel over the subsequent frame by multiplying the value of each pixel in the kernel by the value of the pixel at the same location in the subsequent frame, then summing up the values obtained for each pixel. The position of the kernel is rastered over a grid, with the correlation being recorded each time. The correlation values versus XY position are fitted to a function and the location at which the value peaks is recorded as the interpolated bead position.

Figure 2.4: The major steps in correlation particle racking. Each bead in each frame is compared to the same bead in the first frame. The steps are: identify a bright region in Frame 1 and make a kernel by cutting out a kernel centered on the bright region; scan the kernel over another frame while recording the match quality ("correlation strength") at each location; and define the fine bead position by fitting the highest match quality values versus position to a quadratic equation, with the fitted peak defining the position.

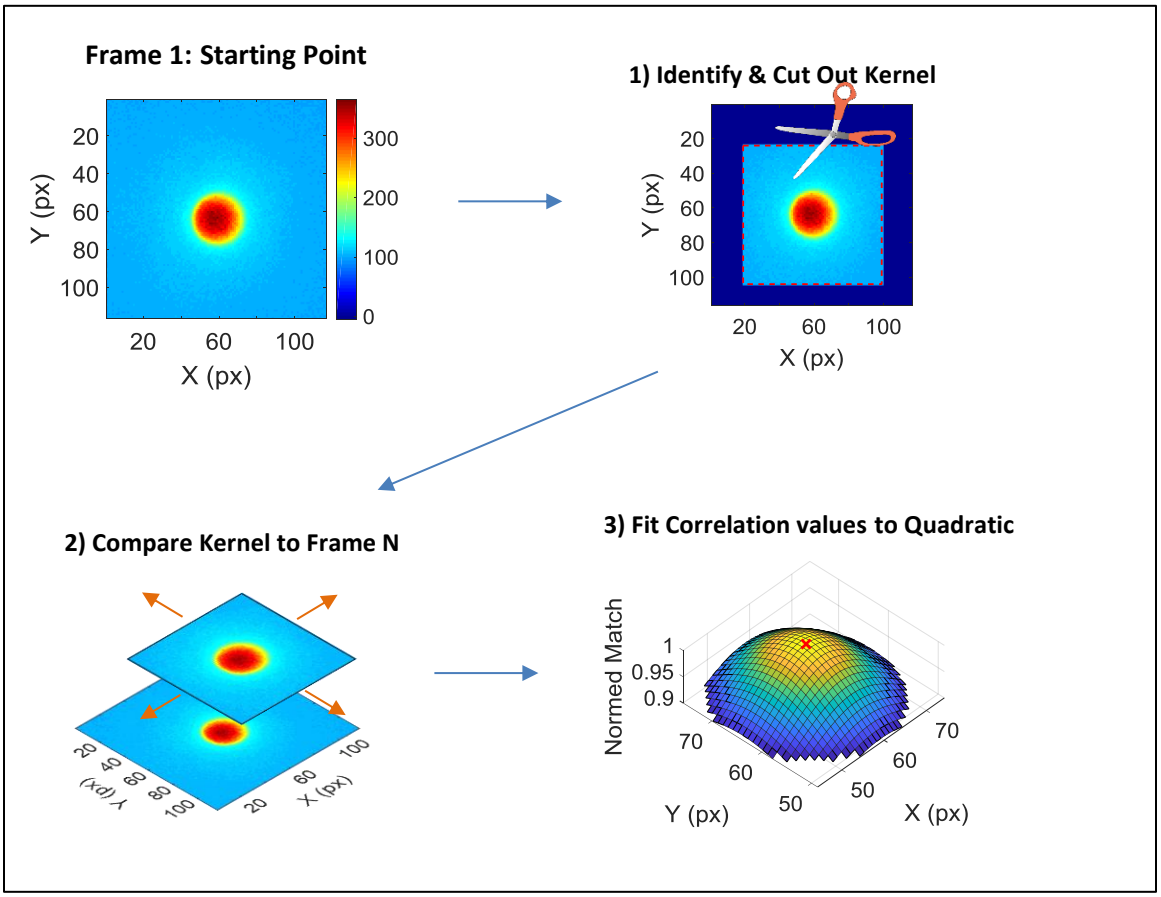

The extraction of bead positions started with bead identification in the first frame and generation of a kernel for each detected bead in that frame. The first step in identification of beads was morphologically opening a copy of the first video frame, morphological opening being an algorithm designed to remove bright speckles from images.[28] The resulting image was then thresholded to convert it to binary black and white. White regions of sufficient size were designated as beads, identified with a number defined by ordering the centroid of each

white region within the image frame from left to right and top to bottom. The initial coordinates of each bead were also defined as the centroid of the corresponding white region. The kernel for each bead was defined as a rectangular area of the original video frame with the same centroid as the corresponding white region, but with width and height 1.5 times that of the minimum bounding box. The rectangular kernels and initial position information were saved for use in determining the position of the beads in successive frames.

In subsequent frames, correlation was performed using the first kernel on the first identified bead, the second kernel on the second identified bead, and so on. Repetition of the correlation process with all frames nominally resulted in a time-stamped list of positions for each bead. The process was able to identify the position of a majority of beads as a function of time; however, beads losing or gaining focus and errors in time stamping of image frames occasionally led to unusable data.

Fourier spectra, which define the displacement amplitude of each bead versus frequency, were generated from the time-stamped position data for each bead along each axis. Two spectra were generated for each bead in each direction: one using sine terms and another using cosine terms (Equations 2.3 and 2.4, respectively), respectively defining "in-phase" and "out-of-phase" displacement at the driving frequency. Representative spectra for a driver and receiver are shown in Figure 2.5.

$$\boldsymbol{A_f = \sum_{i=1}^{N} \frac{2}{N} \sin(2\pi f t_i)\, X_i} \tag{2.3}$$

$$\boldsymbol{B_f = -\sum_{i=1}^{N} \frac{2}{N} \cos(2\pi f t_i)\, X_i} \tag{2.4}$$

Figure 2.5: (a) A representative Fourier spectrum for a driven bead with a 2 Hz displacement amplitude of ~65 nm, and smaller amplitude components of displacement at 4 and 6 Hz. Other frequencies have non-zero measured amplitudes due to thermally-induced bead displacements, optical noise affecting the camera, and imperfect image analysis. (b) A representative Fourier spectrum for a receiver bead with a 2 Hz displacement amplitude of ~5.3 nm. Non-zero amplitudes measured at other frequencies are from the same origins as those for the driven bead. The sharp rise of the noise floor towards 0 Hz limits the precision of lower frequency measurements.

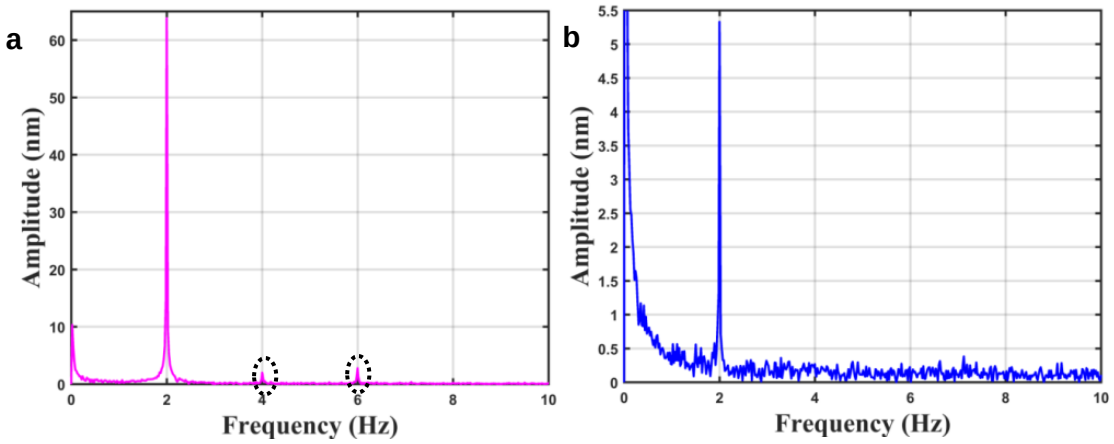

Review of the Inherited Method

The inherited method calibrated the force of an optical trap according to the state of the art and subsequently used trap displacement to generate bead displacements which were reported via Fourier spectra along each axis with phase information. The method was not complete in that it did not yet calculate force applied to the driven bead and thus could not progress to the final step of calculating mechanical properties of the gel. The method did provide raw data which could be used to compute force-displacement couplings and mechanical properties, providing a basic foundation for the 2P active microrheology method.

Goals in development of 2P active microrheology

The major goals, as shown in Table 2.2, were to: make consistent, accurate measurements; to quantify the uncertainty in each measurement, and to measure material properties versus bead separation. The first goal became a focal point not only out of an inherent desire for results which reflect reality, but also from observed weaknesses in the state of the art. Wide scatter in measurements and a lack of discussion related to calibration led to concern for the validity of particular values reported in the literature. A comparison by Dasgupta and Weitz of rheological data from different methods highlighted the possibility of discrepancies between methods, as passive multi-particle microrheology was found to have a discrepancy of up to an order of magnitude from other methods (Figure 2.6).[29] Quantification of error in data came to be a key goal for similar reasons. Both internal data and literature showed wide scatter in values within a single data set. An example of state of the art calibration (Figure 2.7) demonstrates wide scatter in measurements which could introduce error into mechanical property measurements as those values are directly dependent on calculations of applied trap force.[30] Similarly, another study made measurement of modulus within a single collagen sample which spanned multiple orders of magnitude, but did not have error bars for individual values (Figure 2.8), raising questions about how much scatter might be due to the method itself.[14] Finally, the goal of mapping material properties versus bead separation was the result of considering what had never been seen in the literature. Although multi-particle microrheology, at least of the passive variety, has been widely practiced, no studies were found in which length scale was considered for measured properties except in theoretical calculations of convergence to macroscopic values. The foundation of the inherited apparatus and method provided a baseline set of abilities to use in development of a method meeting these goals.

Figure 2.6: A comparison by Dasgupta and Weitz of multiple rheological measurements of shear storage and loss moduli, G' and G'', in 3wt% polyacrylamide gels with 0.05wt% bis-acrylamide. Passive multi-particle rheology is indicated by magenta diamonds and has the highest values of modulus out of any method at a given frequency, with an order of magnitude discrepancy between multi-particle microrheology and quasielectric light scattering, the method which produced the lowest values.[29]

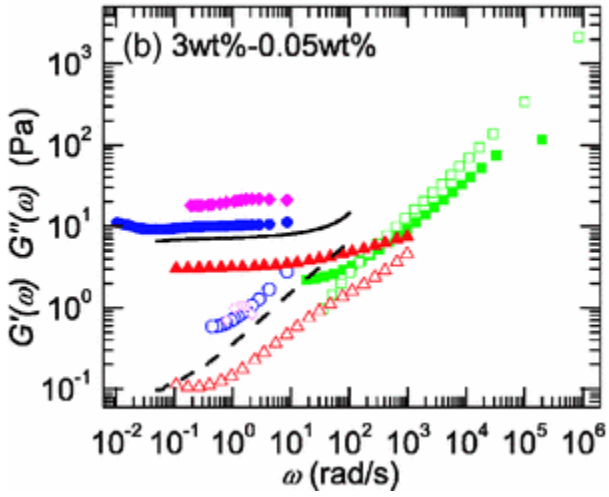

Figure 2.7: : An example of trap force calibration measurements made according to the state of the art. Non-negligible scatter can be observed, as well as a lack of apparent consistency in values with respect to bead-trap offset.[30]

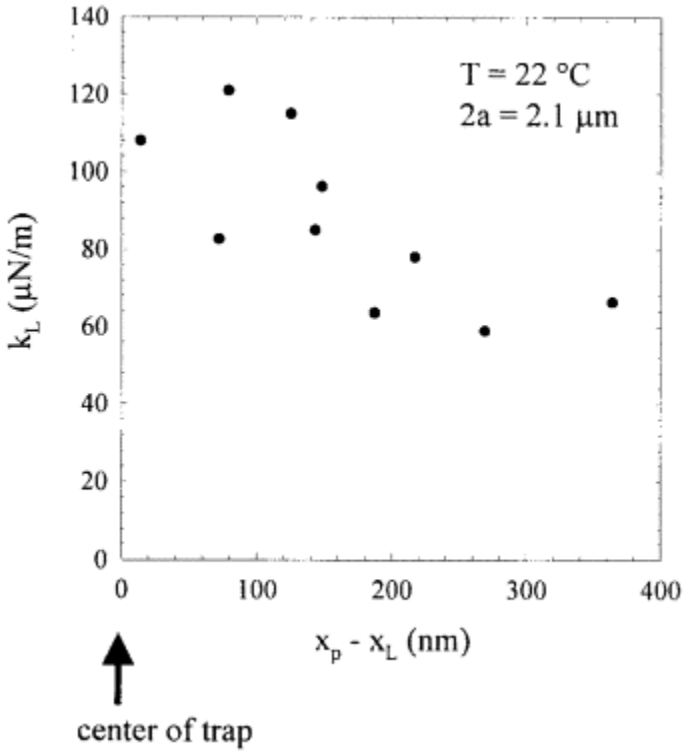

Figure 2.8: Shear storage and loss moduli versus local density of collagen fibrils.[14]

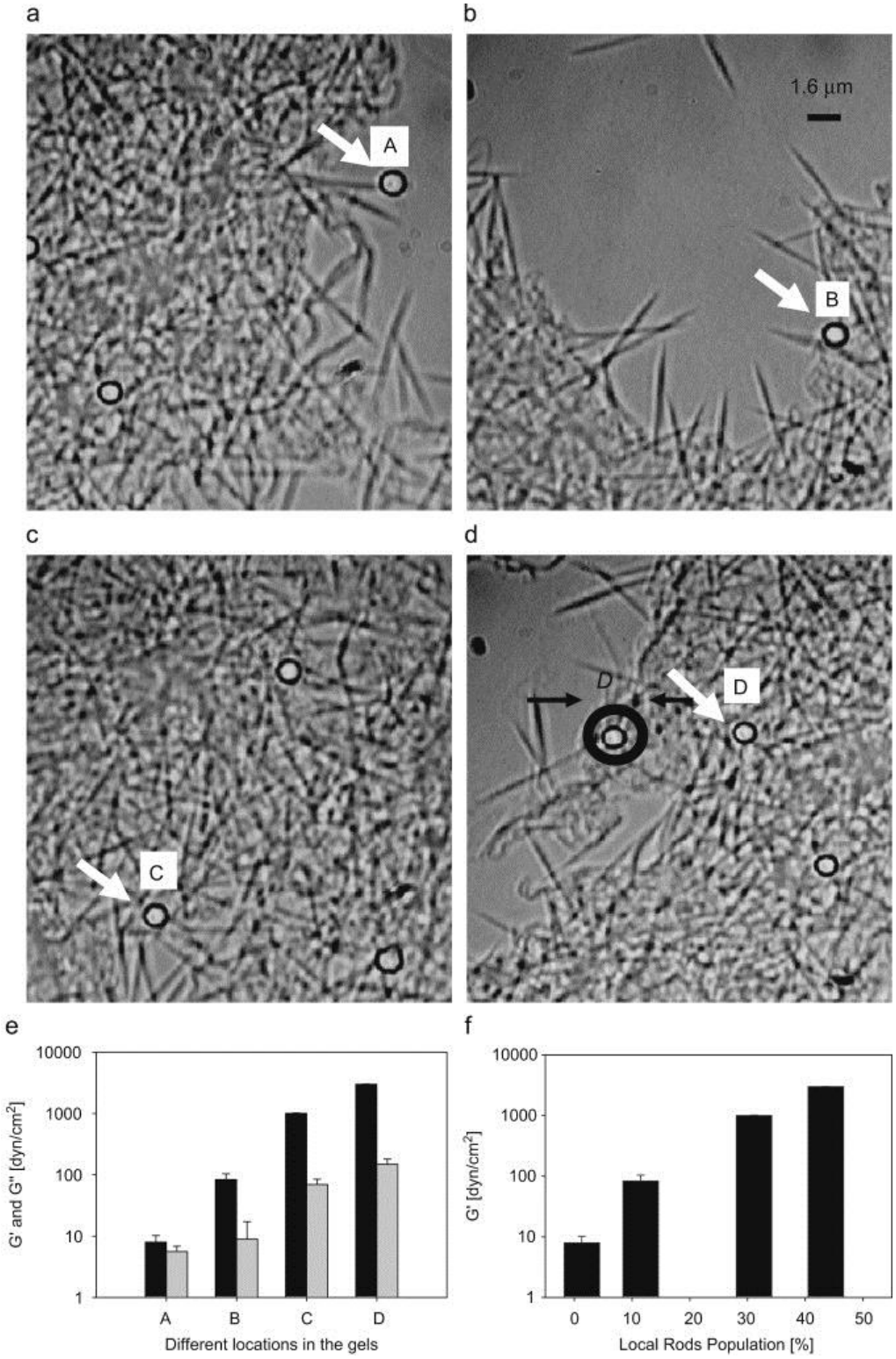

Table 2.2: Key goals in development of the 2P Method.

Goal	Impact
Make consistent, accurate measurements.	Measurements should be accurate if the exact relationship between inputs and outputs is known. Standard calibration protocols for mapping the relationships between apparatus inputs and outputs would allow results to be compared between labs.
Quantify uncertainty in measurements	Knowledge of measurement uncertainty allows partitioning of scatter between uncertainty and variation in material properties.
Measure material properties versus bead separation	Exposes length scales of heterogeneity in a given material through trends in the mean value or scatter of each measured value.

Chapter 3 : Refined Apparatus Calibration

Innovations

Precision and accuracy in the 2P method is only possible when the performance and relation of every component in the apparatus is known. This includes the camera used to observe the beads and trap beam, the laser, the galvanometers used to steer the trap beam, and even the microscope stage. For example, if a camera pixel covers a smaller or larger area than expected, the distance between beads and the displacement of beads will each be over or under estimated, leading to erroneously low or high calculations of gel modulus. It is possible to account for distortion in camera images, or for the galvanometers steering the trap in a different coordinate system than the camera, but only if the relationship between actual and expected performance are known. Similarly, the galvanometers or stage may have displacement smaller or larger than the commanded displacement, and the scaling may even change depending on the current apparatus state. Again, this can be accounted for, but only if the equations relating commanded and actual displacement are known. Calibration of the camera, laser displacement, and stage displacement removed multiple sources of potential error in measurements by providing a coherent coordinate system and equations for predicting displacement within that coordinate system.

Table 3.1: Innovations in apparatus calibration.

Innovation	Description	Impact
End-to-end calibration of an optical trap apparatus	We measured the responses of the stage and trap to commanded sinusoidal displacement in camera coordinates. Pixel size was measured along both X and Y.	Measurements with well-characterized relationships to inputs are accurate. Standard calibration protocols would allow results to be compared between labs.

Camera Calibration

The camera is the component through which every position and displacement is measured, making it critical to know the dimensions of a pixel in the focal plane, and whether those dimensions are consistent. Camera calibrations are typically not mentioned in microrheology studies, although Crocker and Grier briefly mentioned taking images of a reference grid to calculate distortion in their widely-cited paper on particle tracking.[23] The calibration performed in the inherited method was a single, measurement using a stage micrometer, which yielded an effective pixel dimension at the focal plane of 75 nm along each axis. In the mature 2P method, pixel dimension was measured in both axes and checked for consistency at different locations. This yielded the same 75 nm square pixel size found in the inherited method. Although the calibration did not change any calculations of position or displacement, it ruled out image distortion as a significant source of error in calculations.

Laser Trap Force

Microrheology studies almost universally assume that laser trap force is linear and isotropic versus trap-bead offset, although theoretical calculations indicate that this only holds true for small offsets near the trap center, even with the assumption of a perfect trap beam.[21,31–35] Theoretical trap force curves with recognizable nonlinearity even at small displacements are shown in Figure 3.1. The nonlinear trap force of theory strongly

suggests that laser trap force should be measured as a landscape, rather than as the isotropic spring constant typically assumed in optical trap studies.

The inherited method followed the convention of measuring a single trap force and treating it as an isotropic spring constant, while the mature 2P method measures trap force as a landscape. Nonlinearities and anisotropy were found in trap force which had caused approximately a 20% error in mean modulus calculations, and could have caused errors as high as 40%. The methodology for measuring trap force landscape and detailed findings from using this methodology are presented in the next chapter.

Figure 3.1: Theoretical trap force calculated using the Optical Trap Toolbox written by Nieminen et al with a Gaussian beam truncated at a cone half angle of 40 degrees.[21] The x axis is bead-trap offset (bead position vector minus trap position vector) in units of trap beam wavelength, and the Y axis is trapping efficiency, which is proportional to trap force. For the 1064 nm laser used in the 2P apparatus, nonlinearity becomes visually apparent at offsets of 100-200 nm. The curves labeled *X* and *Y* are generated along the axis of polarization and perpendicular to it, respectively.

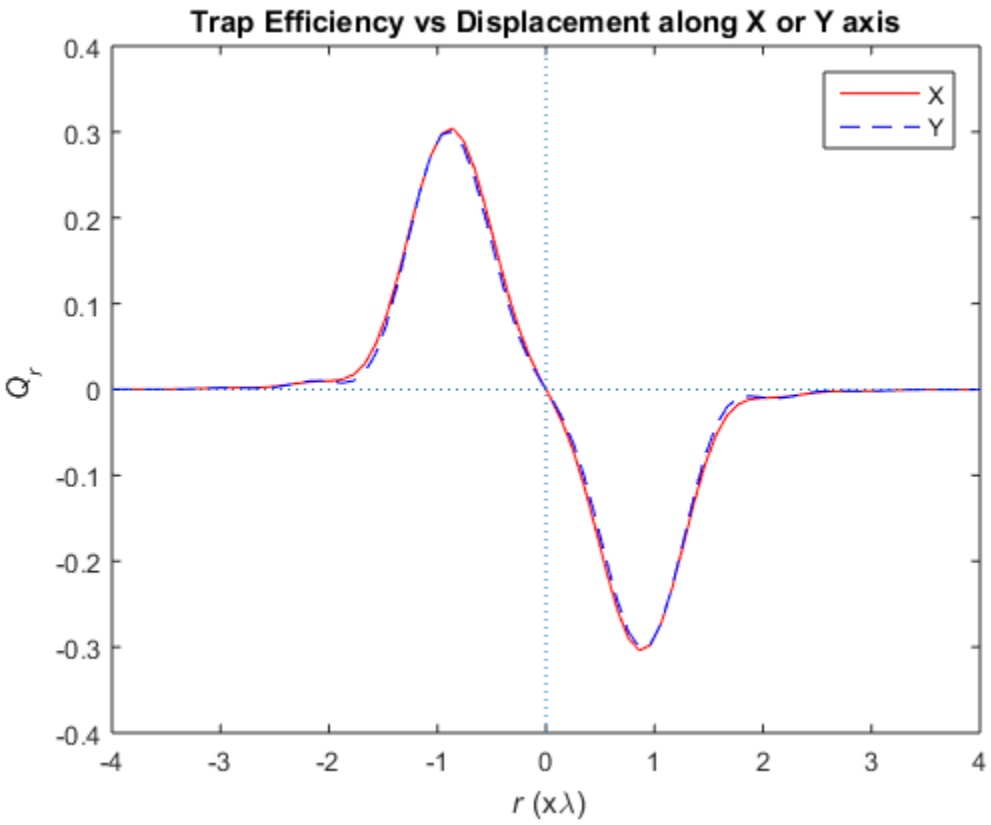

Trap Displacement Calibration

In the 2P method, force is applied to the driven bead via displacement of the trap laser beam. This means that any error in trap displacement would cause concomitant discrepancies between the force which was actually applied to the bead and the force which was expected. In the inherited method, peak trap displacement was measured for a nominal 500 nm amplitude sinusoidal displacement, specified in a LabVIEW program. The resulting displacement was taken to be perfectly sinusoidal, to have no time lag with respect to the input signal, to align with the camera image sensor coordinate system, and to be consistent between the galvanometer controlling X displacement and the galvanometer controlling Y displacement of the beam. With the exception of sinusoidal displacement, each assumption of ideal behavior in trap displacement proved to be a source of error when calculating force applied to a driven bead.

In the mature 2P method, laser displacement versus commanded displacement was calibrated for isotropy, nonlinearity, rotation, and time delay. Data for these calibrations were generated by commanding sinusoidal laser displacement at 2 Hz with 200 or 500 nm amplitude at a multiple of 45° for each trial, with trial angles ranging from 0° to 315°. Video was captured of the laser spot reflecting off a cover slip surface after removing a filter which normally blocked laser light from reaching the camera. The laser position was determined in each video frame by fitting a 2D Gaussian to the brightest region within the frame. Laser displacement was then analyzed using Equations 2.3 and 2.4 across a range of frequencies, explicitly including 2, 4, and 6 Hz. Isotropy, nonlinearity, rotation, and time delay were measured using the displacement amplitudes with phase information at these frequencies along both axes.

Figure 3.2: Measured laser trap displacement vectors compared to commanded laser trap displacement vectors. Each colored, dashed line represents a commanded laser displacement terminating at a marker indicating 500 nm of displacement at the nominal displacement angle. Crosses with the same color are measured displacements at that nominal displacement angle with nominal amplitudes of 200 or 500 nm. Besides a consistent rotation between the coordinate system of expected displacement and measured displacement, direction-dependent scaling can also be seen in measured trap displacement.

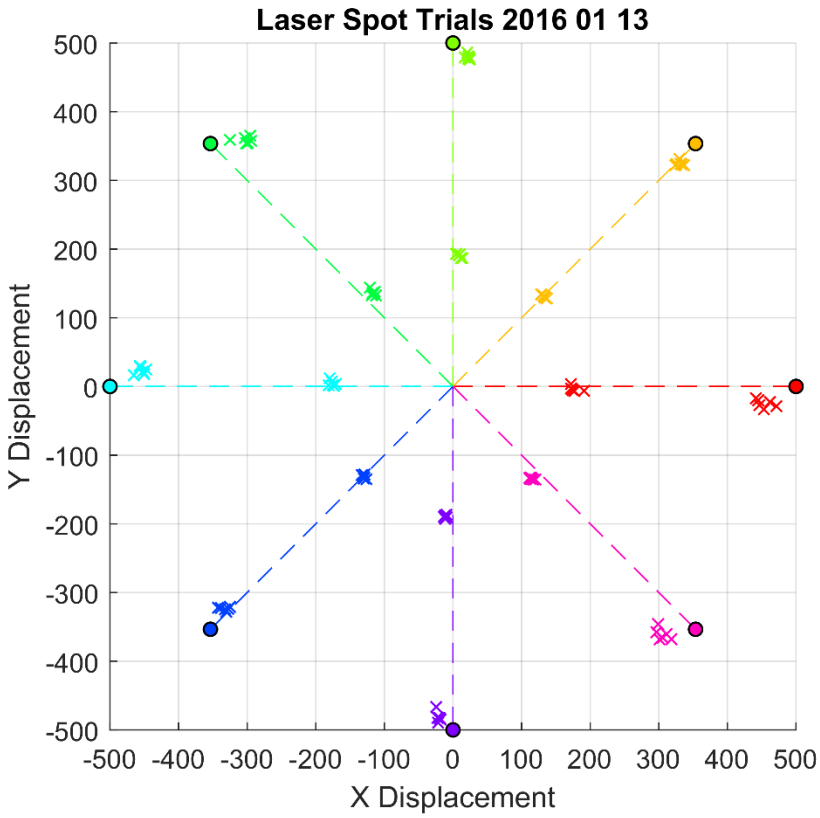

Nonlinearity was measured through observations of harmonics in the Fourier spectra of laser displacements and through the ratio of measured 2 Hz displacement amplitudes for trials with commanded displacements of 200 and 500 nanometers. The presence of harmonics or a 2 Hz amplitude ratio other than 0.4 would indicate a deviation from the sinusoidal displacement commanded. Harmonics were indistinguishable from noise and the amplitude ratio between 200 and 500 nm commanded displacements was consistently 0.4, leading to a finding of linear displacement with respect to the input command signal.

Phase lag of the actual displacement with respect to the commanded displacement was determined using Equation 3.1, where ϕ is the phase lag, A_{IP} is the amplitude of the 2 Hz displacement component in phase with the commanded displacement, and A_{OP} is the amplitude of the 2 Hz displacement component out of phase with the commanded displacement. A_{IP} and A_{OP} are defined in Equation 3.2 and Equation 3.3, respectively, with x_i being the position of a bead along either axis at time t_i and f being frequency. Phase lag at 2 Hz was found to be 1.6±0.2°, or 2.2±0.3 ms when formulated as time lag.

$$\boldsymbol{\phi = \tan^{-1}\left(\frac{A_{OP}}{A_{IP}}\right)} \tag{3.1}$$

$$\boldsymbol{A_{IP} = \frac{1}{n}\sum_{i=1}^{n} x_i \sin(2\pi f t_i)} \tag{3.2}$$

$$\boldsymbol{A_{OP} = -\frac{1}{n}\sum_{i=1}^{n} x_i \cos(2\pi f t_i)} \tag{3.3}$$

Rotation and anisotropic scaling of laser displacement were found by determining θ, T_x and T_y in Equation 3.4. MATLAB was found to perform poorly on angular fitting, so these values were determined in a two-step process. First, the difference between measured angle of displacement and commanded angle was determined at each angle increment tested, and the mean difference in angle from all tested angles was taken to be θ. This measured angle of rotation was negated by applying an opposite rotation. The second step was determination of T_x and T_y using linear fitting of X and Y displacements versus commanded displacement in the respective directions across all angles tested. Using this method on the inherited apparatus without adjustment, it was found that $\theta = 2.6°$, $T_x = 0.87 \pm 0.02$ and $T_y = 1.02 \pm 0.02$. A new set of calibrations yielded $\theta = -0.2°$ after realigning the camera to the microscope, validating the hypothesis of misalignment between components introducing angular bias in the system. Fitting measured displacements to Equation 3.4 allowed any directional discrepancies between commanded and actual displacement to be accounted for, regardless of the level of inherent error.

$$\begin{bmatrix}\Delta x_{actual}\\ \Delta y_{actual}\end{bmatrix} = \begin{bmatrix}\cos\theta & -\sin\theta\\ \sin\theta & \cos\theta\end{bmatrix}\begin{bmatrix}T_x & 0\\ 0 & T_y\end{bmatrix}\begin{bmatrix}\Delta x_{commanded}\\ \Delta y_{commanded}\end{bmatrix} \quad (3.4)$$

Thorough calibration of laser trap displacement avoided several sources of errors, and ruled out a potential source of errors. Direction-dependent scaling of trap displacement versus commanded displacement would have led to direction-dependent modulus errors of 2-13%, which would also have led to erroneous findings of anisotropy. Rotation of trap displacement with respect to the nominal displacement angle would have led to erroneous classification of force-displacement coupling as nonlinear. Displacement lag with respect to the input signal would have led to incorrect calculation of viscoelastic displacement lag, which then would have led to errors in calculating viscoelastic material properties. Nonlinearity of trap displacement with respect to the commanded displacement was ruled out, but could have affected findings related to linearity of material response. In all, three categories of corrections were made for trap laser displacement, avoiding a larger number of erroneous findings.

Stage Displacement Calibration

Stage displacement was used in trap force measurement for the 2P method, and so could introduce several of the same errors possible with laser trap displacement. The author is not aware of any microrheology papers which mention calibrations of stage displacement, even though there are references to using stage displacement for trap force calibration.[31,32] In the inherited method, peak stage displacement was measured for a nominal 10 µm amplitude sinusoidal displacement along X or Y, specified in a LabVIEW program. The resulting displacement was taken to be perfectly sinusoidal, to have no time lag with respect to the input signal, to align with the camera image sensor coordinate system, and to be consistent between the piezo actuator controlling X displacement and the piezo actuator controlling Y displacement of the beam. Each assumption of ideal behavior in stage displacement proved to be incorrect, and all but one proved to introduce error in trap force calculations.

Instantaneous stage velocity, and hence stage position, were foundational for calculating trap force versus bead displacement, making calibration equally foundational. For trap force calibration trials in the 2P method, the commanded stage position versus time was a fixed amplitude sine wave at 2 Hz. To calculate stage velocity at any moment in time, it was necessary to know the stage position in terms of a 2 Hz periodic function. Stage position in ended up being well-modeled by Equation 3.5 with different coefficients for X and Y displacements.

$$\boldsymbol{X_{stage}} = \sum_{i=1}^{5} \boldsymbol{A_i} \sin(\boldsymbol{4i\pi t} + \boldsymbol{\phi_i}) \tag{3.5}$$

Stage displacement was calibrated in much the same way as laser displacement, but with some aspects simplified. Stage displacement was only used for trap force calibrations – covered in detail in the next chapter – which were performed in either the X or Y direction for a given trial. Bead displacement was taken to be an instantaneous equilibrium between trap force and applied viscous drag force. The drag force was taken to be linear with respect to stage velocity, meaning that small displacements perpendicular to the intended displacement direction could be ignored. With perpendicular displacement ignored, it was still necessary to quantify nonlinearity, phase lag, and direction-dependent displacement scaling.

Stage displacement was measured using video of a bead adhered to a coverslip mounted to the stage, which was itself undergoing displacement identical to that used in the force calibration trials referenced in the previous paragraph. Specifically, commanded stage displacement was a 2 Hz, 20 µm amplitude sine wave. To counter blurring from the high velocity of the bead relative to other trials, image acquisition time per frame was 1 ms. The bead still changed position by almost 2 pixels during acquisition of a single frame at peak velocity, so bead position was defined in each frame as the centroid of a thresholded bright region instead of with the shape-sensitive correlation method used for most particle tracking in the 2P method. Bead position versus time was analyzed using Equations 3.3 and 3.4 to obtain displacement amplitude at the fundamental frequency of 2 Hz, as well as at the 2nd-5th harmonics, and phase lag at each of the corresponding frequencies. The values obtained were then used to generate a function for stage displacement versus time. Figure 3.3 is a

representative bead position versus cyclic time plot, overlaid with the fitted position function used to define stage velocity.

Figure 3.3: A scatter plot of measured stage position versus cyclic time at 2 Hz, overlaid with the fitted function of position which was used to determine stage velocity.

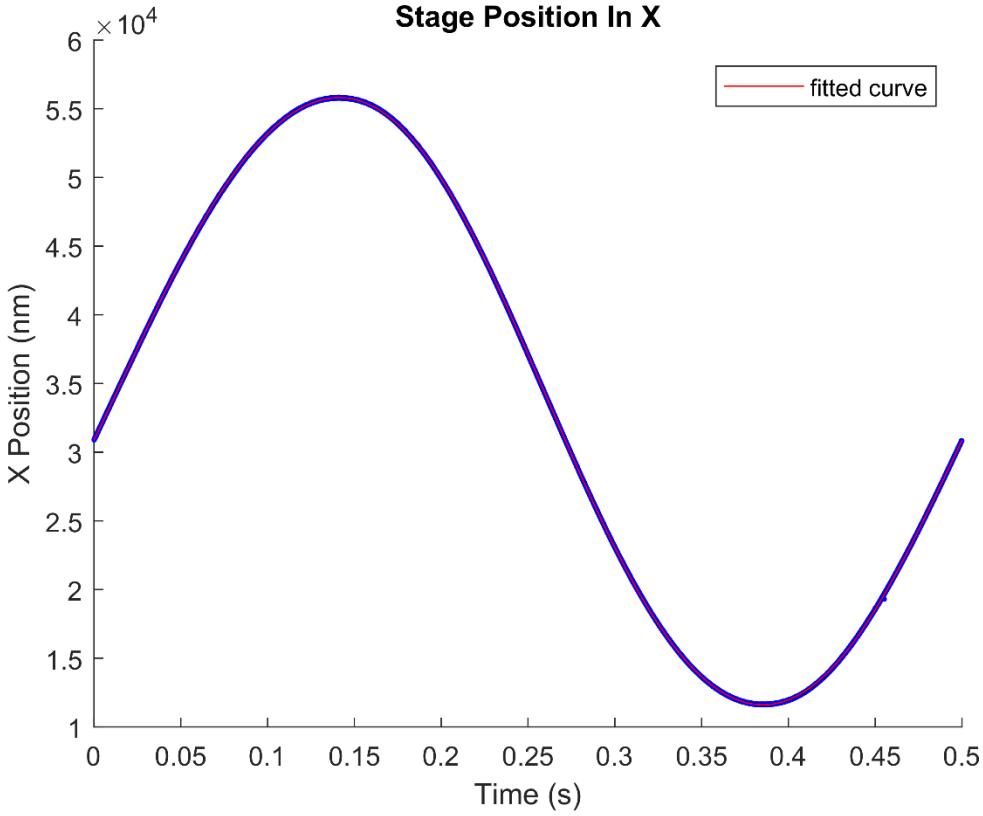

Stage displacement was found to deviate from the expectations of a pure sinusoid at the exact phase angle of the commanded displacement. Multiple sin terms with independent lag values were necessary to get good

agreement between fitted displacement and actual displacement. Furthermore, the shape and lag of the displacement in X and Y were different. Without thorough calibration, stage displacement would have introduced apparent hysteresis and nonlinearity into trap force calculations.

Refined Calibration Summary

With the exception of camera pixel shape, every major component in the apparatus was found to behave in ways that would introduce systematic error into calculated force and displacement without detailed calibration. Individual errors tended to be on the scale of 10%, but this was for a system that had already undergone basic calibration. Other groups have published studies without addressing systematic discrepancies of an order of magnitude, and it seems likely that calibration issues such as found in the inherited method contributed to these discrepancies.[29] Thorough, detailed calibration of every apparatus component is necessary to avoid introduction of unnecessary error into measurements.

Sources of Error Identified

Table 3.2: Sources of error identified in the optical trap apparatus and method during calibration.

Error in:	Discrepancy Values
Stage Displacement	Scaling: sinusoidal displacement component at 2 Hz underestimated by 11% in X, 9% in Y Nonlinearity: second harmonic displacement 2% in X, -1% in Y; smaller 3rd-5th harmonics Time delay: 12 ms in X and 6 ms in Y
Trap Displacement	Scaling: sinusoidal displacement component at 2 Hz overestimated by 16% in X and 8% in Y 3° rotation between camera and trap coordinate system Time delay: 2 ms in X and Y
Nonlinear trap force versus trap-bead offset	Up to 33% underestimation of applied trap force.

Chapter 4 : Measuring Bead Position and Displacement

Introduction

The purpose of this chapter is to describe why issues were suspected in measuring bead position and displacement, how those issues were addressed, and the results of the modifications. Bead displacement is a crucial part of every property measurement in microrheology and is derived from bead position data, so both the measurement of bead position and the process of extracting amplitude of displacement from the driving force are key factors in determining the accuracy and precision of reported property values. Since bead displacement cannot be known as an absolute, expectations for measured bead displacement were set by analytical equations for the displacement field resulting from force on a rigid bead in a linear elastic, homogenous medium. This is illustrated in Figure 4.1a, for which a circle of force vectors on a driven bead results in an ellipse of receiver bead displacements oriented perfectly towards the driven bead. Suspicions about the data processing were prompted by deviations from the generally expected force-displacement relationship, and were resolved to good effect by the innovations in Table 4.1.

Table 4.1: Innovations in measuring bead position and displacement.

Innovation	Description	Impact
Reduced template size	Use of a template slightly smaller than the bead for correlation particle tracking, as opposed to the much larger template used by Cheezum et al.	A reduced template size should allow for correlation mapping even near image boundaries without greatly reducing tracking precision in other situations.
Simple background subtraction	Subtract the value of the darkest pixel in each frame from that entire frame before performing correlation	Reducing background brightness effectively magnifies the contrast used in correlation, which should result in more precise tracking.
Sinusoidal trap displacement	Bead displacement was sinusoidal in synthetic data and commanded trap displacement was sinusoidal in experimental data	Sinusoidal signals are the simplest to measure with Fourier analysis and allow direct quantification of nonlinearity through use of harmonics and phase lag.
Integer cycles of displacement data	Truncate each bead position time trace at an integer number of driving cycles before performing Fourier analysis	Minimizes biases in measured displacement amplitude which results from non-zero mean bead position during the fractional cycle.
Zeroing mean position	Subtract the mean value of each position time trace before performing Fourier analysis	Removes non-zero mean position as a source of bias in Fourier analysis.
Generation of full Fourier spectra	Generation of full Fourier spectra with phase information for bead displacement along each axis.	Harmonics allow quantification of nonlinearity, which enabled detection of soft sheaths around beads. Non-harmonic frequencies allow quantification of displacement noise.

Figure 4.1: Schematic representation of a driven and receiver bead in an ideally isotropic, elastic medium. A local coordinate system is defined with the origin at the center of the driven bead, and the positive X axis passes through the center of the receiver bead. A series of equal magnitude force vectors are applied to the driven bead at increments of 45°. The collection of force vectors is circumscribed by a perfect circle. The response of the receiver bead is a series of displacements circumscribed by an ellipse aligned along the local coordinate system. The scaling of the major and minor ellipse axes are defined by the elastic constants of the medium.

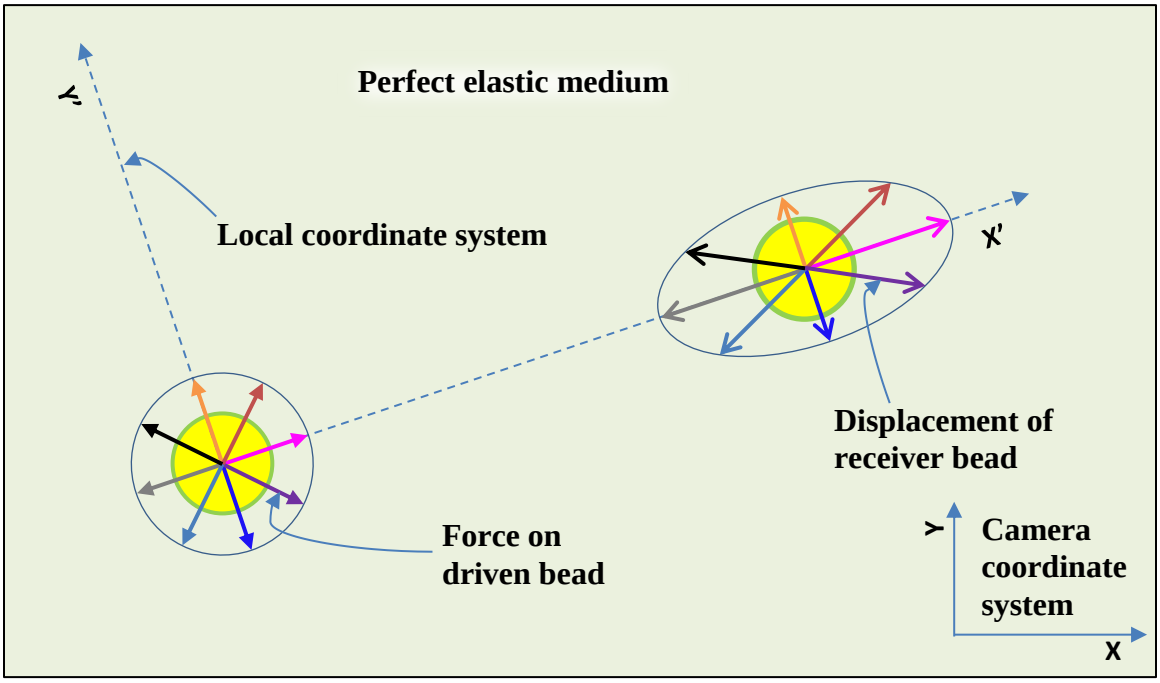

In the inherited method, bead displacements seemed inconsistent with linear elastic displacement theory when using Cheezum et al.'s correlation method in PAA gels. This is significant because PAA is widely reported to be homogenous, isotropic, and essentially linear elastic.[5,36] Measured displacements frequently closely approximated a linear relationship with applied force, but sometimes deviated greatly from a linear relationship. An example of apparently nonlinear response with the inherited method is shown in Figure 4.2a, which shows measured displacements of all non-driven beads in response to a set of force vectors of similar magnitude but different direction applied to Bead E. Measured displacement of Bead A is much larger for one trial than for any of the other trials, and involves a measured position outside the image frame. Additionally,

Beads B, D, and F exhibit noticeable deviations from linearity, with forces of similar magnitude and opposite direction producing measured displacements of visibly different magnitudes. It is worth noting that the worst discrepancy is for a bead near the image boundary. The inconsistency of measured bead position and displacement motivated an attempt to quantify uncertainty in measurements and to minimize sources of error.

Interactions of the correlation particle tracking with image edges was identified as a possible source of error in reported position, and similarly limitations in Fourier analysis were suspected sources of error when converting bead position data into amplitude values. Data processing begins with identification of bead position in each frame. Poor performance near edges suggested the possibility that the rectangular kernel in the inherited method was preventing a full correlation grid from being generated in those circumstances, leading to a low-quality fit and inaccurate final bead position. This hypothesis was corroborated with a reduced-size kernel, consisting only of the pixels corresponding to a bright region of a thresholded copy of the image frame. Simple background subtraction was also performed on each frame by subtracting the value of the darkest pixel in the frame from every pixel, effectively stretching the contrast in the final fit of correlation values for a minor improvement in fitting. Regarding Fourier analysis, common practice is to use the fast Fourier transform method on a signal with a sampling rate which is an integer multiple of the frequency of interest and a number of samples spanning an integer number of wavelengths. The data can then be “looped” to yield an infinite waveform for analysis. This was not possible for the optical trap apparatus and method because the image framerate was both variable and negatively dependent on the size of the field of view captured.

Figure 4.2: Raw CCD frame from a 1000-frame video, overlaid with data from six trials on the bead constellation. For each trial, scaled displacement vectors are shown for each bead except the driven bead, which has scaled force vectors shown. Displacement vectors begin at the calculated mean position of each bead. a) Position, force vectors, and displacement vectors from the Chz method. The calculated mean position for Bead A is outside the image frame for one trial, well outside the bright region for one trial, and varies by a few hundred nm between the remaining trials. The displacement vectors for each bead are grossly incompatible with elasticity theory, failing to trace the outline of an ellipse oriented towards the driven bead. b) Position, force vectors, and displacement vectors from the RefCor method. The calculated position of each bead in each trial appears to be near the respective bead center. The displacement vectors are compatible with elasticity theory, forming ellipses oriented towards the driven bead. The relationships between force on the driver and displacement of each receiver reported by RefCor are more consistent with elasticity theory than the relationships reported by Chz.

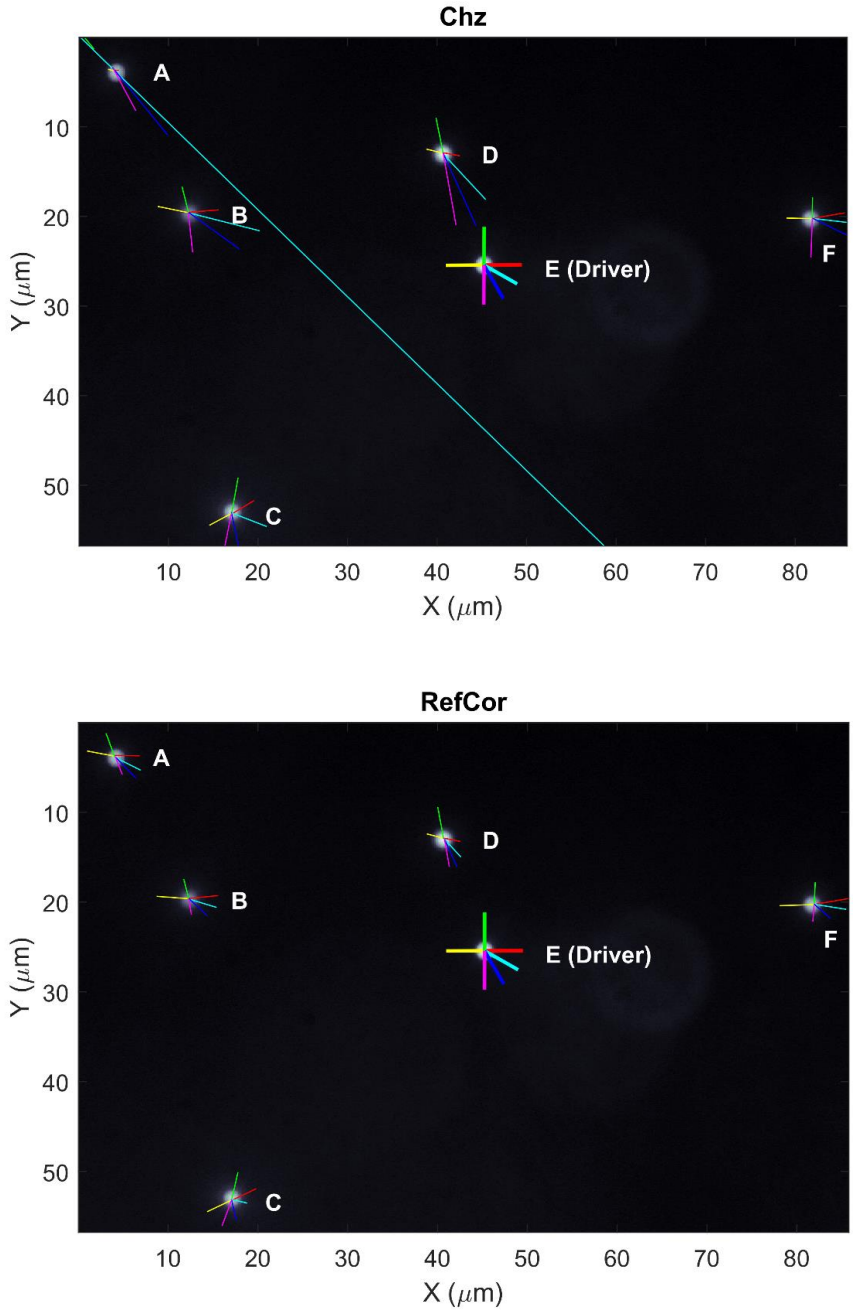

Methods

Experimental Data Collection

CCD videos with 1,000 time-stamped image frames were obtained of constellations of 2 µm diameter fluorescent beads in polyacrylamide gels (3% acrylamide, 0.05% bis-acrylamide) with one bead being driven sinusoidally by an optical trap.

Basic Explicit Fourier Analysis (BasicFA)

The CCD frame rate in experimental data was largely determined by the size of the field of view, rather than the frequency of interest, and was found to vary within a video, contraindicating use of the Fast Fourier transform. Instead, explicit Fourier analysis was performed using Equations 4.1 and 4.2. In these equations, X_i is the coordinate along one axis of the bead at time t_i, and f is the frequency for which amplitude should be calculated. Equation 4.1 yielded A_f, bead displacement amplitude in-phase with the trap driving force and Equation 4.2 yielded B_f, bead displacement amplitude out-of-phase with the trap driving force. These equations were applied to the displacement of each bead along each axis to determine in-phase and out-of-phase vector displacement of each bead.

$$\boldsymbol{A_f = \sum_{i=1}^{N} \frac{2}{\mathrm{N}} \sin(2\pi f t_i)\, X_i} \tag{4.1}$$

$$\boldsymbol{B_f = -\sum_{i=1}^{N} \frac{2}{\mathrm{N}} \cos(2\pi f t_i)\, X_i} \tag{4.2}$$

Refined Explicit Fourier Analysis (RefFA)

Although any frequency can be use in Equations 4.1 and 4.2, errors in calculated amplitude is introduced by signals with non-zero mean and/or spanning a non-integer number of periods. To minimize these errors, position information in RefFA was chopped to an integer number of periods and the mean value of the

remaining data points was subtracted from each data point ("zero-meaned") before calculating amplitude for any given frequency. This is illustrated in Figure 4.3. Except for this modification, analysis was identical to BasicFA.

Figure 4.3: Demonstration of a sinusoidal signal with arbitrary length and non-zero mean being adjusted to have an integer number of cycles and zero mean value.

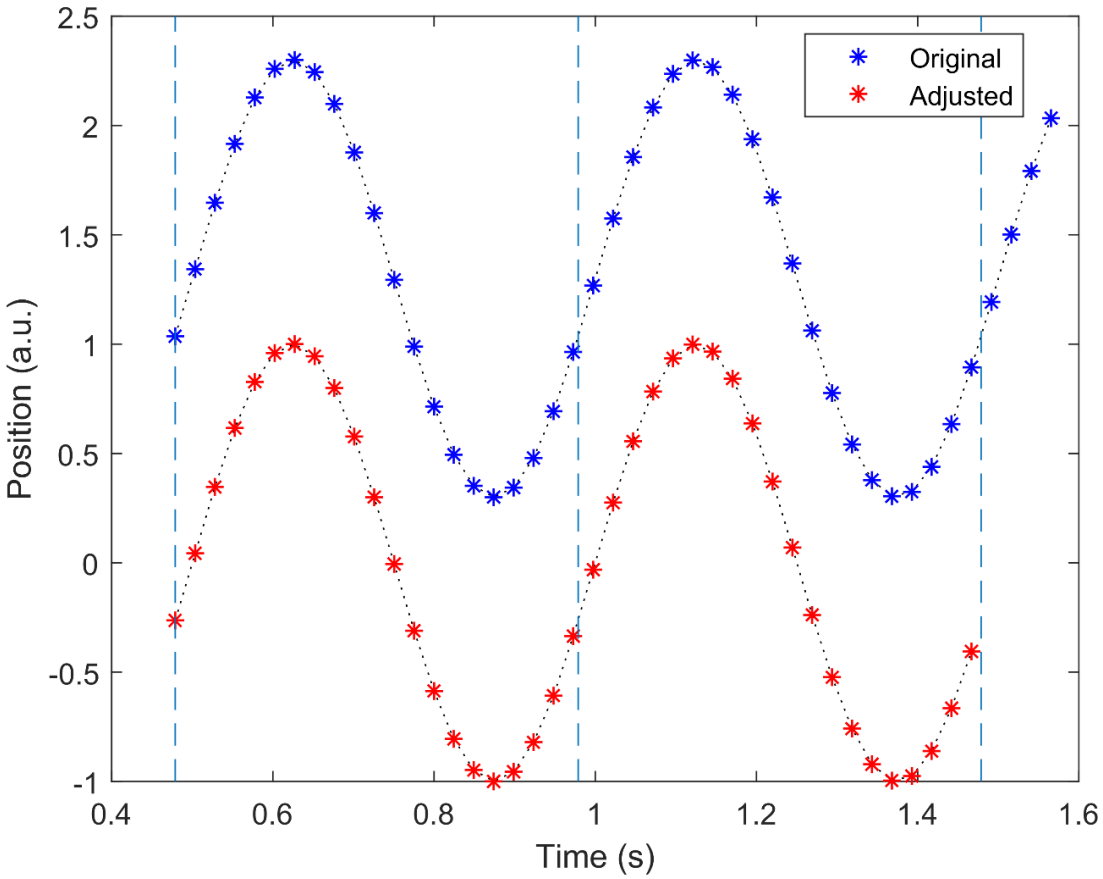

Estimation of Amplitude Noise

A method was established to estimate the uncertainty, or noise level, of amplitudes generated by Fourier analysis in noisy position data. In this method, the absolute values of Fourier amplitude peaks near the frequency of interest were ordered from lowest amplitude to highest amplitude and the absolute value of the peak at the 68th percentile was taken to be the noise in the amplitude measurement. This is shown in Figure 4.5**.** To minimize the effect of "signal leakage" from active driving at 2 Hz or higher harmonics in synthetic and experimental data, only peaks from 1-1.5 Hz and 2.5-3.46 Hz were included in the analysis. These frequency ranges are illustrated in Figure 4.4. A visual example of the uncertainty estimates generated by this method is provided by Figure 4.6, in which uncertainty of receiver bead displacement along both axes is indicated by an oval at the end of the corresponding displacement vector.

Figure 4.4: Illustration of the frequency ranges used to estimate uncertainty in measured displacement amplitude. The peak at 2 Hz is the driven bead displacement, with some amount of uncertainty which would be desirable to quantify.

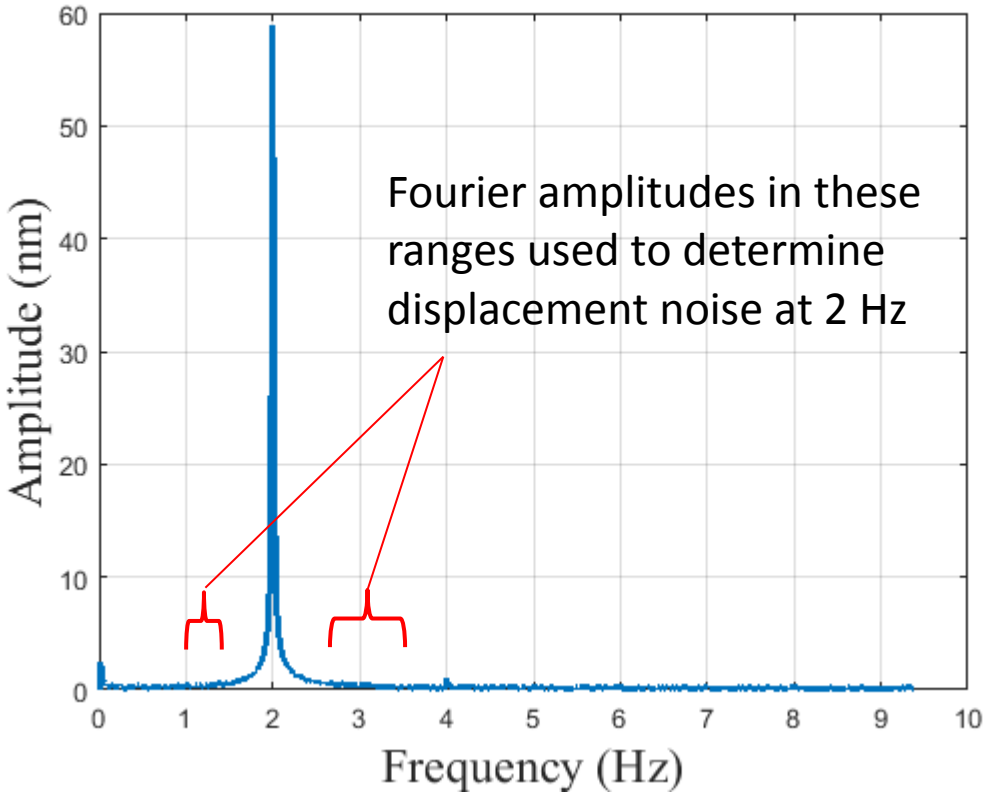

Figure 4.5: Fourier amplitude peaks from bead position data for frequencies from 1-1.5 Hz and 2.5-3.46 Hz, sorted from smallest to largest. The peak at the 68th percentile was taken to be the uncertainty in displacement for this bead along the Y direction for the trial from which these amplitudes were extracted.

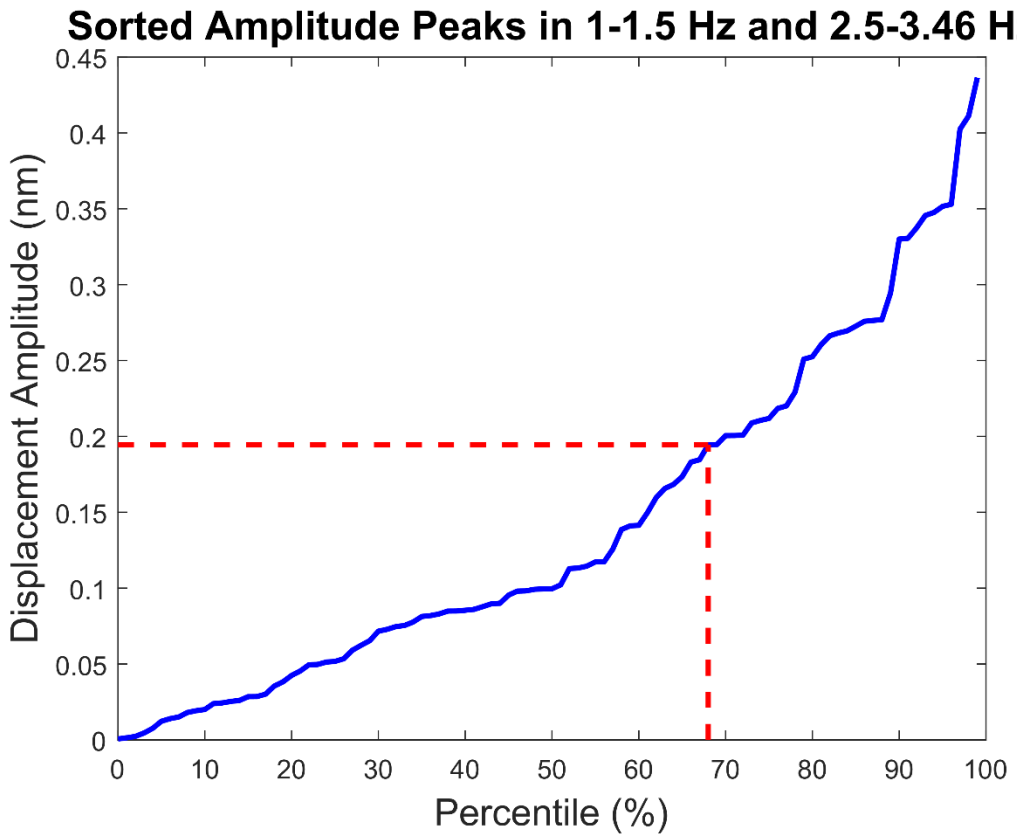

Figure 4.6: Visualization of displacement uncertainty with experimental data on a pair of 2 µm diameter beads. A driven bead, labeled "D", had several peak force vectors applied over the course of several trials which induced displacements in a receiver, labeled "R". Force vectors on the driver and displacement vectors of the receiver are paired by color, and both sets are scaled arbitrarily but uniformly to enable visualization. The uncertainty estimated from Fourier analysis can be seen as small ovals at the end of each displacement vector.

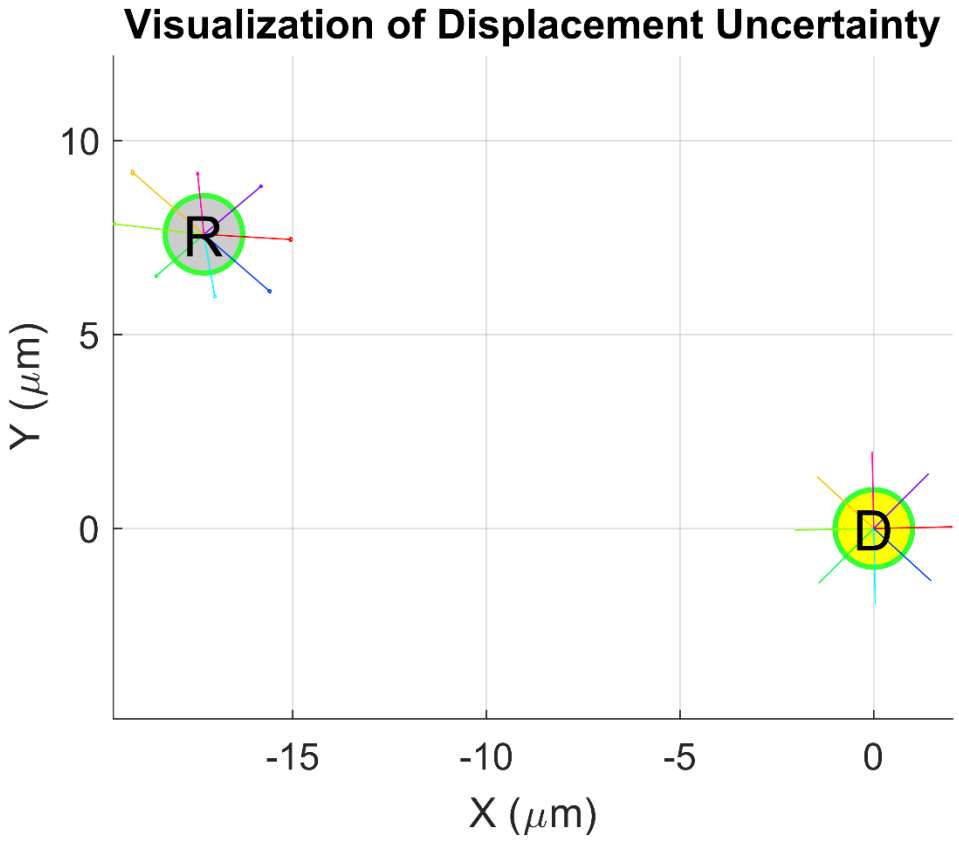

Synthetic Data Generation

Because the exact position of beads cannot be known in experimental data, synthetic data was generated to simulate real data with precisely known sinusoidal displacement and bead coordinates at each time point. 121-by-121 pixel, 1,000 frame videos were generated of a simulated bead oscillating sinusoidally at 2 Hz along the X direction at an amplitude between 1 and 60 nm (simulated pixel size of 75 nm) with a randomly generated starting position within 1 pixel of the image center. The 1,000 frames spanned a total time of between 20 and

50 seconds, with up to 0.5 ms of time delay randomly added to each individual frame. The simulated bead was generated as a 2D Gaussian with a peak brightness of 300 and a full width half max of 26.7 pixels. The simulated bead was overlaid on a constant background brightness between 30 and 80, and then shot noise was added to the resulting image. Shot noise was calculated per-pixel with normally distributed random values having zero mean and a standard deviation of 1-10% the square root of the brightness of the pixel for which the noise would be applied to.[22] In summary, synthetic videos with random frame timing were generated of a sinusoidally-displacing 2D Gaussian with background brightness and shot noise.

Centroid Particle Tracking

Conceptually, centroid particle tracking identifies beads and specifies precise bead position as the "center of mass" of the image brightness generated by each bead. The centroid tracking method was implemented essentially as described by Crocker and Grier.[23] The major steps are illustrated in Figure 4.7 under the "CG" label. First, a radius, *w*, was set to be 1.5 bead diameters. Boxcar averaging over a window width 2*w+1* pixels and Gaussian blurring with a half width of 1 pixel were applied simultaneously (Equations 4.3-5, copied from Crocker and Grier) to remove background brightness and reduce the impact of image noise.[23] Next, bead positions were roughly identified as the brightest pixel within radius *w* and above the threshold of 40% of the image contrast. For each bead detection, a disk-shaped region was cut out of the image with radius *w* and the interpolated position of the bead in that frame was specified as the brightness centroid of that disc. This was repeated for every frame and every bead. Consistent labeling of beads between frames was achieved by proximity to the position of an identified bead in previous frames.

$$\boldsymbol{K(i,j)} = \frac{\mathbf{1}}{\boldsymbol{K_0}\left[\frac{\mathbf{1}}{\boldsymbol{B}}\exp\left(\frac{-(i^2+j^2)}{4\lambda_n^2}\right) - \frac{\mathbf{1}}{(2w+1)^2}\right]} \tag{4.3}$$

$$\boldsymbol{K_0} = \frac{\mathbf{1}}{\boldsymbol{B}}\left[\sum_{i=-w}^{w}\exp\left(\frac{-i^2}{2\lambda_n^2}\right)\right]^2 - \frac{\boldsymbol{B}}{(2w+1)^2} \tag{4.4}$$

$$\boldsymbol{B} = \left[\sum_{i=-w}^{w} \mathbf{exp}\left(-\frac{(i^2+j^2)}{4\lambda_n^2}\right)\right]^2 \quad (4.5)$$

Inherited Correlation Particle Tracking

Conceptually, correlation particle tracking identifies a bead in a single image frame, creates a "kernel" (a region of the image containing at a variation in brightness generated by the bead,) and then defines bead position in those subsequent frames according to the position of the kernel at which its brightness variations best match the subsequent frame, which can be thought of as correlation strength. The inherited correlation particle tracking method was implemented essentially as described by Cheezum et al.[22] The major steps are illustrated in Figure 4.7 under the "Chz" label. In the first frame of every video, beads were identified as bright regions of size comparable to actual bead projected area after thresholding the image at 22% of total image contrast. The centroid of each region was determined to be the bead position in the first frame. The kernel for each bead was generated from a square image region, 81 pixels on a side, centered at the centroid of the thresholded region. Correlation strength at any an alignment (x,y) of the kernel center was defined by Equation 4.6, where $K_{i,j}$ is a pixel in the kernel and $I_{x,y}$ is a pixel of the image frame in which the bead position is being specified by correlation. Correlation for each bead in subsequent frames was performed with the kernel aligned exactly as in the original image, and at integer pixel position differences along X and Y to create a 31-by-31 grid of correlation strength values. The correlation strength values were fitted against (X,Y) coordinates using a 2D paraboloid, and the precise bead position was defined as the peak value of the paraboloid. This was repeated for each bead and each frame after the first frame.

$$\boldsymbol{C_{x,y}} = \sum_{i=-m}^{m}\sum_{j=-n}^{n} \boldsymbol{I_{x+i,y+j}K_{i,j}} \quad (4.6)$$

Refined Correlation Particle Tracking

This method is based on the inherited correlation particle tracking method, with the primary change being a smaller, non-rectangular kernel. Additionally, each frame of the video had the value of the darkest pixel in that

frame subtracted from the value of each pixel in that frame before any other processing steps. Frames with this simple background subtraction performed are referred to just as “frames” for the remainder of this description. Thresholding at 22% of total image contrast was applied to a copy of the first image frame to which Gaussian blurring had been applied with a standard deviation of 1 pixel. The list of pixel coordinates of each appropriately-sized bright region in this thresholded image was recorded and kernels were generated for each bead from a non-blurred copy of the first frame. Correlation for each bead in subsequent frames was performed with the kernel aligned exactly as in the original image, and at integer pixel position differences along X and Y to create a 31-by-31 grid of correlation strength values. The correlation strength values were fitted against (X,Y) coordinates using a 2D Gaussian, and the precise bead position was defined as the peak value of the Gaussian. This was repeated for each bead and each frame after the first frame. The major steps are illustrated in Figure 4.7 under the “RefCor” label.

Figure 4.7: Comparison of the main steps in CG, Chz, and RefCor. In CG, each frame is processed identically, in isolation from any other frame. The steps are: blurring and boxcar averaging the image; roughly identifying particle centers as the brightest pixel within a preset radius and cutting out a disc of the same radius; and defining precise bead position as the brightness centroid of that disc. In Chz, each bead in each frame is compared to the same bead in the first frame. The steps are: identify a bright region in Frame 1 and make a kernel of a fixed-size square centered on the bright region; scan the kernel over another frame while recording the match quality at each location; and define precise bead position by fitting match quality versus position to a paraboloid. In RefCor, the same steps are followed as in Chz, except each kernel is a region above a preset brightness threshold, the minimum brightness in each image is subtracted from each pixel in that image, and the fine position of a bead is found in step 3 by fitting match quality versus position to a two-dimensional Gaussian.[22,23,37,38]

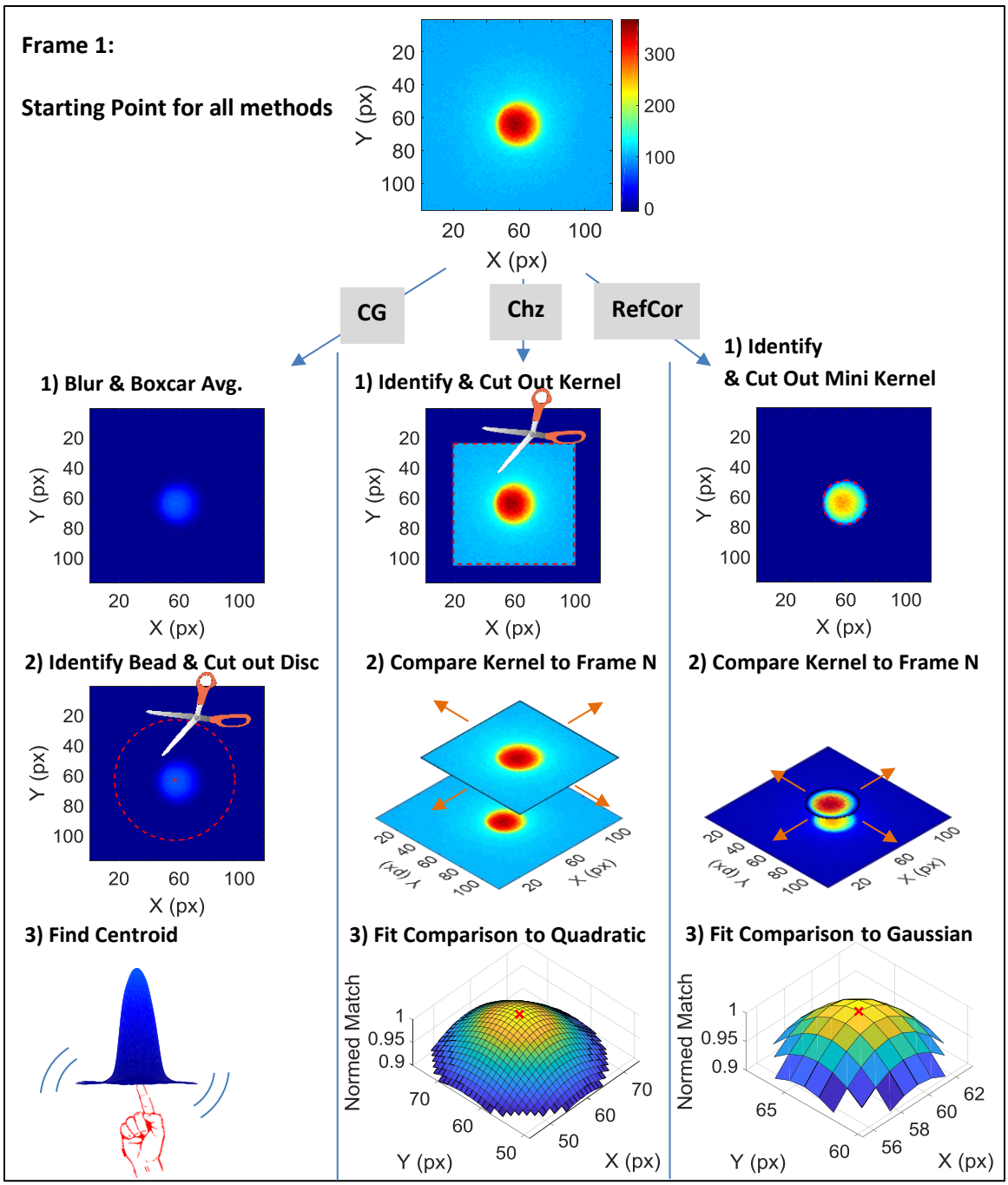

Results and Discussion

The performance of the three particle tracking methods and two Fourier analysis variants was tested in three steps. First, the two variants of Fourier analysis were applied to perfectly sinusoidal time traces with random amplitude, random offset, and random sampling frequency. Next, performance of the three particle tracking methods was compared on synthetic data. Finally, uncertainty in calculated amplitude was defined using refined Fourier analysis on time traces resulting from use of the two correlation tracking methods on experimental data.

Basic versus refined explicit Fourier analysis

Even with a perfectly sinusoidal signal and a constant frame rate, BasicFA produced erroneous results. Figure 4.8 shows the amplitude reported using Equation 4.1 on set of position values collected at 34.7 from a perfect 2 Hz sinusoidal signal with amplitude 1 and offset 100. After collection of 181 data points at 5.216 seconds, the error in reported amplitude was over 600%. Even at almost 30 seconds, errors over 100% were observed. It was hypothesized that this error was a result primarily of a non-zero mean and a non-integer number of cycles.

Adjusting the signal to address either greatly reduced the error. Figure 4.9 shows the result of subtracting the mean position value ("zero-meaning") from the data shown in Figure 4.8, while Figure 4.10 shows the result of truncating the data at the largest possible integer cycle count. In the same time span which saw peak error slowly drop from over 600% to just over 100%, peak error with a zero-meaned signal started out at approximately 1% and dropped to approximately 0.2%. In the case of signal truncation, error in the same time span started out at just under 5% and dropped to about 0.8%.

Combining the zero-meaning and signal truncation to create RefFA resulted in peak error starting at 0.45% and dropping down to 0.1%. This is shown in Figure 4.11. Because of the scale of improvement over BasicFA, RefFA is used for the remainder of this document.

The caveat to this analysis and demonstration of improvement is that it was performed on a perfectly sinusoidal signal with a fixed start time of 0 seconds and at a perfectly stead sampling rate. Real data is not so ideal and will likely show increased error for every case, although RefFA does not seem likely to have error anywhere near the magnitude of error of BasicFA.

Figure 4.8: Amplitude reported for a 2 Hz signal versus data collection time with an unmodified signal.

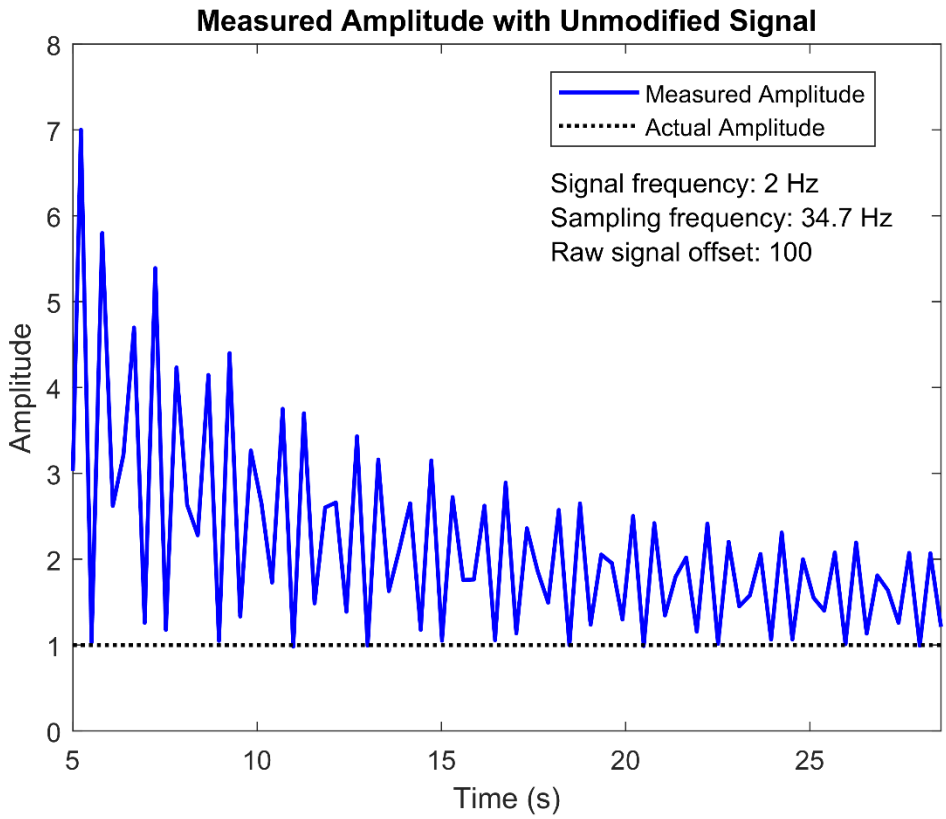

Figure 4.9: Amplitude reported for a 2 Hz signal versus data collection time with a signal from which the mean value of all data points has been subtracted.

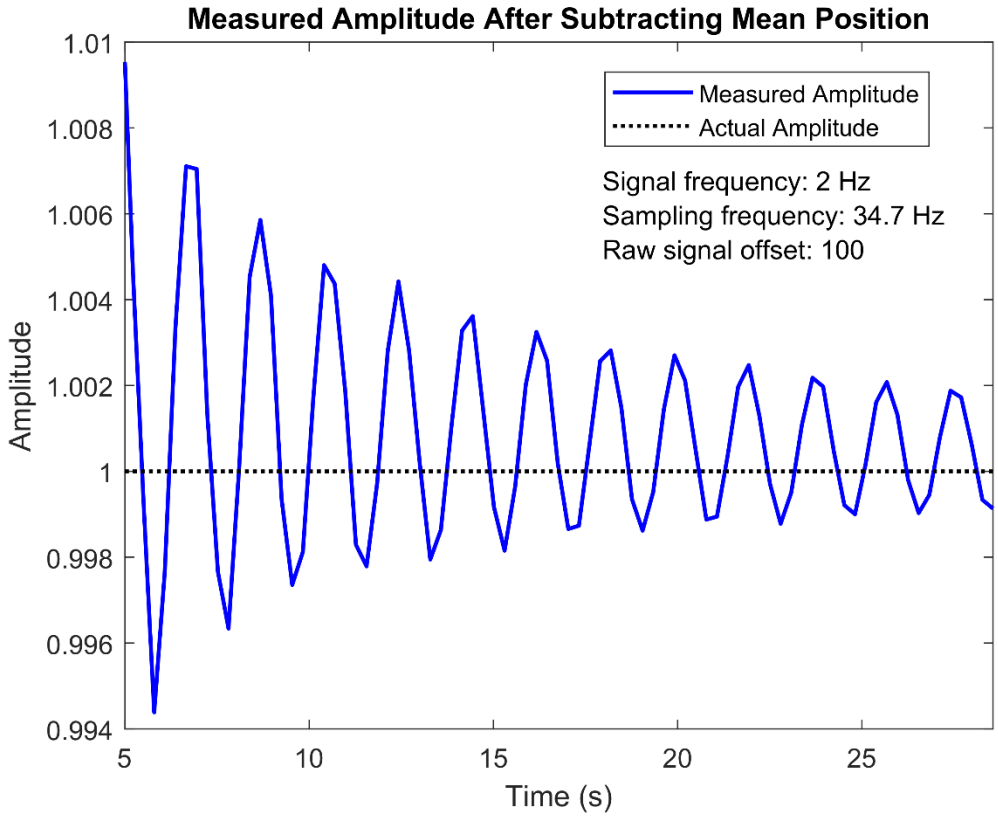

Figure 4.10: Amplitude reported for a 2 Hz signal versus data collection time with a signal which has been truncated at the largest possible number of integer cycles.

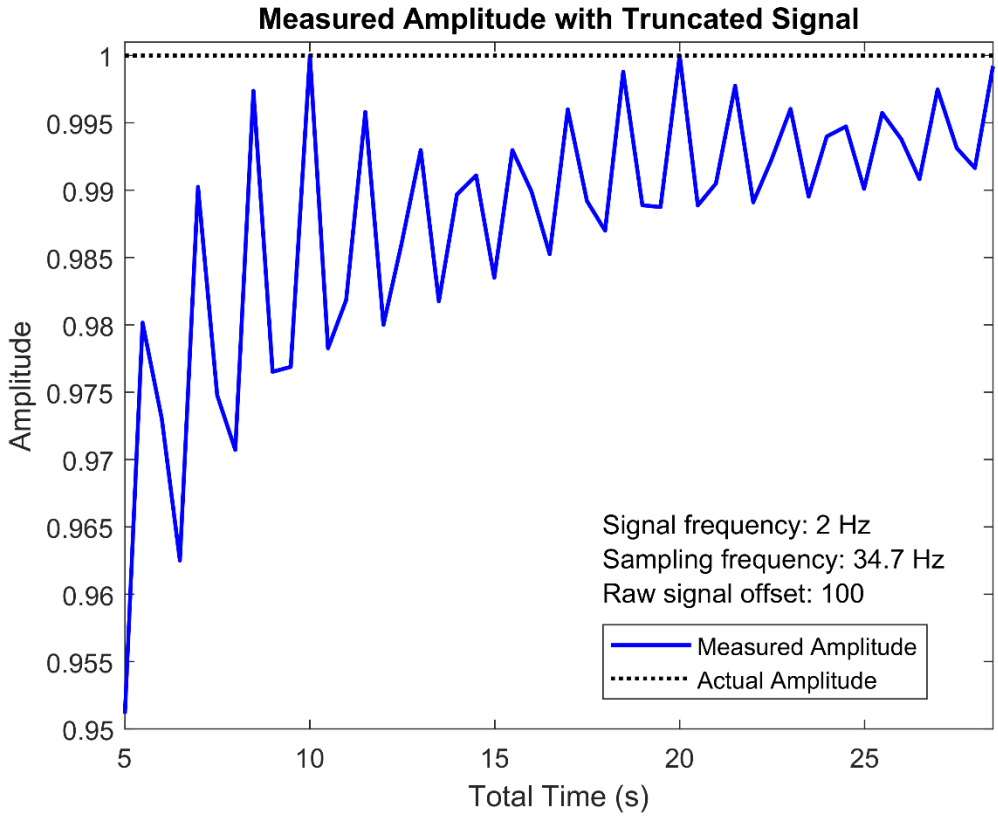

Figure 4.11: Amplitude reported for a 2 Hz signal versus data collection time with a signal which has been truncated to the largest possible number of integer cycles and then had the mean value zeroed.

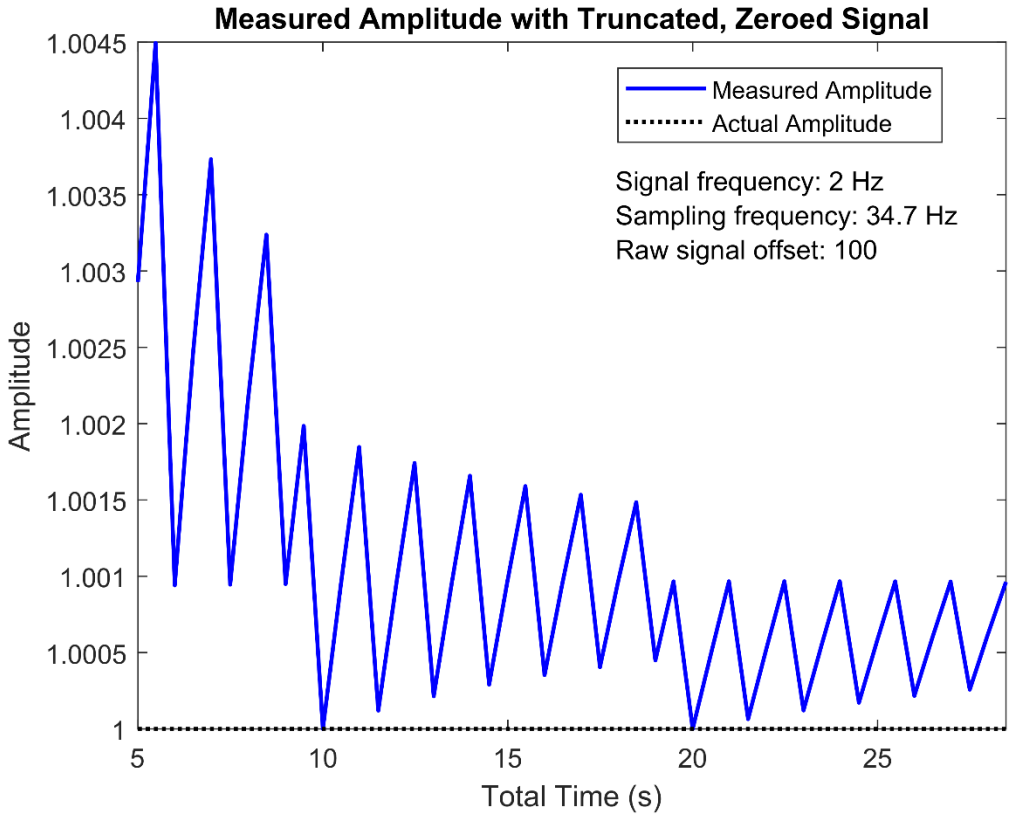

Visual Estimation of Fourier peaks

In the process of examining Fourier amplitudes, it was discovered that it is critical to measure the amplitude of a peak at exactly the frequency of interest, rather than relying on visual estimation of peak height. For each receiver (non-driven) bead examined, the Fourier spectrum out of phase with force application to the driven bead appeared to have a peak almost as large at the driving frequency as the spectrum in phase with force application. This can be seen by comparing Polyacrylamide, the material in which the beads were embedded, is widely reported to be nearly linear elastic, making this a confusing observation. Closer observation revealed

that the actual amplitude of the out-of-phase displacement component at 2 Hz was much smaller than rough visual examination would reveal, and that a “valley” was formed by signal leakage from the 2 Hz in-phase signal to nearby frequencies in the out-of-phase spectra. This discovery of erroneous peak estimation made it clear that Fourier peaks could not be visually estimated, but instead must be reported directly at the frequency of interest.

Figure 4.12: The in-phase Fourier amplitude spectrum of a receiver (non-driven) bead resulting from a 2 Hz sinusoidal force applied to the driven bead primarily along the X direction.

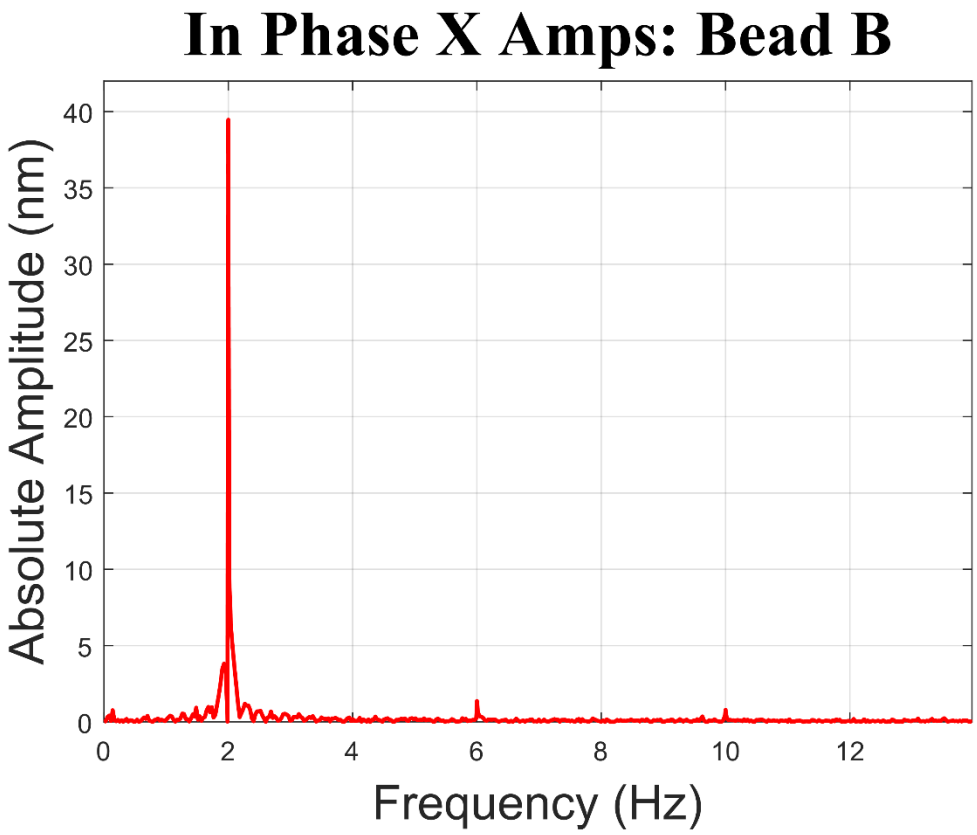

Figure 4.13: The out-of-phase Fourier amplitude spectrum of the same receiver (non-driven) bead and trial in Figure 4.12, which resulted from a 2 Hz sinusoidal force applied to the driven bead primarily along the X direction. The out-of-phase component of displacement at 2 Hz appears to be approximately 27 nm, almost as large as the approximately 39 nm in-phase peak.

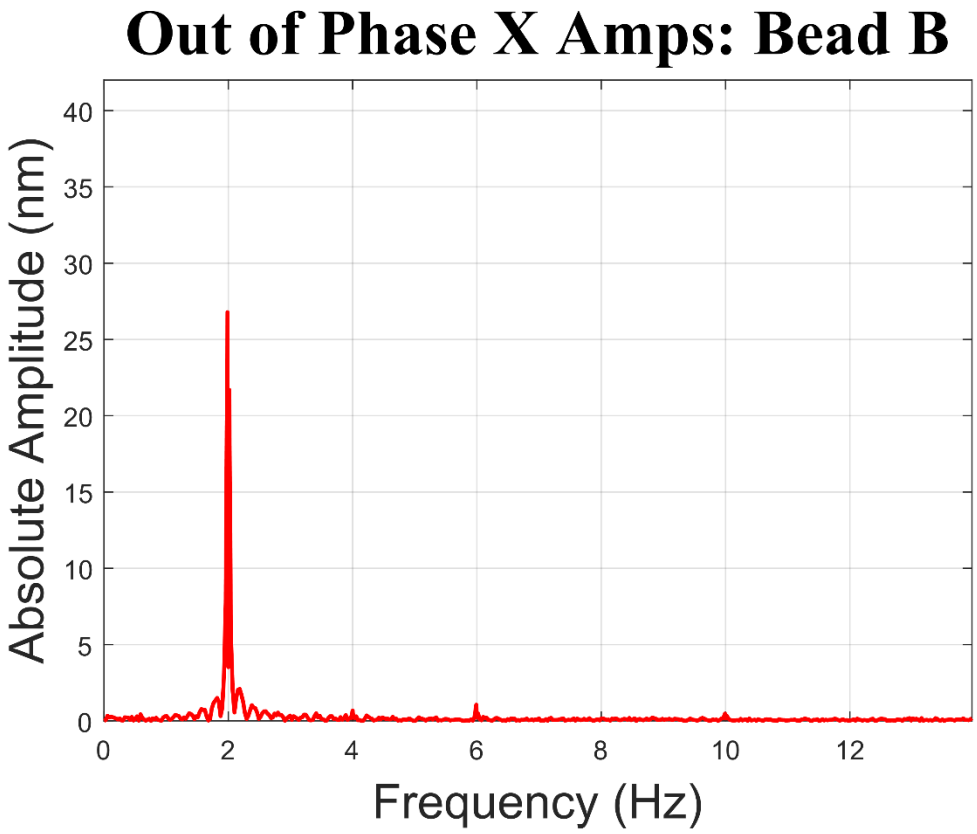

Figure 4.14: A zoomed in view of the out-of-phase Fourier amplitude spectrum of a receiver (non-driven) bead shown in Figure 4.13, which resulted from a 2 Hz sinusoidal force applied to the driven bead primarily along the X direction. Stretching the frequency scale reveals that the out-of-phase amplitude at 2 Hz is actually 3.5 nm, not the 27 nm it could have been mistaken for in Figure 4.13.

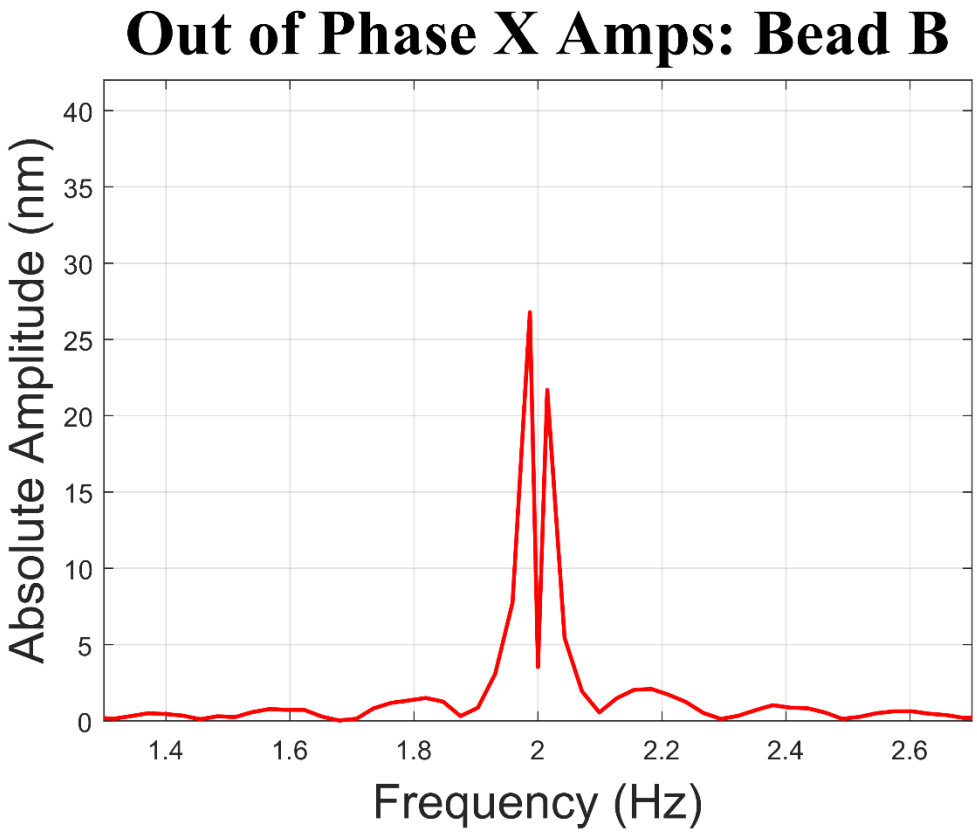

Particle tracking performance on synthetic data

The three particle tracking methods and RefFA were applied to synthetic data which had been designed to roughly simulate experimental data. The simulated data had a rotationally symmetric, bright "bead" oscillating in front of a bright background with simulated imaging noise added per-pixel.

Representative time traces from the three tracking methods to synthetic data are shown in Figure 4.15. The presence of a sinusoidal signal in centroid tracking data is not obvious, while both correlation methods very

closely reflect the actual position, with sustained offset and some level of per-frame noise. The average difference in position across 20 trials was 8.3 ± 22.1 nm for centroid tracking, 7.1 ± 23.5 nm for inherited correlation tracking, and 7.8 ± 22.9 nm for refined correlation. The differences in mean positions reported by the three methods are not important for multi-particle optical rheometry, as only relative position between beads – on the scale of 10,000 nm – enters into any calculations.

More important are the amplitudes of displacement obtained at the frequency of driven oscillation. Values of calculated in-phase bead displacement amplitude versus actual displacement are shown in Figure 4.16 for the three particle tracking methods applied to synthetic data with refined explicit Fourier analysis. Over the span of 40 trials, the mean difference between actual and measured displacement amplitude was 0.114 ± 2.026 nm for centroid tracking, 0.019 ± 0.198 nm for inherited correlation tracking, and 0.015 ± 0.134 nm for refined correlation tracking. No trend was found versus actual amplitude. On an average sense, all three methods produced accurate values. Refined correlation tracking had slightly higher precision than inherited correlation tracking, and both were approximately an order of magnitude more precise than centroid tracking.

Even the comparatively poor performance of centroid tracking in comparison to the correlation methods was actually a demonstration of the ability of Fourier analysis to de-noise a signal. The results of centroid tracking had hundreds of nm of “fuzz” obscuring the sinusoidal signal, yet Fourier analysis constantly extracted a displacement amplitude within a few nm of the actual displacement amplitude.

Figure 4.15: Time traces of bead position as obtained by applying the three tracking methods on synthetic data, overlaid with the actual position of the synthetic bead.

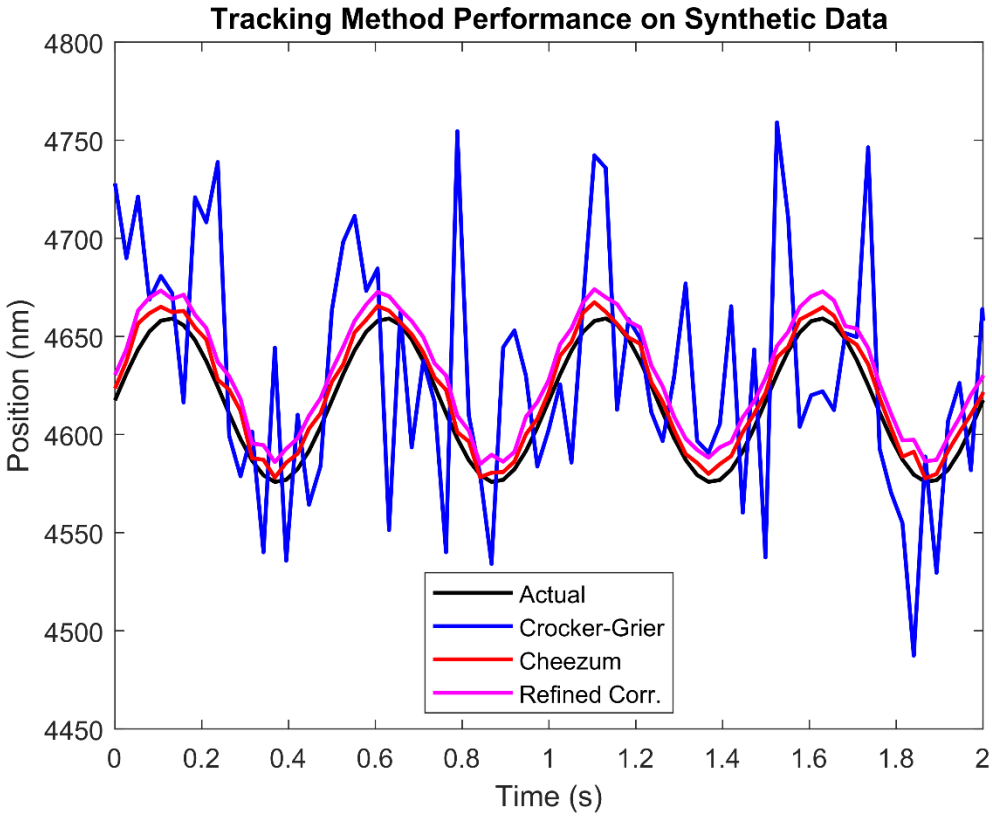

Figure 4.16: Actual and reported displacement amplitudes of bead displacement in synthetic data using Crocker and Grier's centroid particle tracking, Cheezum's correlation particle tracking, and the refined method of correlation particle tracking.

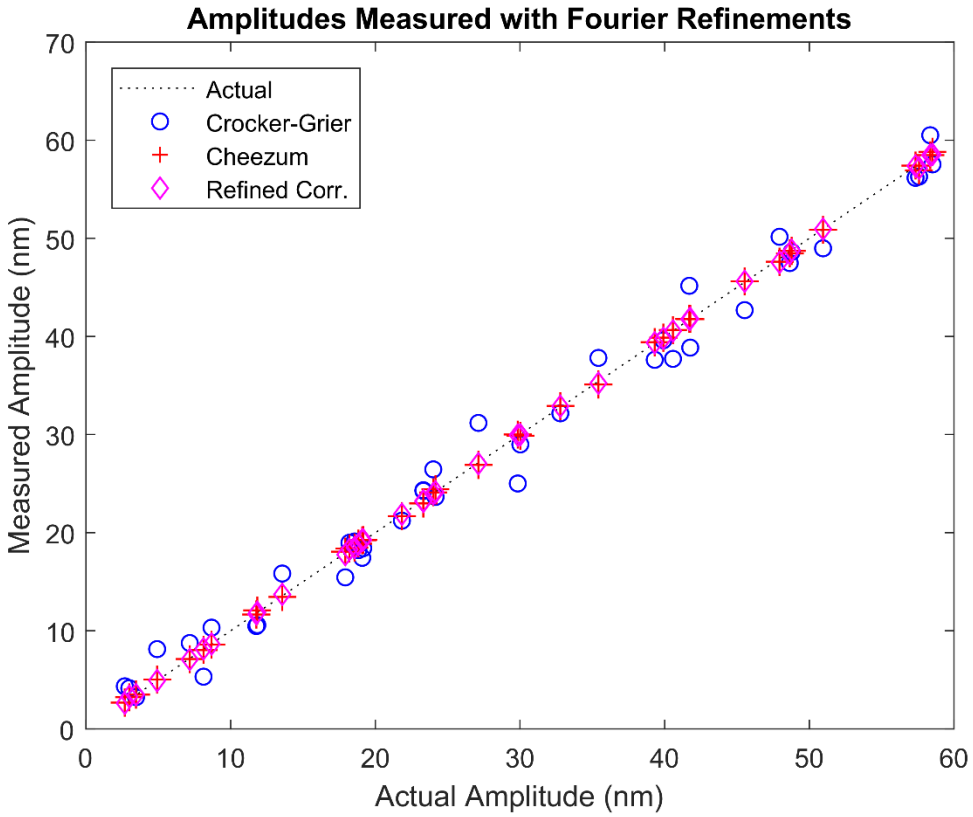

Displacement uncertainty estimates in experimental data

As exact position and displacement were not possible to determine in experimental data, only an estimate of uncertainty ("noise") in bead displacement was examined. Experimental data consisted of constellations of beads in polyacrylamide gels, with one of the beads driven sinusoidally and the rest moving passively as a result of the displacement field of the gel. The data was processed using the two correlation methods in conjunction with RefFA. Uncertainty in amplitude for refined correlation was compared against inherited correlation with and without image boundaries impinging on the correlation grid.

Refined correlation yielded amplitude measurements with very slightly lower noise than inherited correlation when an image boundary did not impinge, but the impingement of an image boundary greatly increased the mean noise for the inherited correlation method. The mean noise for refined correlation was 0.39 ± 0.35 nm, while the mean noise for inherited correlation away from a boundary was 0.39 ± 0.36 nm and the noise for inherited correlation impinged by a boundary was 0.84 ± 8.6 nm. The relationship between noise from refined correlation and noise from inherited correlation with/without impingement is shown in Figure 4.17. A very small decrease in noise from inherited correlation to refined correlation was observed, not worth pursuing when an image boundary is not present, but the apparent benefit of refined correlation is clear in the presence of an image boundary.

Anecdotal, indirect evidence suggests that refined correlation may produce more accurate measurements of bead displacement, regardless of noise measurements. Figure 4.2a and b show displacement patterns as measured by both the inherited and refined correlation methods, respectively. Beads far from an image edge which would not be affected by impingement still have measured displacements in the inherited correlation case which are less consistent with elasticity theory than the displacements seen in the refined correlation case. A hypothesis was conceived that patterns, such as brightness from out-of-focus beads, in the background affected the large kernel of inherited correlation more than the smaller kernel of refined correlation. Unfortunately, this hypothesis was not able to be tested in the limited time allotted for this study. This indirect evidence weakly adds to the preference for refined correlation.

The optimum combination of particle tracking and Fourier analysis for micron-scale fluorescent beads is refined correlation followed by RefFA. Both the inherited and refined correlation significantly outperform centroid tracking, but refined correlation is more precise in the presence of image edges and may be more accurate in certain cases which have not been well defined as yet. For the step of measuring amplitude from position data, RefFA greatly outperforms BasicFA. Additionally, Fourier amplitude peaks should be reported at exactly the frequency of interest, rather than relying on visual estimation. These findings are shown in Figure 4.15.

Figure 4.17: Displacement noise of individual beads for refined correlation or inherited ("Cheezum") with/without image impingement plotted against the noise for that same bead when using refined correlation. There are small differences between refined correlation and unimpinged inherited correlation. There are dramatic increases in noise for some beads with impinged inherited correlation, including one case with noise measured at 246.8 nm.

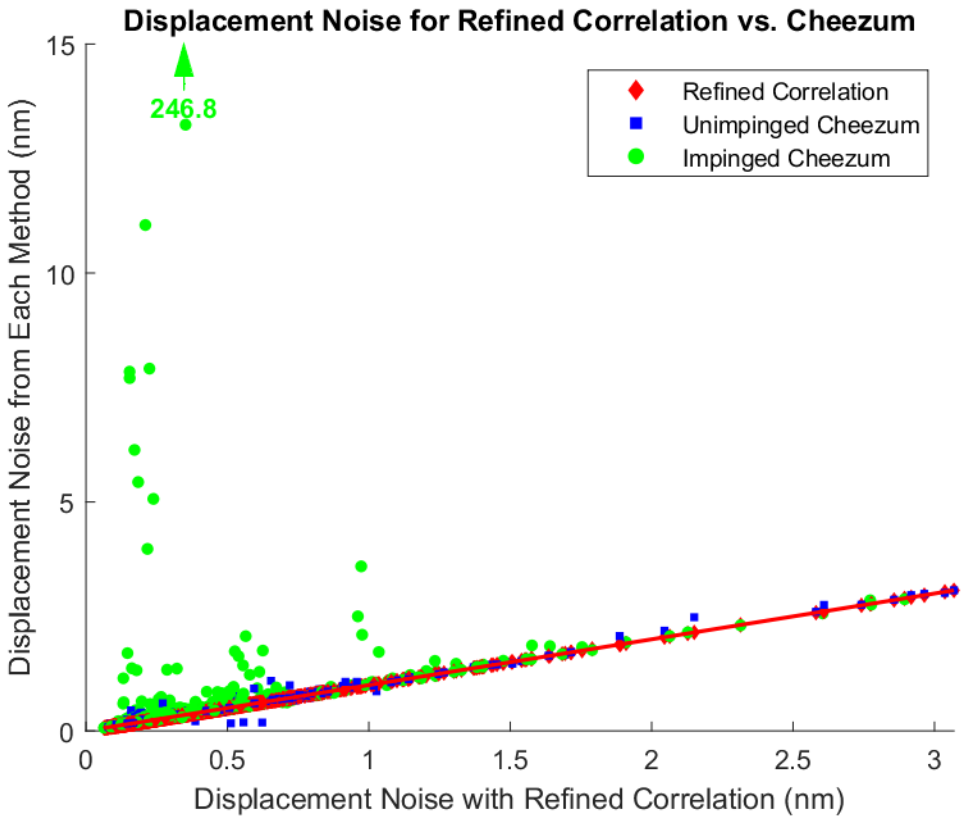

Table 4.2: Findings in measuring bead position and displacement.

Finding	Description	Impact
Correlation tracking more precise than centroid tracking.	In a comparison of tracking methods on synthetic data, the correlation method consistently tracked bead position while centroid tracking suffered from large, seemingly random fluctuations in reported position.	Correlation particle tracking should be used in place of centroid tracking.
Reduced template size improves performance near image edges	Tracking performance with a small template was much improved near image edges and indistinguishable otherwise.	Small templates should be used in place of large templates for more robust tracking performance.
Fourier analysis compensates for shortcomings of particle tracking	In a comparison of tracking methods on synthetic videos of a bead undergoing sinusoidal displacement, Fourier analysis yielded a displacement amplitude within 5 nm of the actual amplitude for position traces which had random fluctuations spanning hundreds of nm.	Even with high noise in particle position data, Fourier analysis of sinusoidal bead driving can recover an amplitude very near the actual value.
Simple background subtraction increased tracking precision by a negligible amount.	Subtracting a constant background brightness reduced uncertainty in reported amplitude by picometers when using the correlation method of particle tracking.	The small benefit of simple background removal in high signal-to-noise images should only be considered when precision is critical.
Exact frequency in Fourier analysis	Visual examination of Fourier spectra was found to sometimes result in displacement amplitude estimates off by an order of magnitude.	When the image acquisition rate is not precisely matched to the driving frequency, explicit Fourier analysis must be performed at the exact frequency of interest.

Chapter 5 : Measuring the Trap Force Landscape

Introduction

The purpose of this chapter is to demonstrate practical measurement of optical trap force as a landscape, which can justify application of higher forces than typically used in optical trap microrheology by maintaining precise knowledge of the force applied at any moment. The force an optical trap exerts on a bead depends on offset, the position difference between the trap center and a bead, as shown in Figure 5.1. This relationship can be considered linear for small offsets, commonly considered to extend out to 100-200 nm. Use of optical traps is commonly restricted to this range with the intention that a single measurement of trap force versus position offset can define force over the entire regime. A major limitation of this strategy is that it limits trap force to a fraction of the maximum force available, which occurs at larger offsets. Another limitation is that the state of the art in trap force calibration is prone to large error, as shown in Figure 5.2.[30] On top of that, the trap may not be linear over the assumed range due to issues with beam alignment or shape, may not have a different linear stiffness in the range used in experiments than calculated if the measurement reflects force at an offset outside the range, or may be anisotropic which cannot be detected from a measurement along a single direction. Measurement of the trap force as a landscape is the key to use of higher trap forces with knowledge of the force at any offset.

Measuring a trap force landscape requires that force versus offset be measured at many offsets, with implicit requirements of accuracy and sufficient precision in each measurement to resolve detail in the landscape. Both ray optics and T-matrix theory predict a monotonic relationship between trap force and offset between the points of peak force, suggesting that densely spaced measurements along either axis can result in accurate

mapping of the other quantity. As the most common method of measuring trap force is use of Stokes' Law on a bead dragged through water with laminar flow, a natural tactic for achieving densely spaced measurements is continuous variation in fluid velocity with instantaneous measurement of offset.

Figure 5.1: A bead in the energy well generated by an optical trap. The bead is at the bottom of the energy well when its center is along the axis of beam propagation and slightly past the beam waist along the axis of propagation. Displacement (offset) of the bead relative to this position in any direction is "climbing" the energy well, resulting in a force vector on the bead equal to the slope of the energy well at that point. This force is linear versus offset for sufficiently small offsets.

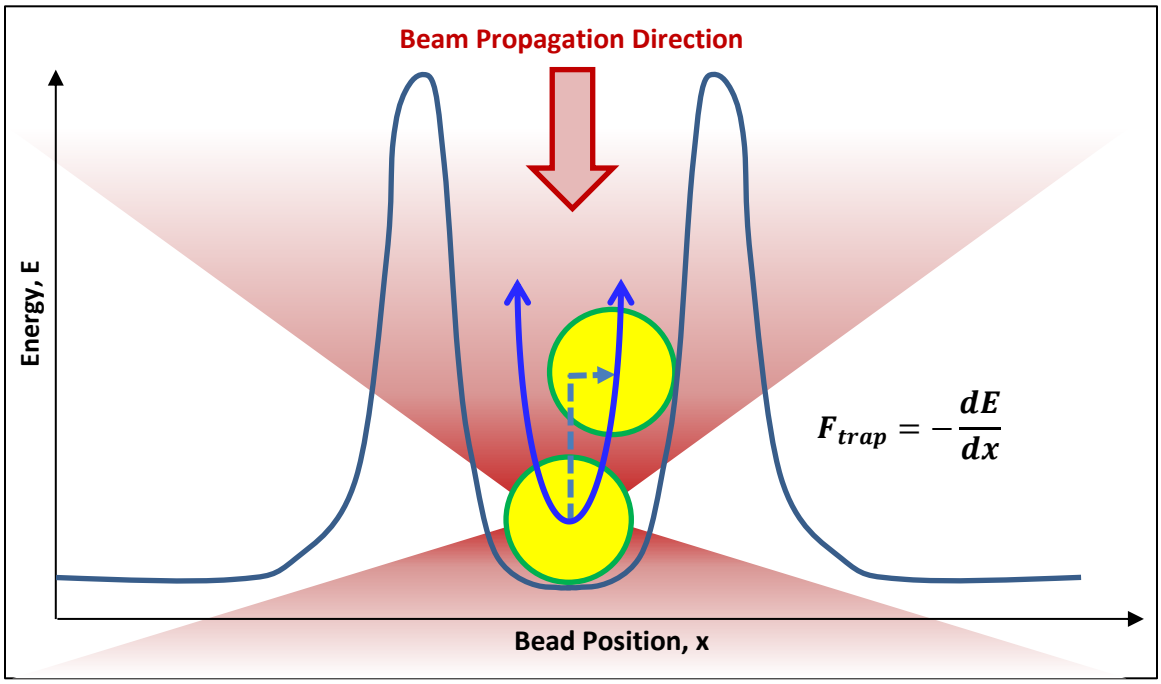

Figure 5.2: Trap force spring constant measurements made by Velegol and Lanni using a state of the art method. The spring constant was determined to be 100 µN/m for small offsets.[30]

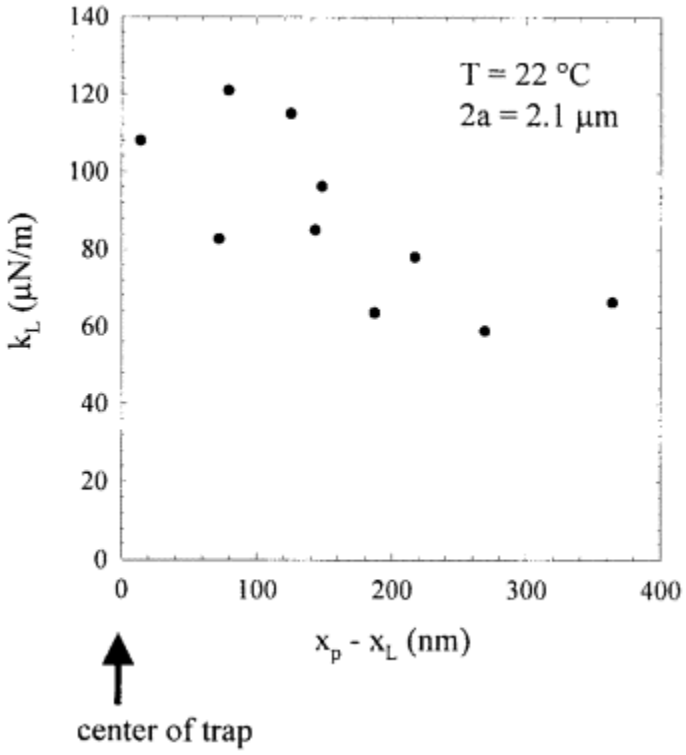

This chapter demonstrates measurement of a trap force landscape achieved via calibrated, sinusoidal fluid flow combined with video particle tracking to get a dense path of bead position versus drag force. The innovations involved are summarized in Table 5.1. Qualitative comparison is made to theoretical calculations of trap shape.

Table 5.1: Innovations in measuring the trap force landscape.

Innovation	Description	Impact
Sinusoidal stage displacement	The microscope stage was commanded to displace sinusoidally while a bead was held nearly stationary by the optical trap in a water-filled chamber on the stage.	Sinusoidal stage displacement generates spatially uniform cosinusoidal fluid velocity which varies continuously from minimum to maximum values.
Trap force downscaling	Uniform downscaling of trap force was achieved by reducing beam power through rotation of a half-wave plate upstream of a polarizing beam splitter.	Reduced trap force allows the laminar, low-velocity fluid flow from the stage displacement to match the trap force at arbitrarily large bead-trap offsets.
Mapping force versus bead offset	Instantaneous negative drag force and smoothed bead position were plotted against each other to generate a map of trap force versus bead-trap offset	This results in a detailed, full-span map of trap force versus bead-trap offset, allowing quantification of trap force nonlinearity.

Methods

Optical trap apparatus

There are a number of key components of the apparatus, centered on a microscope with a piezo-actuated stage. The apparatus is shown in Figure 5.3. The optical trap itself is generated by a laser beam which is steered by galvanometric mirrors and expanded in a telescope region before entering the objective lens, which focuses the beam to a waist a few hundred micrometers past the lens surface. Fluorescence of the beads which the trap acts upon is induced by a mercury lamp and a FITC filter. Images of those same beads are obtained by a CCD camera placed after filters which block laser and mercury lamp light so only bead fluorescence is visible. Filters for laser light can be removed to assist in identifying the position of the trap. The stage and galvanometric mirrors are controlled by LabVIEW programs, and imaging is controlled using µManager.[25]

Figure 5.3: The optical trap apparatus, centered on a microscope with a piezo-actuated stage. The laser beam which forms the trap passes through an optical diode, a half-wave plate, and a polarizing beam splitter before being reflected off the two galvanometric steering mirrors, expanded in a telescope, and entering the objective lens. The beam is focused to a waist a few hundred micrometers above the objective lens, where it forms the optical trap. Fluorescense is excited light from a mercury lamp passed through a FITC filter. Imaging is achieved by a CCD camera with filters to pass in only light from bead fluorescence.

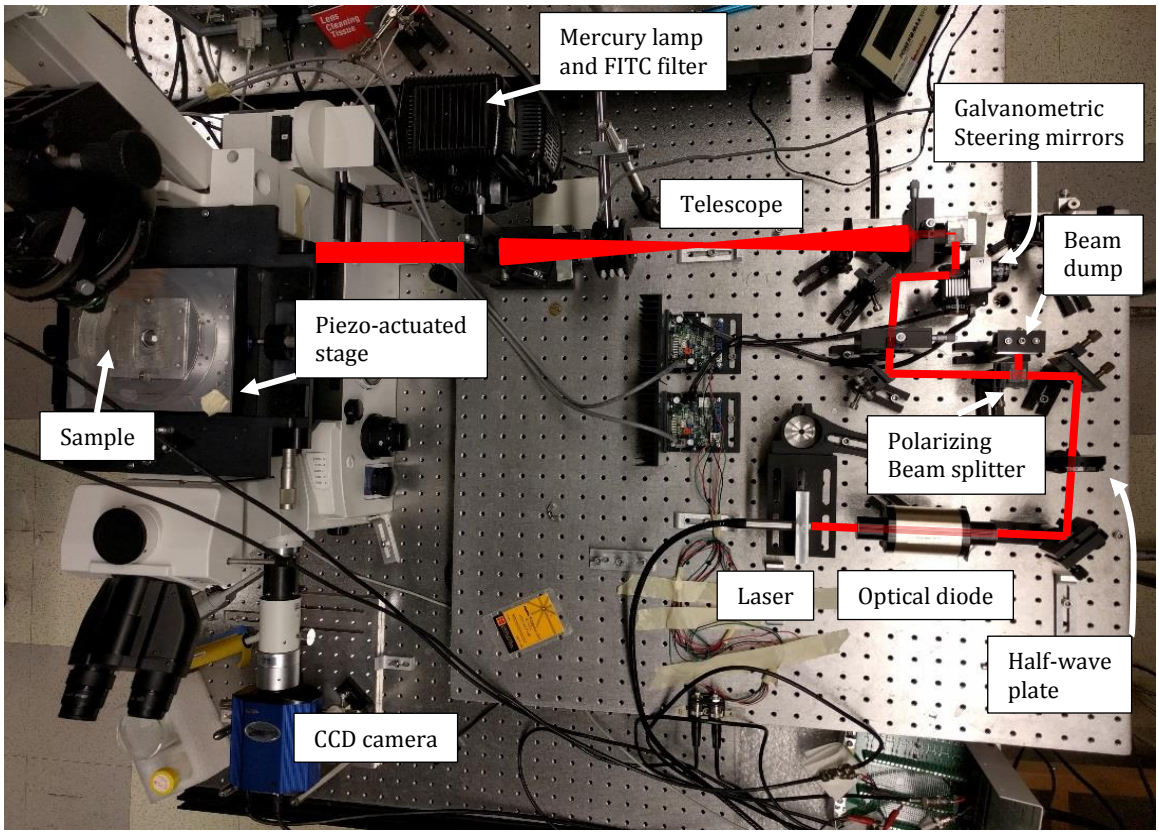

Calculation of trap force versus bead position

Trap force on a bead is calculated indirectly by causing fluid flow over the bead and calculating the drag force being applied, which can then be matched to the bead position observed at that time. For sufficiently low fluid velocities, which will apply to all trap force calibrations with micron-sized beads, laminar flow can be assumed and Stokes' law specifies drag force. This is shown in Equation 5.1, where F_{drag} is the drag force, η the dynamic viscosity of the fluid (water), a the bead radius, and v the relative velocity of the fluid with respect to the bead.

$$F_{drag} = 6\pi\eta a v \quad (5.1)$$

Measuring stage position and velocity

Fluid flow over the bead is generated by holding the bead nearly stationary using the optical trap in a fluid-filled chamber on the microscope stage as the stage is moved using piezo actuation. The velocity of the fluid, which is identical to the stage velocity, is used in calculation of trap force versus bead position and thus requires measuring stage position and velocity.

Displacement is observed by drying a dilute bead solution on a cover slip and capturing video of a single bead during stage displacement. Position over many (sinusoidal) cycles of displacement are measured and fitted with a sin series of arbitrary order with phase lag information. This yields a nearly exact position at every moment throughout the cycle, allowing stage velocity to be calculated as the derivative of stage position. The precise steps are described in Appendix A: Protocols under the "Measuring the Trap Force Landscape" sub-heading.

Measurement of trap force as a landscape

The major steps in the process are:

1. Measurement of stage position while commanding sinusoidal stage displacement, followed by fitting stage position to a sin series with phase information and then differentiating the sin series to obtain stage velocity at every moment of the cycle.
2. Capturing video of a bead in the optical trap as fluid flow applies drag force to it. This is achieved by trapping the bead inside a water-filled chamber fixed to the stage and oscillating the stage identically to the oscillation in step 1. Trap power is scaled down uniformly by adjusting a half wave plate in the beam path upstream of a polarizing beam splitter to divert an arbitrary amount of laser power from the branch in the beam path which leads to the optical trap.

3. Performing particle tracking to get bead position versus time within a generic cycle of stage displacement, then smoothing the data and fitting the smoothed data to a sin series with phase information.
4. Calculate drag force according to Stokes' law
5. Plot drag force versus bead offset, with offset being bead position minus the value of bead position at zero fluid velocity. This is the trap force landscape along one direction. Landscapes can be defined along other directions by modifying the direction of stage displacement used.

The entire protocol is as follows:

Supplies

- Precision #1.5 cover slips
- Microscope slide
- Double-sided mounting tape. Gorilla Glue™ clear mounting tape is recommended.
- Triple-distilled water (TDW)
- Fluosphere solution (Life Technologies Corporation, Carlsbad) diluted ~10,000:1 in TDW

Procedure

1. Map stage displacement and velocity
    a. Place small drops of diluted fluosphere solution onto a cover slip, let them dry out, and place the cover slip on the stage.
    b. Command sinusoidal stage displacement of the same amplitude and direction(s) that will be used to generate fluid velocity over a trapped bead in water. Capture video of the bead displacement with the shortest possible exposure time to minimize blurring.
    c. Perform particle tracking on the video, plot the resulting position versus cyclic time (time modulo the period of sinusoidal stage displacement), and fit a sin series with phase

information to the resulting data. This defines stage position versus cyclic time, and the derivative of the sin series defines stage velocity versus cyclic time.

2. Use a bead trapped in water to correlate drag force with bead position.
    a. Set the trap laser to the power which will be used in microrheology data collection and turn on the lamp used to excite fluorescence in the beads.
    b. Apply a single piece of mounting tape to the microscope, as close to the dimensions of the cover slip as possible. If the mounting tape is less than 1 mm thick, it may be a good idea to apply two thicknesses of tape.
    c. Cut a rectangle in the center of the mounting tape (approximately 10x20 mm) and peel the inner tape away from the slide, leaving a "well" of tape on top of the slide.
    d. Slightly overfill the well with diluted Fluosphere solution and place the coverslip down over the well to create a sealed chamber. Make sure to lower the cove slip evenly so the excess water escapes out the sides without leaving air bubbles in the chamber.
    e. Place the sealed chamber on the stage, cover slip side towards the objective lens.
    f. Capture a floating bead in the trap.
    g. Command sinusoidal stage displacement of the same amplitude used to map trap position and velocity. While using live video view in μManager, rotate the half wave plate upstream of the polarizing beam splitter in the trap beam path until the amplitude of bead displacement is sufficient to cover that range of bead-trap offsets expected in experimental data.[25]
    h. Capture video of the bead oscillation during sinusoidal stage displacement, using the shortest possible exposure time to minimize blurring.
    i. Measure beam power in the telescope section of the beam path with the half-wave plate at the same angle of rotation used to enable large displacements of the trapped bead. Measure

the power again with the half-wave plate rotated to allow maximum power along the branch of the beam path which forms the trap.

j. Perform particle tracking on the video, plot the resulting position versus cyclic time (time modulo the period of sinusoidal stage displacement), and duplicate the data with one period of stage displacement added, creating two cycles of identical bead displacement data.

k. Smooth the two cycles of data in MATLAB using the smooth function with span specified and method set to *rloess*, which is a local regression smoothing method which progressively decreases the weighting used for outliers, reaching zero weight at six mean absolute deviations. Span width should be set to the minimum value possible without generating obvious noise. The smoothing operation has non-ideal performance at the ends of the data set, which is why a second identical cycle is used. With the second cycle, a full cycle of data can be extracted without approaching either end of the data set.

l. Fit a sin series with phase information to the smoothed data starting half a cycle into the data and ending half a cycle before the end of the second cycle. This defines stage position versus cyclic time, and the derivative of the sin series defines bead velocity versus cyclic time.

m. Calculate drag force on the bead according to Stokes' law, with fluid velocity defined by stage velocity minus bead velocity. Multiply this force by the ratio of maximum beam power to reduced beam power found in step i so that the force curve will represent the force at maximum power, rather than at the effectively reduced power used to enable large bead displacement.

n. Identify the time point in the cycle at which fluid velocity crosses zero. Subtract the corresponding bead position at that time point from all bead position values because this is the resting bead position (position at zero drag force).

o. Plot negative drag force versus bead position. This is trap force versus bead-trap offset. Alternately, plotting negative drag force versus negative bead position will yield trap force versus trap-bead offset.

Measurement of trap force as a spring constant

For comparison to trap force mapping, trap force was also measured using the state of the art as a spring constant, i.e. linear versus trap-bead offset, using a simple variant of trap force versus bead position calculation. Specifically, the spring constant was obtained by calculating the amplitude of cosinusoidal displacement at 2 Hz of a trapped bead resulting from 2 Hz sinusoidal stage displacement. Stage displacement was calculated as the 2 Hz Fourier peak obtained from the position versus time of a bead fixed to the stage. Displacement amplitude of the bead in the optical trap was similarly calculated through Fourier analysis. The spring constant was then given by Equation 5.2, where F_{drag} is the drag force given by Equation 5.1 and A_{bead} is the 2 Hz Fourier peak for trapped bead displacement.

$$k_{trap} = \frac{-F_{drag}}{A_{bead}} \tag{5.2}$$

Theoretical trap force calculation

Theoretical trap force was calculated using the Optical Trap Toolbox developed by Nieminen *et al*.[21] The toolbox uses T-matrix theory, which includes wavelength effects. The model was set up to have a Gaussian beam with 1064 nm wavelength passing through a 1.2 NA lens into water, where it trapped a 2 µm diameter bead with index of refraction 1.55. The toolbox gives trapping efficiency per photon, and a conversion to trap force per Watt is given in the documentation. Because the laser power reaching the bead is difficult to calculate, arbitrary scaling was applied between the theoretical and experimental trap force landscape for a qualitative, rather than quantitative, comparison.

Results and Discussion

The trap force landscape was measured for 2 μm diameter Fluospheres (Life Technologies Corporation, Carlsbad). Results are shown for intermediate steps in the process of measuring trap force landscape, as well as for the final results. Stage position versus cyclic time along the X direction is shown in Figure 5.4, with a sin series fit to the displacement and overlaid onto the scatter plot with very good agreement. The derivative of the sin series was taken to obtain stage velocity at all times within a cycle, as shown in Figure 5.5. The position of a bead held in a stationary trap during stage displacement along X is shown in Figure 5.6. This position data was smoothed and fit to a sine series, with both the raw smoothed curve and the fitted sine series overlaid. Aside from beam power measurements, these measurements of position were fully sufficient to define the trap force landscape along X.

The final trap force landscape along both X and Y are in Figure 5.7. There are immediately practical applications for such maps. The linearity observed in a trap with good alignment would allow for confident use of a spring constant model at larger than offsets than the 100-200 nm typically used in microrheological experiments.[30] Alternately, trap force landscapes could allow microrheological experiments to use offsets over the entire map, as force could be looked up using the map. This would be useful for low quality or custom traps which do not have large, linear regions. Extending this idea, trap force landscapes can enable diagnosis of flaws in trap shape. Figure 5.8 shows a trap force landscape paired with a spring force constant calculated using the same bead within a few minutes of collecting data for the landscape. The spring constant agrees well with the trap force landscape at offsets up to 100 nm, but quickly loses accuracy at larger offsets to finally underestimate applied force by 38% at an offset of 350 nm. The beam path was re-examined and found to have poor alignment, the fixing of which led to the relatively linear trap force landscapes in Figure 5.7. The ability of trap force landscapes to show the range of offsets with acceptable error for a spring constant model, to precisely specify the

instantaneous force at any offset in more precise calculations of force, and to diagnose issues with a trap make them a powerful tool for experimental work.

Turning to theory, it is noteworthy that the landscapes along both axes are very nearly linear for spans of offsets exceeding ±400 nm. This agrees well with theoretical calculations made using T-matrix theory over the same span of offsets.[21] The experimental trap force landscapes are shown in Figure 5.9 with arbitrary scaling to match the approximate features of theoretical landscapes over the same span of offsets. The theoretical curves are similarly linear over a matching offset span. However, as shown in Figure 5.10, the theoretical curves show increasing trap force well beyond what could be measured experimentally, finally peaking at offsets over 1000 nm. Attempts to increase bead offset beyond the offsets shown in the maps resulted in the beads escaping the trap. Precursors of this danger are visible in Figure 5.6 as rapidly increasing scatter in bead position at either end of peak displacement. It is not clear whether trap force continues to increase beyond this point and is simply overcome by currents within the fluid chamber, or whether some effect is missing in the theoretical calculations which causes trap force to peak at much lower offsets than predicted. Trap force landscapes at least provide an efficient tool for examination of theory, with the possibility of extending both theory and the methodology behind trap force landscape generation.

Figure 5.4: Scatter plot of bead position when affixed to stage during commanded sinusoidal displacement of the stage. A sin series fit with phase information and harmonics up to the 5th is overlaid.

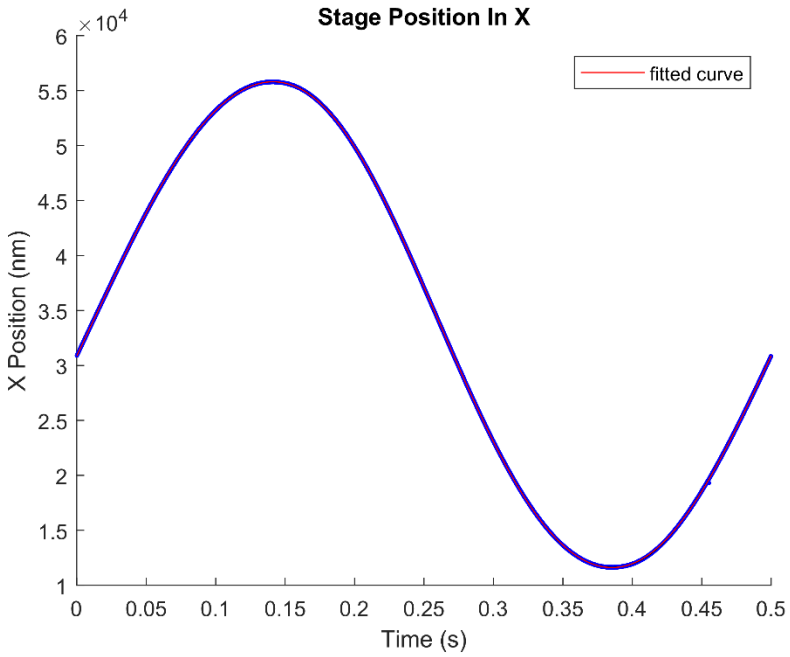

Figure 5.5: Stage velocity, as determined using the fitted sin series in Figure 5.4.

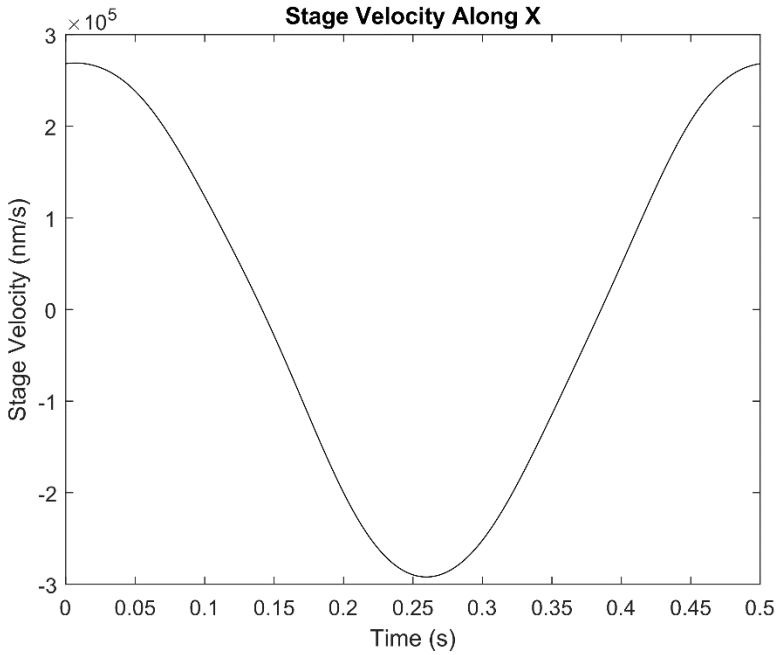

Figure 5.6: Measured position of bead over many cycles when held by a stationary optical trap in water during stage displacement. The raw curve obtained from smoothing the data is shown in white, and the sin series fit to that curve is shown in red.

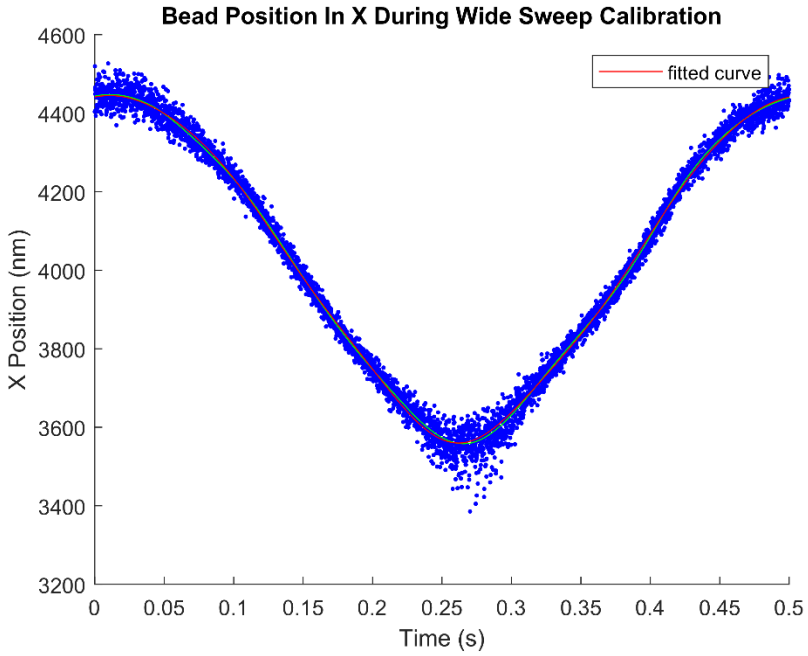

Figure 5.7: Trap force landscape along both X and Y directions with good beam alignment.

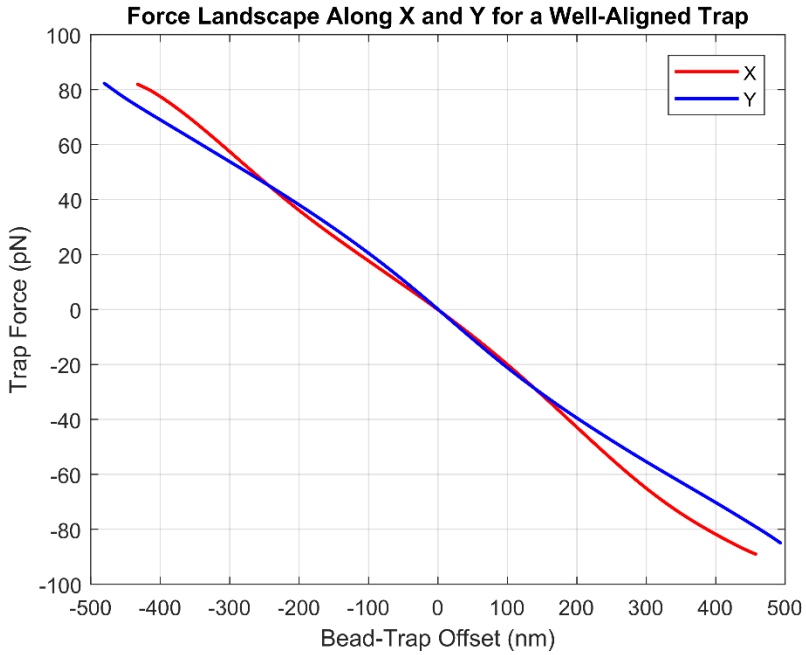

Figure 5.8: Trap force landscape along X and Y with non-ideal beam alignment, plus force vs offset calculated using the spring constant method. The two methods agree within 10% for displacements up to 100 nm,

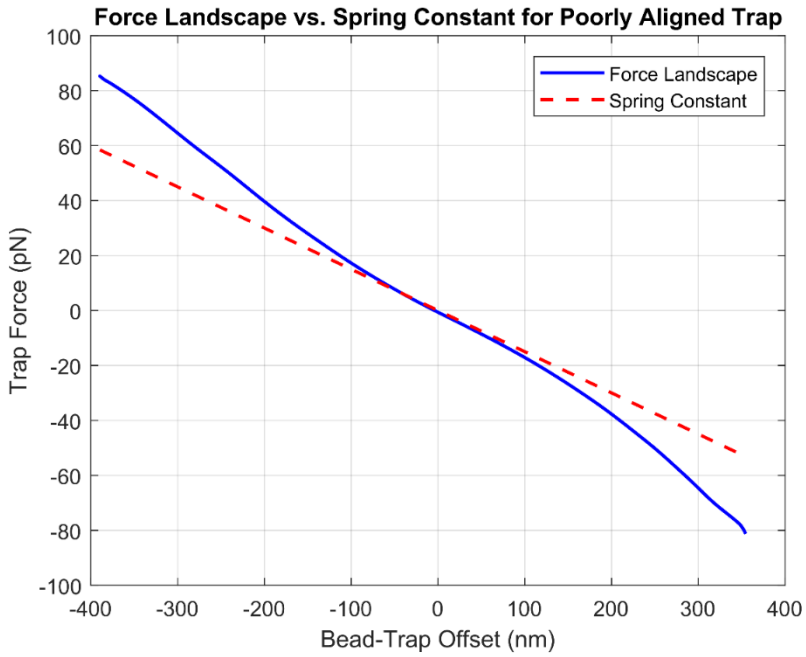

Figure 5.9: Experimental and theoretical trap force landscape over the approximate range of bead-trap offsets which could be measured experimentally.

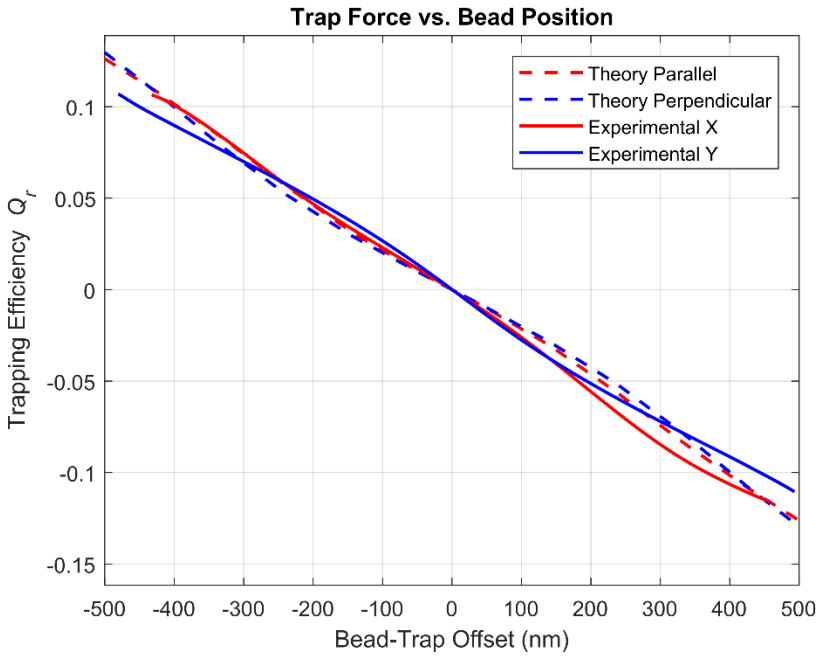

Figure 5.10: Experimental and theoretical trap force landscape over a range of offsets covering all non-negligible force amplitudes in theoretical calculations. Theory shows the trap stiffness increasing beyond the maximum offset which could be obtained experimentally, finally peaking at offsets of just over 1000 nm.

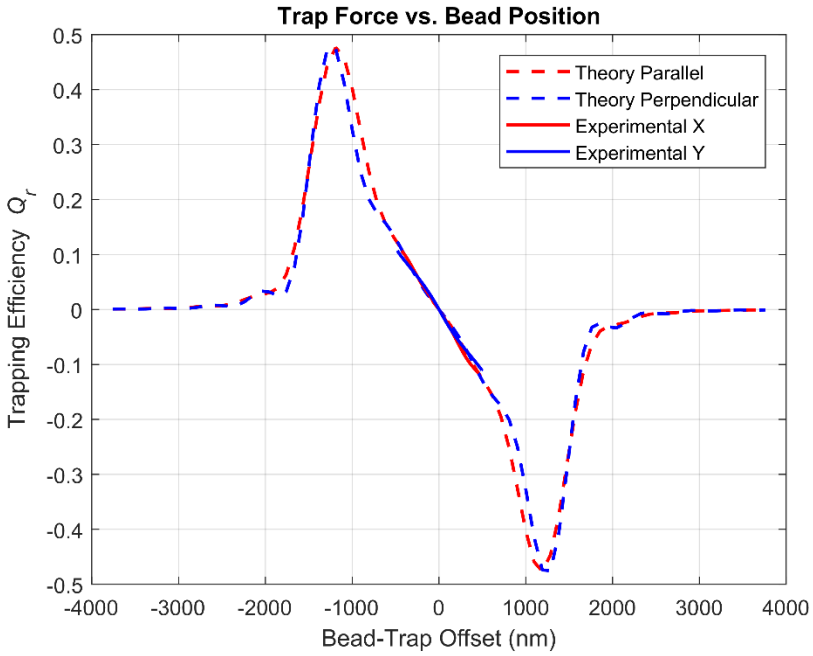

The method developed for generation of trap force landscapes proved to be powerful, both experimentally and as a test of theoretical calculations. Major outcomes are shown in Table 5.2. Experimentally, landscapes can enable confident use of larger offsets, and hence larger forces, than typically used in microrheology through agreement with a spring constant model or to look up precise, instantaneous force. This has implications for multi-particle microrheology, in which receiver bead displacement is inversely proportional to distance and material stiffness, requiring either larger forces or more precise measurement of bead displacement to extend the method. Regarding theory, trap force landscapes were found to corroborate theoretical calculations, but only over a range of bead-trap offsets just under half the span that might be expected from the theoretical calculations. The marginal effort involved in generating a trap force landscape is

comparable to the former state of the art while providing greatly increased power, making them a clear improvement which should be used whenever possible.

Table 5.2: Major outcomes in trap force landscape mapping.

Finding	Description	Impact
Maps cover large bead-trap offsets	Trap force could be mapped for bead trap offsets up to approximately 0.5 µm for 2 µm diameter beads and 0.2 µm for 1 µm diameter beads.	The magnitude of offsets mapped provide knowledge of trap forces well beyond the span commonly used in optical trap experiments, providing the possibility of large trap displacements to generate large bead displacements.
Nonlinearity in trap force	Trap force maps showed anisotropic nonlinearity dependent on beam alignment, with variation in a secant spring constant ranging from approximately 10% for good beam alignment almost 40% for poor alignment.	Trap force maps provide quantitative information about trap shape, allowing for use of a trap at any offset within the map and also diagnosis of problems with the trap.
Agreement with theory in span of offsets measured	Trap force maps qualitatively agreed with calculations made using T-matrix theory, with the major exception that theory predicted trap force increasing well beyond the point at which the bead escaped the trap experimentally.	Trap force landscapes provide a more powerful tool for comparison to theory than the previous state of the art method, but the reason for a limited span of offsets in experimental trap force landscapes is not clear.

Chapter 6 : Data Collection Procedure

Advances in the actual process of data collection were necessary to provide certain abilities of the 2P method. Apparatus calibrations (Chapter 3) and trap force landscape measurements (Chapter 5) are examples of this, but were not required to be repeated for every sample, much less every constellation of beads examined. In data collection performed directly on gels, three main advances were made: sinusoidal trap displacement, large amplitudes of those displacements, and “star driving”. Sinusoidal trap displacement results in approximately sinusoidal bead displacements well-suited for Fourier analysis, while large amplitudes of those displacements increase the displacement signal at the driving frequency over the background noise for more precise measurements. Star driving, illustrated in Figure 6.1, is a process of applying sinusoidal driving to the driven bead at successive spatial angles, provides a spectrum of (X,Y) force vectors. The resulting (X,Y) displacement vectors for each bead can then be related to the applied force vectors to probe material properties. These advances are straightforward to apply and greatly enhance the ability of the 2P method to characterize materials.

Figure 6.1: Schematic of a bead pair in the 2P method with star driving and elliptical receiver displacement.

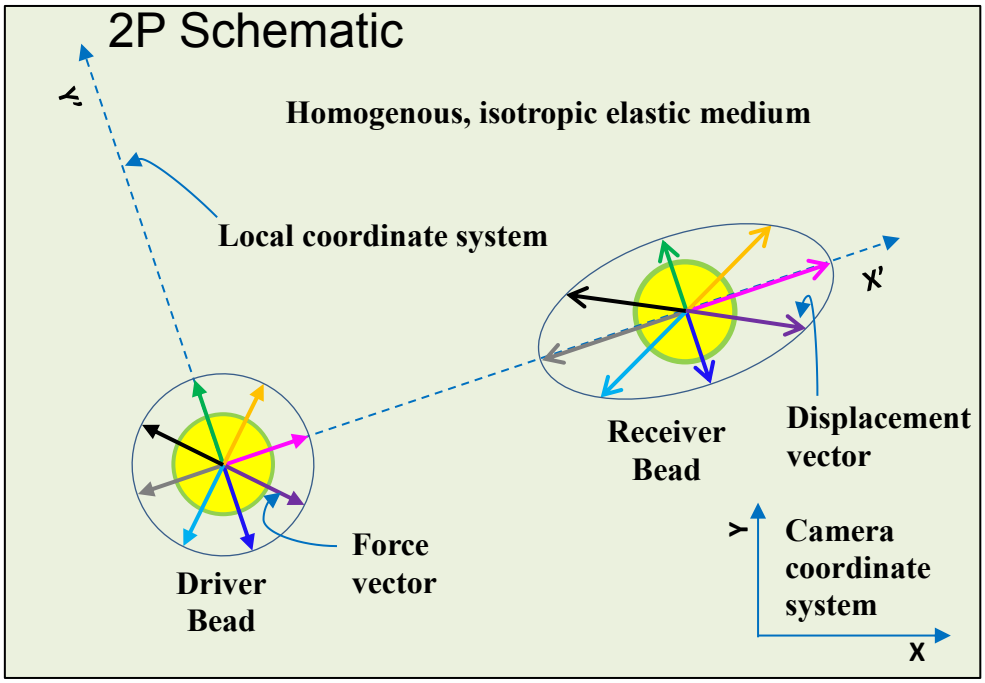

Table 6.1: Innovations in data collection procedure.

Innovation	Description	Impact
Sinusoidal trap displacement	A single bead was driven by sinusoidal displacement of the optical trap	Sinusoidal signals are the simplest to quantify with Fourier analysis and enable quantification of nonlinearity through use of harmonics and phase lag.
Large optical trap displacements	The use of large optical trap displacements to generate large bead displacements.	Larger bead displacements at a given laser power increase the signal-to-noise ratio.
Star driving	Star driving is the process of incrementing the angle of force applied to a driven bead.	Observing X and Y bead displacement with varied ratios of X and Y force enables quantification of a 2D relationship between force and bead displacement.

The actual process of taking data, the protocol for which is in the appendix, has several key steps. After a pre-prepared gel sample is placed on the microscope stage, the operator scans through it to find a constellation of beads all in focus within the field of view. The operator then chooses one of those beads to be the driven bead and moves the microscope stage so that the driven bead is centered on the trap (this is done roughly by manual stage adjustment, then with fine control using piezo-actuated stage displacement). With the driven bead centered on the trap, the operator initiates oscillation of the optical trap using a LabVIEW program, typically at an amplitude of 500 nm and an angle of 0°. This program records time traces of the signal sent to the galvanometric trap steering mirrors and the voltage of the CCD shutter signal, with time stamps for each data point. As the trap oscillates sinusoidally, the "spring force" connecting the bead to the trap will generate a similar force pattern on the driven bead, which will lead to a displacement field throughout the whole gel. Next, the operator begins image acquisition, usually for 1000 frames, through µManager.[25] After saving the data from each "trial", the operator re-centers the driven bead on the optical trap and begins another trial with a different angle of trap oscillation until all desired angles have been tested. The operator may then choose another driven bead within the same constellation or scan through the sample and find a new constellation. The relative positions of each constellation are not recorded. However, depth into the sample is generally recorded to avoid testing of a constellation near the cover slip, which could lead to deceptively small displacements if gels are bonded to the glass or deceptively large displacement if gels are unattached. The result of this data collection procedure is a set of videos associated with time-stamped logs of driving and shutter signals, from which bead displacement and applied force can then be calculated and assembled into a relationship between force and displacement for each driven bead and bead pair.

Chapter 7 : Analysis of Experimental Data

Introduction

As the multiparticle microrheology technique is enhanced with respect to calibration and data collection, improvements in data extraction and analysis must also be developed. In broad terms, analysis of microrheological data required the calculation of force and bead displacement amplitudes, the definition of relationships between force and bead displacement, and finally reframing of those relationships as quantities which provide specific insights into micromechanical behavior of the gel which was probed. This chapter describes substantial advances in data processing that allow 1P and 2P data to be extracted simultaneously for each bead constellation, facilitates the collection of the full Fourier spectra for the quantification of nonlinearity and estimation of precision, constructs force-displacement coupling matrices which specify the relationship between the driver and receiver bead, and provides a platform from which all properties can be reported versus bead separation to investigate length scale effects specific to each material (Table 7.1).

Table 7.1: innovations in analysis of experimental data.

Innovation	Description	Impact
Trap force mapping	A method was developed to quickly map optical trap force over a large span of bead-trap offsets.	Specifies the force applied at any trap-bead offset. Allows quantification of nonlinearity in trap shape and/or extraction of an effective spring constant.
Simultaneous 1P and 2P	The simultaneous analysis of 1P & 2P data from each data set.	Allows comparison of the two data types for each sample and sample type.
Generation of full Fourier spectra	Generation of full Fourier spectra with phase information for bead displacement along each axis.	Harmonics allow quantification of nonlinearity, which enabled detection of soft sheaths around beads. Non-harmonic frequencies allow quantification of displacement noise.
Force-displacement coupling matrices	Definition of a force-displacement coupling matrix for each driver-receiver bead pair.	These matrices fully define isotropic viscoelastic material properties, anisotropic orientation and magnitude for 1P data, and could be used to define anisotropic material orientation and properties.
Viscoelastic characterization	Viscoelasticity was quantified in 1P and 2P data through phase lag with respect to the trap force, including phase lag dependence on force-displacement coupling mode.	Complex modulus is the standard result of microrheology, but dependence of viscoelastic constants on whether the coupling mode is direct or transverse has not been studied before, to the author's knowledge.
Material properties versus bead separation	Examination of all measured properties versus bead separation.	Exposes length scales of heterogeneity through trends in the mean value or scatter of each value.

Measuring Position, Displacement, and Force

The first step in the data processing was the conversion of video data to bead position versus time using the refined particle tracking (Figure 7.1). First, beads were detected in the first frame and kernels (a region cut out of the first image frame and compared to subsequent images at different locations) are generated. Each kernel was projected onto each frame of the video in a predefined grid of different positions and compared for goodness-of-match at each position. The precise position of that bead in that frame was then reported as the

peak of a 2D Gaussian fit to the goodness-of-match versus position. The result was a list of the (X,Y) positions of each bead and an associated list of time stamps for the frames from which those positions were extracted.

Figure 7.1: Major conceptual steps in refined correlation particle tracking. First, a small kernel for each detected bead is cut out from the first frame after background brightness is subtracted. Next, that kernel is compared for goodness-of-match (correlation strength) to subsequent frames across a grid of relative position offsets. F

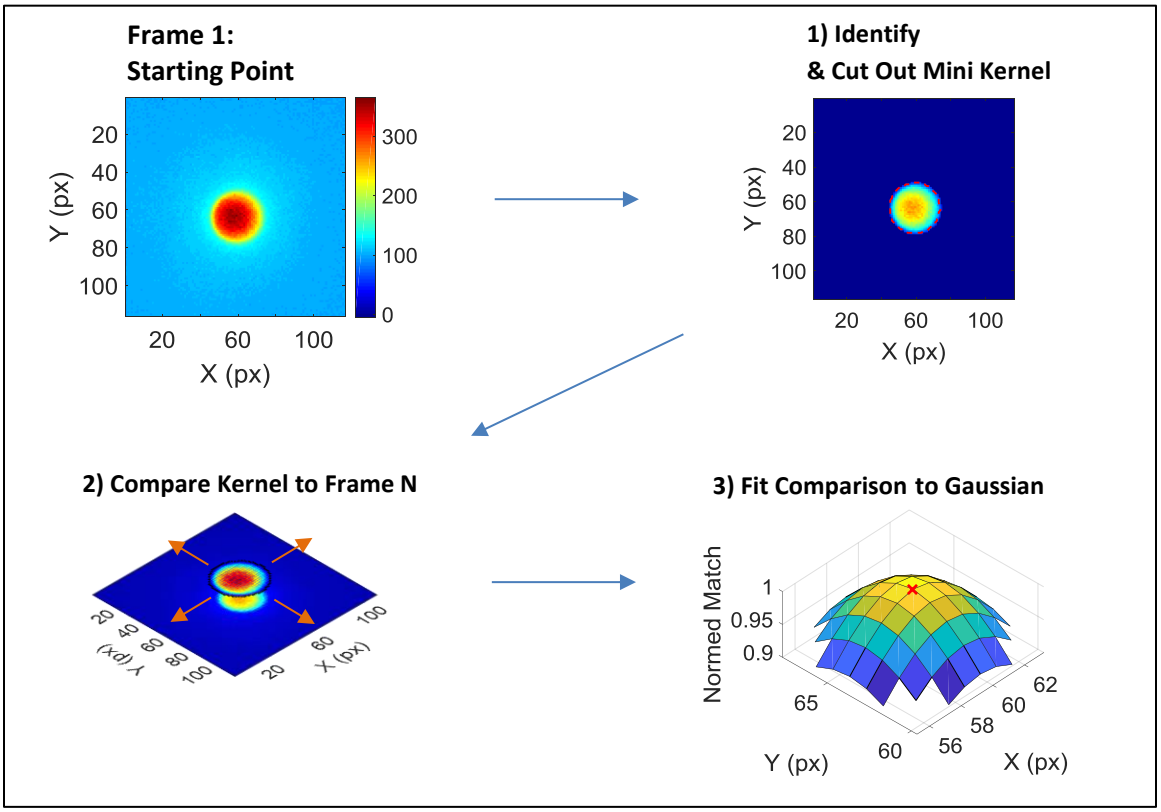

Position data was used to group trials involving the same bead constellation and to provide consistent labels to beads in those trials. The lack of an "absolute" coordinate system associated with video data, photo

bleaching of beads, changes in the position of beads with respect to the focal plane, and changes in the field of view captured between trials all complicate this recognition process. Recognition was initiated through comparison of relative bead positions from frame to frame. Each bead from the most recent constellation was paired with the same bead within the current constellation, and the relative position difference between the bead in the prior trial was subtracted from a copy of the position of the bead in the current constellation. This process is repeated for all the beads in a constellation. If this resulted in a sufficient fraction of beads in the current constellation having positions within a fraction of a bead radius of bead positions in the recently observed constellation, the two were considered a match and any newly observed beads were recorded as being part of the constellation. Master lists were made labeling all beads observed in a data set, which trials they were observed in, and their indices within that trial. Consistent labeling not only of constellations between trials, but of individual beads, enabled efficient identification of all available data for each bead pair.

After bead position and time values were extracted from videos, Fourier spectra of bead displacement amplitudes were generated for each bead along each axis. Frequencies were generated in increments of the sampling period inverse up to the Nyquist frequency, with the precise active driving frequency and any applicable harmonics added into each spectrum if they were not already included. Because the sampling frequency was not tied to the driving frequency and sometimes varied by more than a factor of two over the duration of a video, refined explicit Fourier analysis (RefFA) was used to generate “in-phase” and “out-of-phase” spectra with accurate and precise amplitudes at the frequencies of interest. Representative spectra generated using RefFA, described in Chapter 4, are shown in Figure 7.2. Amplitudes of displacement with phase angle at the driven and harmonic frequencies, were extracted, as were estimates of uncertainty in those amplitudes. The uncertainty values were obtained through analysis of amplitudes other than the driven or harmonic frequencies. The result of this step was a set of values for each bead in each trial, describing the direction and phase angle of displacement at the driving frequency and harmonic frequencies with attached uncertainty values.

Figure 7.2: (a) A representative Fourier spectrum for a driven bead with a 2 Hz displacement amplitude of ~65 nm, and smaller amplitude components of displacement at 4 and 6 Hz. Other frequencies have non-zero measured amplitudes due to thermally-induced bead displacements, optical noise affecting the camera, and imperfect image analysis. (b) A representative Fourier spectrum for a receiver bead with a 2 Hz displacement amplitude of ~5.3 nm. Non-zero amplitudes measured at other frequencies are from the same origins as those for the driven bead. The sharp rise of the noise floor towards 0 Hz limits the precision of lower frequency measurements.

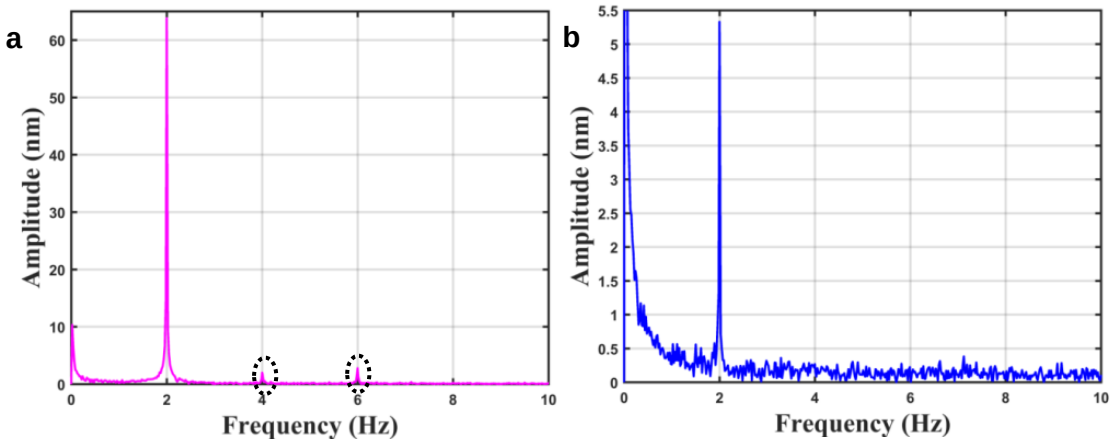

After bead displacements had been defined, the force vector applied to the driven bead was calculated for each trial using the difference between trap displacement and bead displacement. Effective spring constants along each axis were defined for entire data sets based on a map of trap force (Chapter 5), the amplitude of trap displacement, and typical amplitudes of bead displacement. A force vector was then calculated for each trial. Calculation of force at each time point could have provided more accuracy in the 2 Hz sinusoidal component of force, phase angle information, and amplitude of force at harmonic frequencies, but technical challenges and sensitivity studies suggested that an effective spring constant was sufficient for an optical trap with good alignment. The result of this step was a vector specifying the force applied to the driven bead in each trial.

Extraction of 2P Data

Force-displacement coupling matrices for 2P data were defined using a combination of data from each of the previous steps: mean position data for each bead, consistent bead labeling between trials, and force on driven beads. First, all trials with the same driven bead were identified. Next, a list was made of every bead identified in any of those trial. For each receiver bead, a coordinate system was defined with the origin at the center of the driven bead and the positive X' axis passing through the center of the receiver bead, as shown in Figure 7.3. In this coordinate system, four linear fits of receiver displacement versus driver force were performed, with r-squared (goodness of fit) values reported for each fit. The first two were for displacement in phase with the applied force. The first of the in phase fits was displacement along one direction at a time versus force along both X' and Y' to generate a coupling matrix with the form of Equation 7.1. A representative fit is shown in Figure 7.4. The second of the in phase fits was displacement along one direction at a time versus force along the same direction, generating a coupling matrix with the form of Equation 7.2. The two out-of-phase fits had the same form as the in-phase fits. These fits provided a full description of the force-displacement relationship for each bead pair, with the exception of nonlinearity in the response.

$$\begin{bmatrix} \boldsymbol{u}_{X'} \\ \boldsymbol{u}_{Y'} \end{bmatrix} = \begin{bmatrix} \boldsymbol{T}_{X'X'} & \boldsymbol{T}_{X'Y'} \\ \boldsymbol{T}_{Y'X'} & \boldsymbol{T}_{Y'Y'} \end{bmatrix} \begin{bmatrix} \boldsymbol{F}_{X'} \\ \boldsymbol{F}_{Y'} \end{bmatrix} \tag{7.1}$$

$$\begin{bmatrix} \boldsymbol{u}_{X'} \\ \boldsymbol{u}_{Y'} \end{bmatrix} = \begin{bmatrix} \boldsymbol{T}_{X'X'} & \boldsymbol{0} \\ \boldsymbol{0} & \boldsymbol{T}_{Y'Y'} \end{bmatrix} \begin{bmatrix} \boldsymbol{F}_{X'} \\ \boldsymbol{F}_{Y'} \end{bmatrix} \tag{7.2}$$

Figure 7.3: Schematic representation of a driven and receiver bead in an ideally isotropic, elastic medium. A local coordinate system is defined with the origin at the center of the driven bead, and the positive X axis passes through the center of the receiver bead. A series of equal magnitude force vectors are applied to the driven bead at increments of 45°. The collection of force vectors is circumscribed by a perfect circle. The response of the receiver bead is a series of displacements circumscribed by an ellipse aligned along the local coordinate system. The scaling of the major and minor ellipse axes are defined by the elastic constants of the medium.

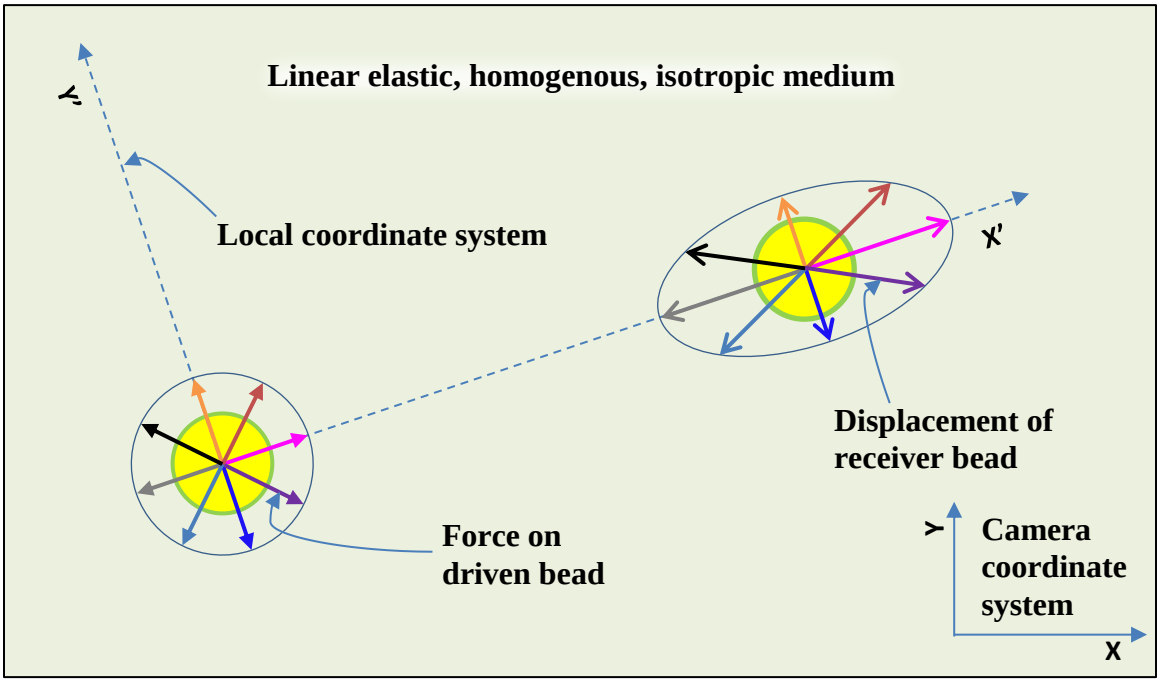

Figure 7.4: Experimental data used to generate element T_{YY} of a force-displacement coupling matrix for a receiver bead. The resulting linear fit is overlaid in red.

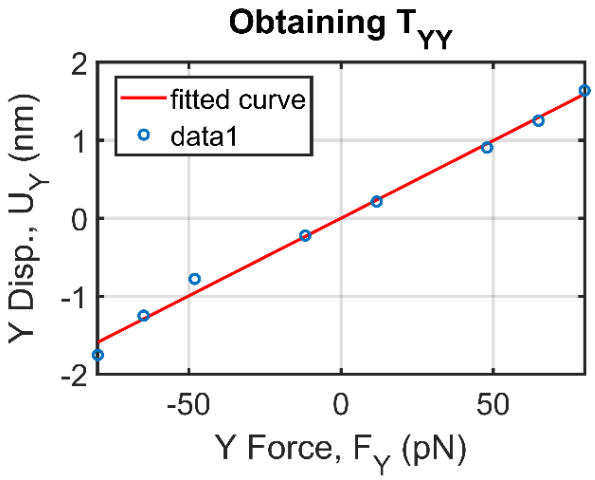

Material property values were defined using the 2D linear force-displacement coupling matrices, with error bounds of each value being provided by using propagation of uncertainty from 95% confidence intervals for the elements of the coupling matrices. Elastic Poisson's ratio was defined according to Equation 7.3 for in-phase displacement, and viscous Poisson's ratio was defined using the same terms for out-of-phase displacement. Equation 7.4 defined elastic shear modulus. Phase lag of bead displacement with respect to the trap was defined by Equation 7.5, and is illustrated in Figure 7.5. This allowed shear modulus to be defined in the traditional viscoelastic framework of *G'*, shear storage modulus, and *G''*, shear loss modulus using Equations 7.6 and 7.7, respectively. Anisotropy, only detectable for a single bead pair as coupling between force and displacement along different axes, was defined according to Equation 7.8. In total, seven material properties were measured using force-displacement coupling matrices, each value of which was assigned to a specific bead pair to allow plotting of the values versus bead separation.

$$\nu_{2P} = \left(\frac{a^2}{3r^2} + 3 - \left(1 - \frac{a^2}{r^2}\right) / \left(\frac{T_{X'X'}}{T_{Y'Y'}} - 1\right)\right) / 4 \tag{7.3}$$

$$G = \left(1 - \nu - \frac{a^2}{6r^2}\right) / (4\pi(1-\nu) T_{X'X'} r) \tag{7.4}$$

$$\phi = \tan^{-1}\left(\frac{u_{out\ of\ phase}}{u_{in\ phase}}\right) \tag{7.5}$$

$$G' = G(\cos(\phi))^2 \tag{7.6}$$

$$G'' = G\cos(\phi)\sin(\phi) \tag{7.7}$$

$$A_{2P} = \left(\left(\frac{T_{X'Y'}}{T_{X'Y'}}\right) + \left(\frac{T_{Y'X'}}{T_{Y'Y'}}\right)\right) / 2 \tag{7.8}$$

Figure 7.5: Illustration of phase lag, ϕ, between sinusoidal force and sinusoidal displacement.

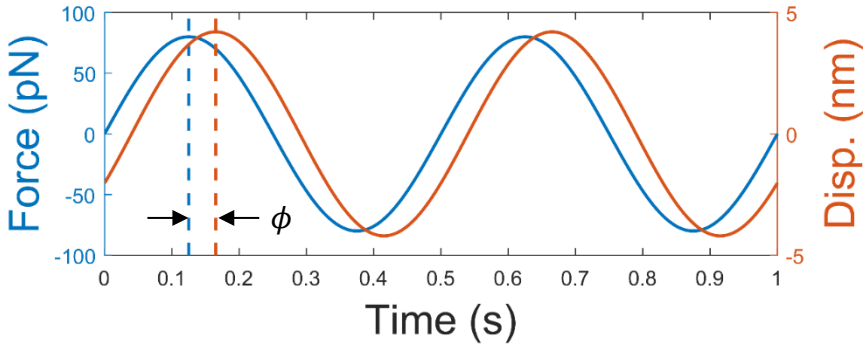

The final quantification performed for 2P data was harmonic amplitudes, defined as the ratio of displacement amplitude at a harmonic frequency to the displacement amplitude at the fundamental (driving) frequency. Second through fifth harmonic amplitudes were reported for bead displacement to quantify nonlinearity.

Extraction of 1P Data

1P data was processed similarly to 2P, with three major exceptions. The first exception was that force-displacement matrices were generated in the camera coordinate system because there was no inherent bead pair orientation. The second exception was that Poisson's ratio was assumed to be 0.5 rather than calculated because $T_{X'X'}$ and $T_{Y'Y'}$ were functionally interchangeable, making ν_{1P} undefined. Finally, anisotropy was quantified through eigenvector analysis as the ratio of displacements per force along the softest direction over the stiffest direction. 1P data processing was different than 2P data processing only to the extent that 1P data is fundamentally limited.

Conclusions

Data was processed from initial identification of bead position to quantification of a number of material properties with an emphasis on extracting as much data as possible. Trap force maps were paired with measured bead displacement to generate effective spring constants that are an improvement to the state of the art. Position data from multiple trials was assembled to group relevant trials together for generation of force-displacement coupling matrices. Full Fourier spectra with phase information were generated instead of just calculating amplitudes at the driving frequency to quantify nonlinearity and uncertainty. Confidence intervals were calculated for force-displacement coupling matrices so that error propagation could define uncertainty in reported material properties. Tracking which bead pair each value came from allowed those values to be reported versus bead separation. Each aspect added to data processing enabled new quantifications.

Chapter 8 : Probing Micromechanics versus Length Scale with 2P Microrheology

This chapter is adapted from the following manuscript:

Gutschick, D., Wallace, C., Yeung, D., Agarwal, G., Anderson, P.M., Powell, H.M. & Lafyatis, G. Probing Micromechanics versus Length Scale with 2P Microrheology. *In preparation.*

Abstract

The mechanics of a material will deviate from macroscopic values as the probe length scale approaches that of structural features in the material. This divergence of properties at small length scales can have major implications, such as for inter-cell communication in bio-matrices. Microrheology is well-situated to measure micromechanics in soft materials, but the state of the art has not been developed sufficiently to fully characterize micromechanics. This paper presents 2P microrheology, a novel method to measure the micromechanics of soft gels versus length scale using active, multi-particle microrheology. Results are shown with comparison between single-particle (1P) microrheology, 2P microrheology, and macroscopic testing.

Introduction

With decreasing length scale, the mechanical properties of a material will have increased scatter and can even diverge from the macroscopic values in a mean sense under certain circumstances. The length scale at which scatter and divergence become significant is related to the length scale of structural features in the material. These variations in mechanical properties can have major implications, such as cell-cell communication on fibrillar gels at distances greatly exceeding what is possible for those same cells on homogenous substrates.[2,3,5,39] Frequently, methods are known which can modulate structural features. In the case of synthetic polymer networks, such as polyacrylamide, cross-linking of the network can be modified simply by adding a cross-linking agent to a solution before initiating polymerization.[36,40] Despite the existence of tools to change structural features in gels and observations of cells responding to those changes, there are relatively few methods to probe micromechanics in the interior of a gel or other soft material.

Microrheology is a class of methods in which probe particles are dispersed inside a material and their displacement is correlated with some applied force to determine micromechanical properties.[24,41–46] The most common variants of microrheology are either passive microrheology, in which minute displacements of individual or paired particles are correlated with thermal forces << 1 pN, or active microrheology, in which larger displacements are generated by an operator-controlled source of force.[24] In both, some form of imaging or position sensitive detector is used to measure particle displacement. Passive microrheology requires on the order of one million time points to yield micromechanical properties because of the scale of displacements being measured. Active microrheology can use as few as two time points, and is generally divided into two sub-variants.[11] Active single particle (1P) microrheology, illustrated in Figure 8.1a, involves measuring the displacement of the particle to which force is being applied. Active single-particle microrheology has generated novel findings, such as a relationship between local collagen fibril density and local modulus spanning multiple orders of magnitude.[14] A major issue for the 1P method is that it has been known for almost 20 years that

particle-gel interface effects bias 1P modulus measurements in a manner that cannot easily be deconvoluted.[13,16,18,46,47] In the less common active multi-particle microrheology, force is applied to individual or sparse particles and the displacement of passive probe particles at a distance from the driven particle is measured.[11] This is illustrated in Figure 8.1b. Multi-particle microrheology has yielded information on the length scale of heterogeneity in colloidal gels and prototypical demonstrations of more advanced capabilities, such as determination of Poisson's ratio.[11,48] The promise of unbiased measurements and new information motivated the authors to advance multi-particle microrheometry.

The goal of this paper is to describe the 2P method, a paired particle microrheology method which provides material properties versus bead separation with high precision and without sensitivity to interface effects. Each driver-receiver bead pair quantifies nonlinearity, effective values of isotropic Poisson's ratio and shear modulus, anisotropy, and viscoelastic phase lag. Each property can be studied with respect to bead pair separation to probe length-scale and orientation dependence. The foundation for these abilities is the receiver bead displacement that arises from application of a periodic force on the driven bead. Many advances were necessary to achieve accurate, precise measurements of the relationship between force and displacement, and to turn that relationship into definitions of material properties. Key advances are laid out in Table 8.1, and representative absolute amplitude spectra of a driver and receiver are shown in Figure 8.1b-c, illustrating the large magnitude of the displacement signal at the driving frequency of 2 Hz relative to noise in each spectrum. With these advances, material properties are defined via the relationship between trap force and bead displacement amplitude, which is measured at the driving frequency with approximately 0.1 nm precision using 1000 time points.

Figure 8.1: a) 1P microrheology in which modulus is defined by F/δx for a single bead b) 2P laser tweezers define a wide range of material properties by measuring different modes of coupling between force on one bead and displacement of another at a distance r and angle θ. Elastic shear modulus, for example, is proportional to $F_r^D/\delta r^R$ for each bead pair. Displacements were extracted from Fourier spectra for c) driven and d) receiver beads at the driving frequency of 2 Hz, at the second and third harmonics of 4 and 6 Hz to probe nonlinearity, and at a range of frequencies near the driving frequency of 2 Hz to calculate noise in the signal.

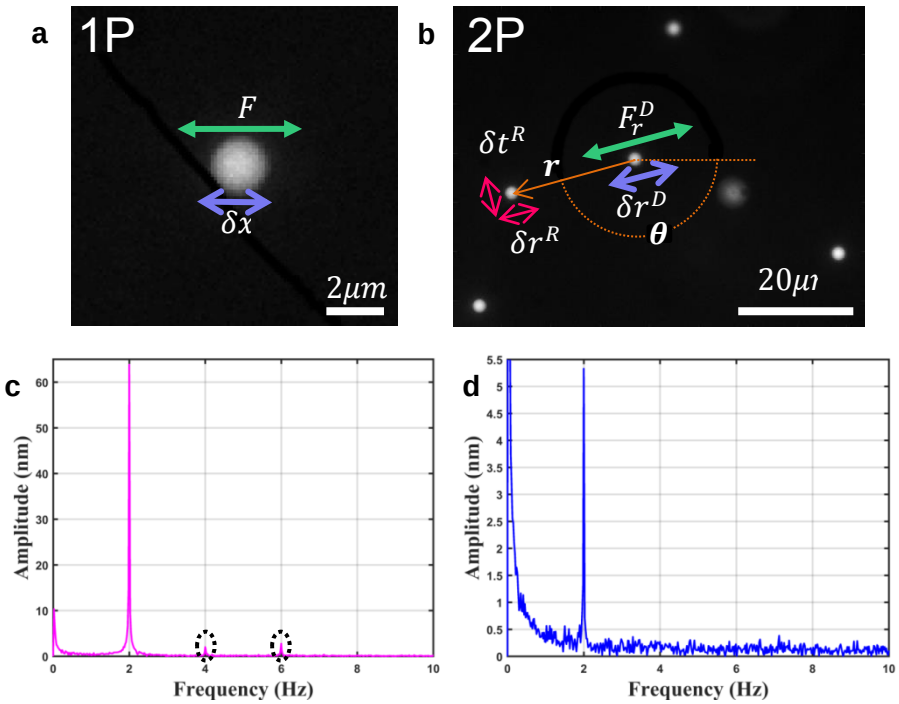

Figure 8.2: Schematic of a bead pair in the 2P method with star driving and elliptical receiver displacement. The size and shape of the ellipse define

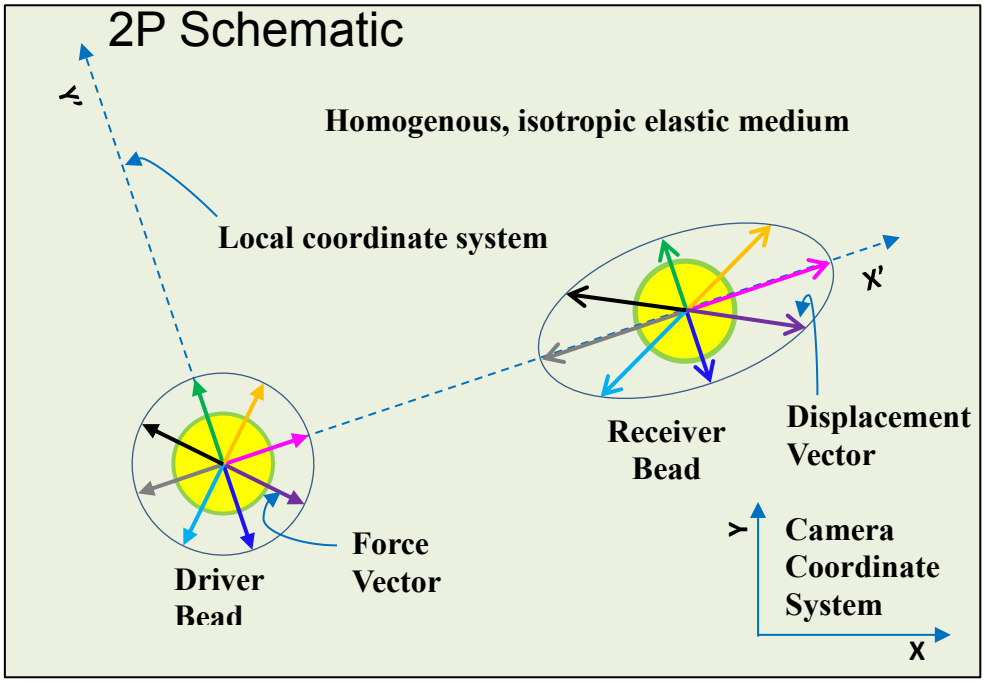

Table 8.1: Key innovations in probing micromechanics versus length scale with 2P microrheology.

Innovation	Description	Impact
Trap force mapping	A method was developed to quickly map optical trap force over a large span of bead-trap offsets.	Specifies the force applied at any trap-bead offset. Allows quantification of nonlinearity in trap shape and/or extraction of an effective spring constant.
Large optical trap displacements	The use of large optical trap displacements to generate large bead displacements.	Larger bead displacements at a given laser power increase the signal-to-noise ratio.
Simultaneous 1P and 2P	The simultaneous collection of 1P & 2P data.	Allows comparison of the two data types for each sample and sample type.
Star driving	Star driving is the process of incrementing the angle of force applied to a driven bead.	Observing X and Y bead displacement with varied ratios of X and Y force enables quantification of a 2D relationship between force and bead displacement.
Generation of full Fourier spectra	Generation of full Fourier spectra with phase information for bead displacement along each axis.	Harmonics allow quantification of nonlinearity, which enabled detection of soft sheaths around beads. Non-harmonic frequencies allow quantification of displacement noise.
Force-displacement coupling matrices	Definition of a force-displacement coupling matrix for each driver-receiver bead pair.	These matrices fully define isotropic viscoelastic material properties, anisotropic orientation and magnitude for 1P data, and could be used to define anisotropic material orientation and properties.
Viscoelastic characterization	Viscoelasticity was quantified in 1P and 2P data through phase lag with respect to the trap force, including phase lag dependence on force-displacement coupling mode.	Complex modulus is the standard result of microrheology, but dependence of viscoelastic constants on whether the coupling mode is direct or transverse has not been studied before, to the author's knowledge.
Material properties versus bead separation	Examination of all measured properties versus bead separation.	Exposes length scales of heterogeneity through trends in the mean value or scatter of each value.
Sheath models	Numerical models of a (visco)elastic medium containing a bead encased in a soft or stiff sheath.	These models allowed predictions of the properties of sheaths which are known to bias G in 1P data.

Results

Method Overview

The 2P method was used on three gel types: polyacrylamide (PAA), a synthetic polymer frequently regarded as a model material for its tunable modulus and homogeneity; collagen gel, a biopolymer matrix widely used in biomedical research and tissue engineering; and agarose, a biopolymer which forms heterogenous gels with large pores.[4,6,29,40,49–58] In PAA gels, three different concentrations of bis-acrylamide cross-linker were used to control the modulus of gels containing 3% acrylamide without changing network density. For collagen gels, the only variant shown was 2 mg/ml. For agarose, the only variant was 0.4% agarose in a buffer solution. 2P results were compared against 1P results for each gel type, and validated against macroscopic tests for one variant of PAA and for collagen.

The 2P method measures micro-mechanical parameters by relating the displacement of receiver beads to a known, oscillatory force on a driven bead (Figure 8.1b). Briefly, the method starts with a steerable optical trap, for which force versus bead-trap offset has been mapped over the relevant span of offsets. Raw micromechanical data is collected by centering the trap on a "driver" bead within a planar constellation of beads, then oscillating the trap sinusoidally at an arbitrary angle within the focal plane to generate force on the driver while a CCD camera records videos of the resulting bead displacements. Refined correlation bead tracking and Fourier analysis yield vector displacement amplitudes with phase information for each bead along each axis. A set of trials with different angles of force application allows statistical fitting of the 2D relationship between force on the driver and displacement of any individual bead. Finally, the relationship between driver force and "receiver" displacement is used to calculate material properties, which can then be mapped against driver-receiver separation.

Different modes of force-displacement coupling convey different information about micromechanical properties. The most direct representation of material properties is found in a coordinate system defined by each bead pair, with the origin at the center of the driven bead and the positive X axis passing through the center of the receiver bead as shown in Figure 8.2. In an isotropic, homogenous gel, force applied to the driven bead along *X'* will only produce receiver displacement along *X'*, and force along *Y'* will only produce receiver displacement along *Y'*. These are the "direct" and "shear" modes of force-displacement coupling. Equation 8.1 shows the equation coupling force to receiver displacement for a linear elastic, isotropic, homogenous gel, with displacement per unit force in direct coupling represented as $T_{X'X'}$ and the same quantity for shear coupling represented as $T_{Y'Y'}$. Poisson's ratio, ν_{2P}, is defined in Equation 8.2 by the same two coupling modes, the distance *r* between the bead centers, and bead radius, *a*. Elastic shear modulus, G, is defined in Equation 8.3. Poisson's ratio cannot be determined from 1P data because there is no differentiation between direct versus shear coupling, but shear modulus can be calculated from Equation 8.3 with an assumed value of Poisson's ratio and *r* set equal to *a*. If the gel is viscoelastic instead of purely elastic, there will be a component of displacement out of phase with force for each coupling mode as shown in Equation 8.4, which can then be used to define phase lag, ϕ, shear storage modulus, G', and shear loss modulus, G'', according to Equations 8.4-6. Finally, anisotropy will result in hybrid coupling modes, i.e. force along *X'* resulting in displacement along *Y'* or force in *Y'* resulting in displacement along *X'*. This will result in Equation 8.1 being replaced by Equation 8.7, from which the magnitude of observed anisotropy can be crudely defined according to Equation 8.8. This set of equations, using nothing but modes of 2D coupling between driver force and receiver displacement, are able to define Poisson's ratio, shear modulus, viscoelasticity, and a simple measure of anisotropy.

$$\begin{bmatrix} \boldsymbol{u_{X'}} \\ \boldsymbol{u_{Y'}} \end{bmatrix} = \begin{bmatrix} \boldsymbol{T_{X'X'}} & \boldsymbol{0} \\ \boldsymbol{0} & \boldsymbol{T_{Y'Y'}} \end{bmatrix} \begin{bmatrix} \boldsymbol{F_{X'}} \\ \boldsymbol{F_{Y'}} \end{bmatrix} \tag{8.1}$$

$$\boldsymbol{\nu_{2P}} = \left(\frac{\boldsymbol{a^2}}{\boldsymbol{3r^2}} + \boldsymbol{3} - \left(\boldsymbol{1} - \frac{\boldsymbol{a^2}}{\boldsymbol{r^2}} \right) / \left(\frac{\boldsymbol{T_{X'X'}}}{\boldsymbol{T_{Y'Y'}}} - \boldsymbol{1} \right) \right) / \boldsymbol{4} \tag{8.2}$$

$$G = \left(1 - \nu - \frac{a^2}{6r^2}\right) / (4\pi(1-\nu) T_{X'X'} r) \tag{8.3}$$

$$\phi = \tan^{-1}\left(\frac{u_{out\ of\ phase}}{u_{in\ phase}}\right) \tag{8.4}$$

$$G' = G(\cos(\phi))^2 \tag{8.5}$$

$$G'' = G\cos(\phi)\sin(\phi) \tag{8.6}$$

$$\begin{bmatrix} u_{X'} \\ u_{Y'} \end{bmatrix} = \begin{bmatrix} T_{X'X'} & T_{X'Y'} \\ T_{Y'X'} & T_{Y'Y'} \end{bmatrix} \begin{bmatrix} F_{X'} \\ F_{Y'} \end{bmatrix} \tag{8.7}$$

$$A_{2P} = \left(\left(\frac{T_{X'Y'}}{T_{X'Y'}}\right) + \left(\frac{T_{Y'X'}}{T_{Y'Y'}}\right)\right)/2 \tag{8.8}$$

Phase Lag, ϕ

Phase lag, ϕ, measured in the 1P and 2P method as an average across all trials, defines viscoelasticity. Although *G'* and *G''* are the quantities most commonly reported in microrheology studies, the authors found that trends in ϕ for both PAA and collagen gels have an impact on how shear modulus might be interpreted, and so should be presented first. Specifically, ϕ in a linearly viscoelastic gel will be the same at every location within the gel, as illustrated in the finite element results shown in Figure 8.3, while every PAA and collagen gel tested exhibited increasing phase lag versus bead separation. This violation of linear viscoelasticity means that G' and G'' are a function of some variable which changes with separation from the driven bead, and not just of frequency as is commonly assumed. In an effort to uncover the root cause of phase lag trends versus bead separation, phase lag was measured not only in 1P and 2P data, but also macroscopically for comparison in PAA and collagen gels.

ϕ *in PAA*

In the case of PAA, the rate of increase in ϕ versus r is modulated by cross-link density, with a more rapid increase in more highly cross-linked gels. Linear fits of ϕ versus r with 95% confidence bounds are given by Equations 8.9-11 for low, medium, and high levels of cross-linking, respectively. The best fit and 95% confidence

interval for each gel type has ϕ increasing with r. PAA was determined to not be linearly viscoelastic at any level of cross-linking tested, although it approached linear viscoelasticity with decreasing cross-linking. Macroscopic ϕ in the medium cross-linked gel was 5 ± 2° at 2 Hz and 0.1% peak strain, consistent with ϕ_{2P} at low bead separations but seemingly inconsistent with ϕ_{2P} at increasing bead separations.

$$\phi_{2P,lo\ PAA} = (0.12 \pm 0.06)r + (4.83 \pm 1.81) \tag{8.9}$$

$$\phi_{2P,med\ PAA} = (0.35 \pm 0.04)r + (0.33 \pm 0.92) \tag{8.10}$$

$$\phi_{2P,hi\ PAA} = (0.68 \pm 0.14)r + (8.40 \pm 3.85) \tag{8.11}$$

Figure 8.3: ϕ versus r in a sample of the least cross-linked PAA gel. Each color represents a different constellation of beads. Also shown are finite element model (FEM) results for a linearly viscoelastic material.

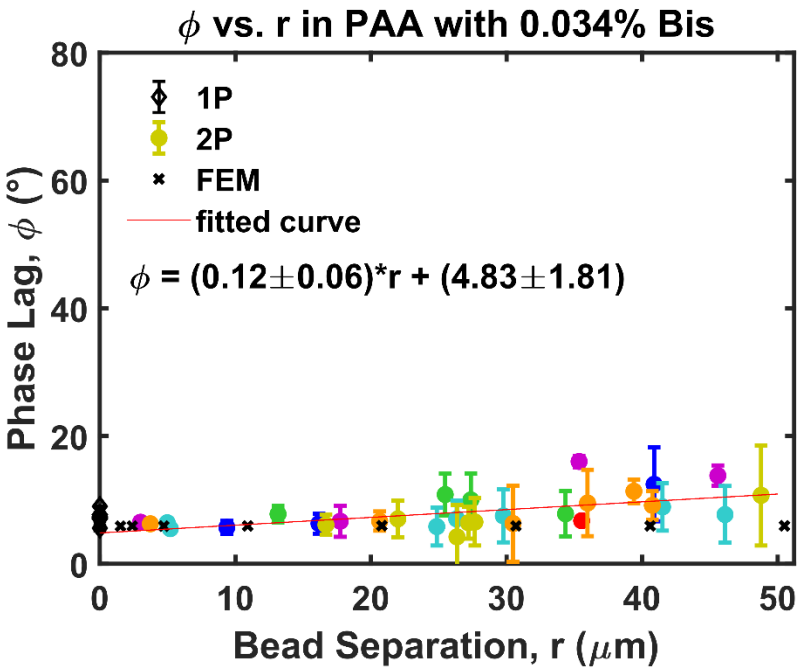

Figure 8.4: ϕ versus r in a sample of medium cross-linked PAA gel. Each color represents a different constellation of beads.

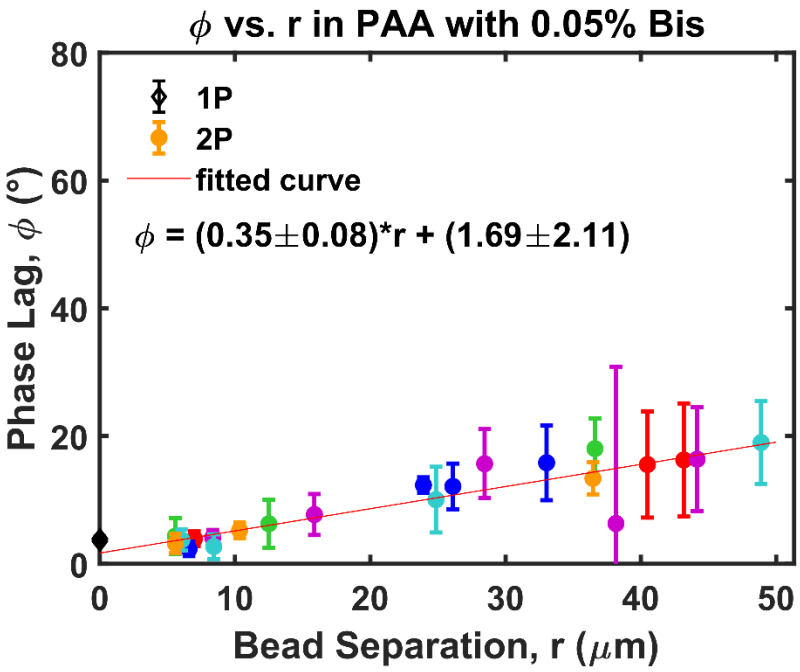

Figure 8.5: ϕ versus r in a sample of the most highly cross-linked PAA gel. Each color represents a different constellation of beads.

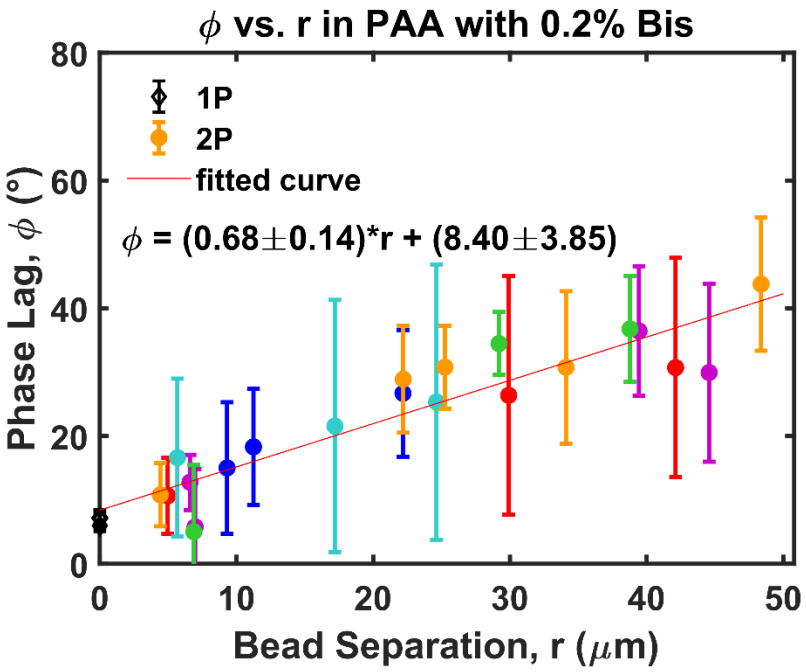

Because local strain and strain rate change with distance from the driven bead, it was hypothesized that a strain or strain rate amplitude effect was responsible for the observed trend in phase lag versus bead separation. To test this hypothesis, local peak shear strain versus bead separation was examined. Strain is the derivative of displacement, meaning that displacement versus bead separation could be fit to a function, and the derivative of that function would be local strain versus bead separation. The increase of ϕ with bead separation meant that in-phase and out-of-phase displacement could not both be falling off proportionally to 1/r as would happen in a linearly viscoelastic material, so both in-phase and out-of-phase displacement per unit force were fitted to Equation 8.12, with the results shown in Figure 8.4. The total strain from both in-phase and out-of-phase displacement was added together, allowing ϕ to be plotted against local peak strain along with macro ϕ versus strain in Figure 8.7. Both 2P and macroscopic data have increasing phase lag with decreasing

peak strain, but the increases occur at higher peak strain amplitudes in 2P data. In 2P data, it is notable that in-phase displacement falls off almost exactly as 1/r, but out-of-phase displacement falls off much more slowly, resulting in estimated peak strains of 3.5% at the driven bead surface, 0.1% at a bead separation of 6 μm, and 0.0013% at a bead separation of 55 μm for a force of 83 pN. The nearly ideal falloff of in-phase displacement shows an absence of length scale, strain, or strain rate effects in elastic displacement, while the slow falloff of out-of-phase displacement indicates that viscous displacement is responsible for ϕ increasing with bead separation.

$$\boldsymbol{T_{Y'Y'} = c/r^n} \tag{8.12}$$

Figure 8.6: Coupling strength versus bead separation, both for a) displacement in phase with applied force and b) displacement out of phase with applied force. Both types of coupling were fitted to Equation 8.12 and the best fit is shown in the plot.

a)

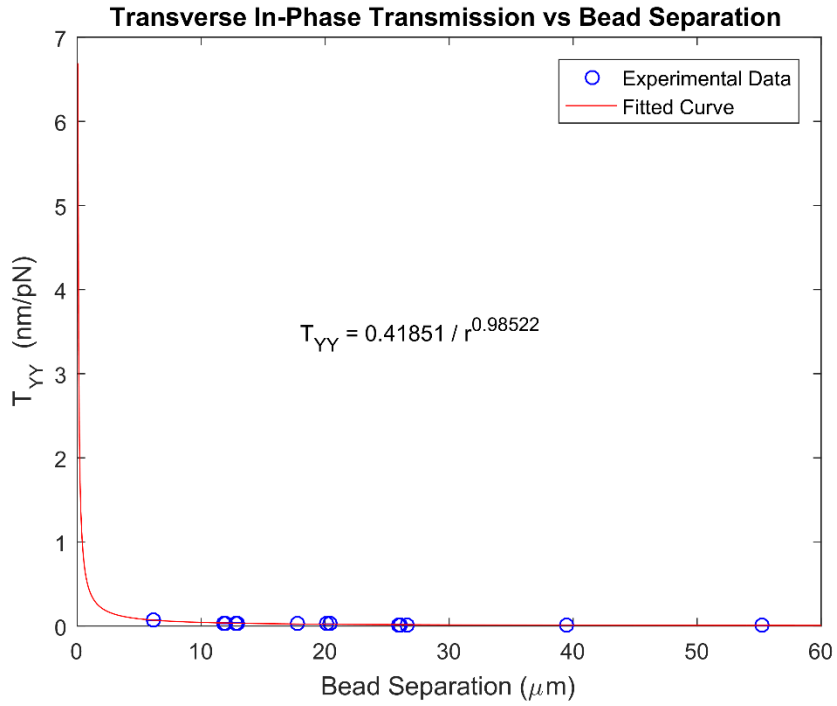

b)

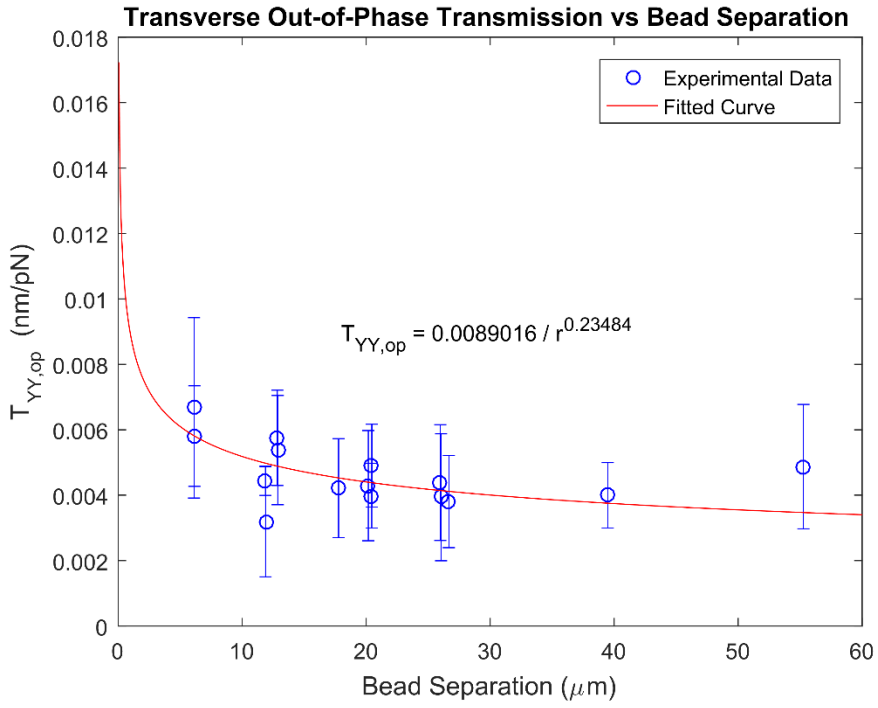

Figure 8.7: ϕ versus peak strain from 2P and macroscopic data. Both 2P and macroscopic data have increasing phase lag with decreasing peak strain as the lowest peak strains are approached, but the increases happen at different strain amplitudes. Two rheometers at The Ohio State University were used, the first in Dr. Vodovotz's lab, and the second in Dr. Swindle-Reilly's lab.

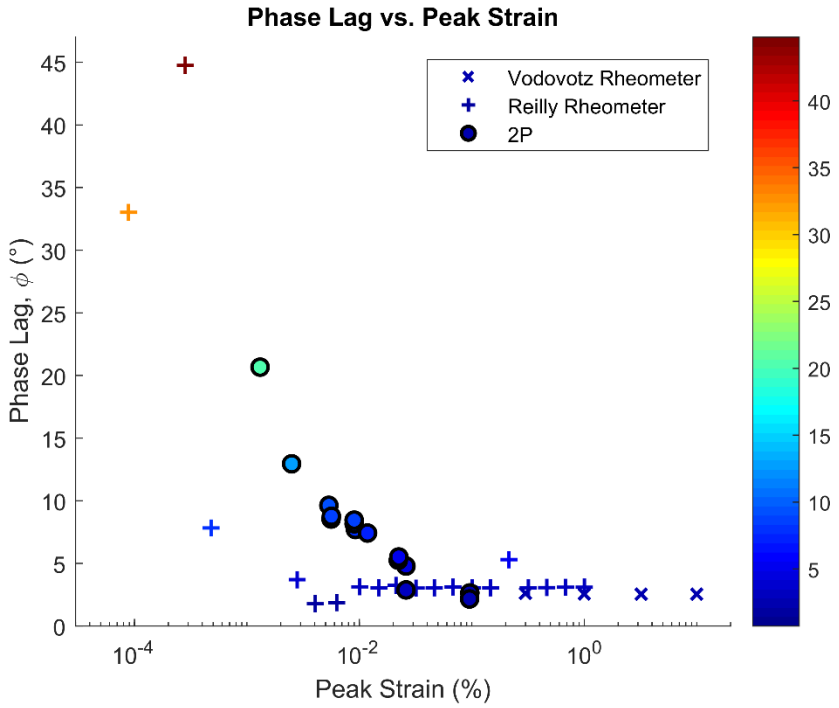

ϕ in Collagen

In the case of collagen, the rate of increase in ϕ versus r lay between the best fit of the lowest and medium cross-linked PAA gels. A linear fit of ϕ versus r with 95% confidence bounds for is given by Equation 8.13. The corresponding data is shown in Figure 8.8. As with PAA, collagen was determined not to be linearly viscoelastic because the 95% confidence interval of the slope in each sample was exclusively positive.

$$\boldsymbol{\phi_{2P,collagen} = (0.21 \pm 0.05)r + (5.03 \pm 1.22)} \tag{8.13}$$

Figure 8.8: ϕ versus r in a collagen gel with no NCPs. Each color represents a different constellation of beads.

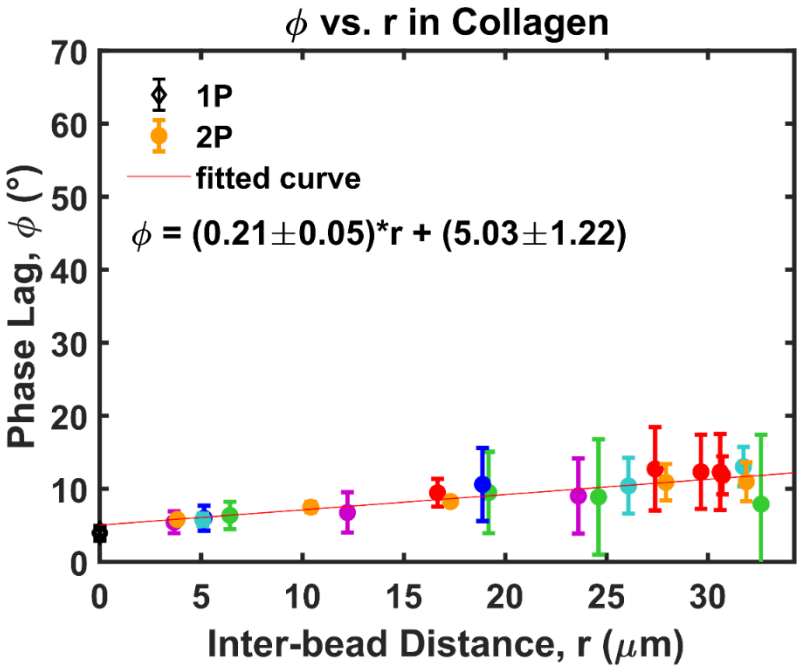

ϕ *in Agarose*

In the case of agarose, scatter in ϕ was greater than in any other sample type, masking any trend in ϕ versus r. A linear fit of ϕ_{2P} versus r with 95% confidence bounds is given by Equation 8.14. No determination could be made on the linearity or nonlinearity of viscoelasticity in agarose.

$$\boldsymbol{\phi_{2P,agarose} = (-0.25 \pm 0.72)r + (29.50 \pm 23.48)} \tag{8.14}$$

Figure 8.9: Phase lag, ϕ, versus bead separation, r, in agarose.

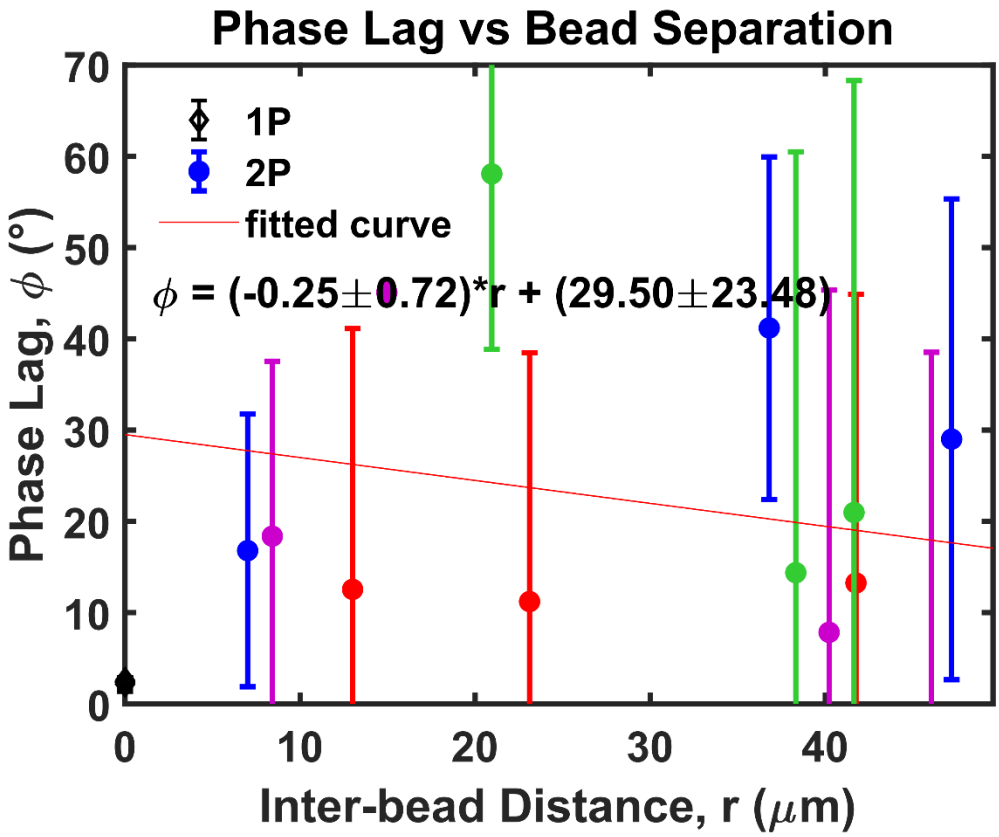

Poisson's Ratio, ν

Poisson's ratio, ν, defines the relationship between strain along different directions for uniaxial stress on a material, and is consequential in 2P data for at least two general reasons and one reason specific to the data at hand. First, it is a mechanical property which cannot be measured with the 1P method but is commonly measured macroscopically and can be obtained directly from differences in coupling mode strengths in 2P data even though this is uncommon.[11,47] Second, the equation that defines ν in 2P data is a function of $T_{X'X'}/T_{Y'Y'}$ and has a singularity when the ratio is unity, making small variations in the ratio of coupling mode strengths

manifest as large fluctuations in the apparent value of ν. Finally, a separation of Poisson's ratio into elastic ν and viscous ν has the potential to recommend or oppose mechanisms for nonlinear viscoelasticity observed in PAA and collagen gels. ν is presented with these features in mind for medium cross-linked PAA, collagen, and agarose.

ν in Med PAA

Elastic ν was measured in medium cross-linked PAA using the 2P method, as well as macroscopically via image analysis of tensile tests. No trend with bead separation was observed in 2P data, which had a mean value of 0.44 ± 0.08. This was statistically indistinguishable from the macroscopic value of 0.5 ± 0.02. As ν cannot be measured using the 1P method, the commonly assumed value of 0.5 is shown as a placeholder for the 1P method, corresponding to an incompressible material. Coincidentally, medium cross-linked PAA is an elastically incompressible or nearly incompressible material, according to the 2P method and macroscopic tests.

Figure 8.10: ν in medium cross-linked PAA. In 2P data, the mean value is 0.44±0.08, while the corresponding macro value is 0.50±0.02. A value of 0.5 is shown for 1P data because ν cannot be measured using the 1P method and it is common to assume a value of 0.5.[30]

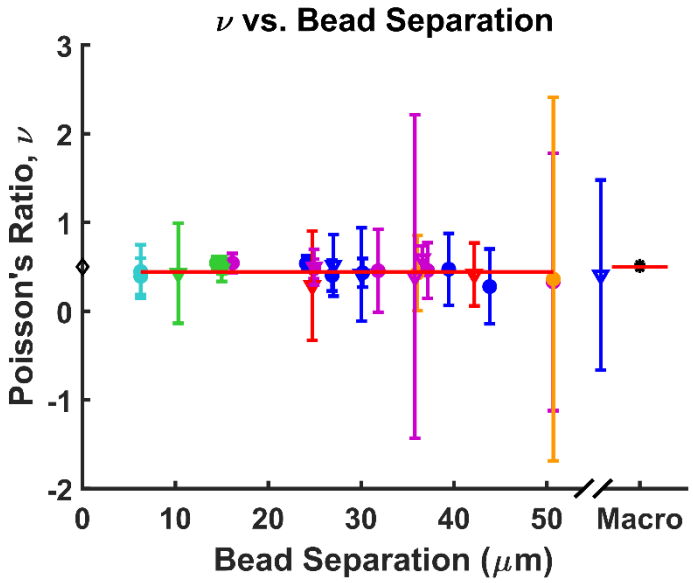

ν in Collagen

Poisson's ratio was found to vary widely in collagen (Figure 8.11). A ceiling value of approximately 0.5 was observed for ν, corresponding to the upper limit allowed by elasticity theory. Similarly, a floor value of approximately -0.5 was observed, corresponding to a theorized limit in Poisson's ratio for linear elastic materials.[59] The mean value was 0.13 ± 0.25. Trend in mean value versus bead separation was not quantified for ν in collagen gel.

Figure 8.11: Poisson's ratio, ν, versus bead separation, r, in collagen gel.

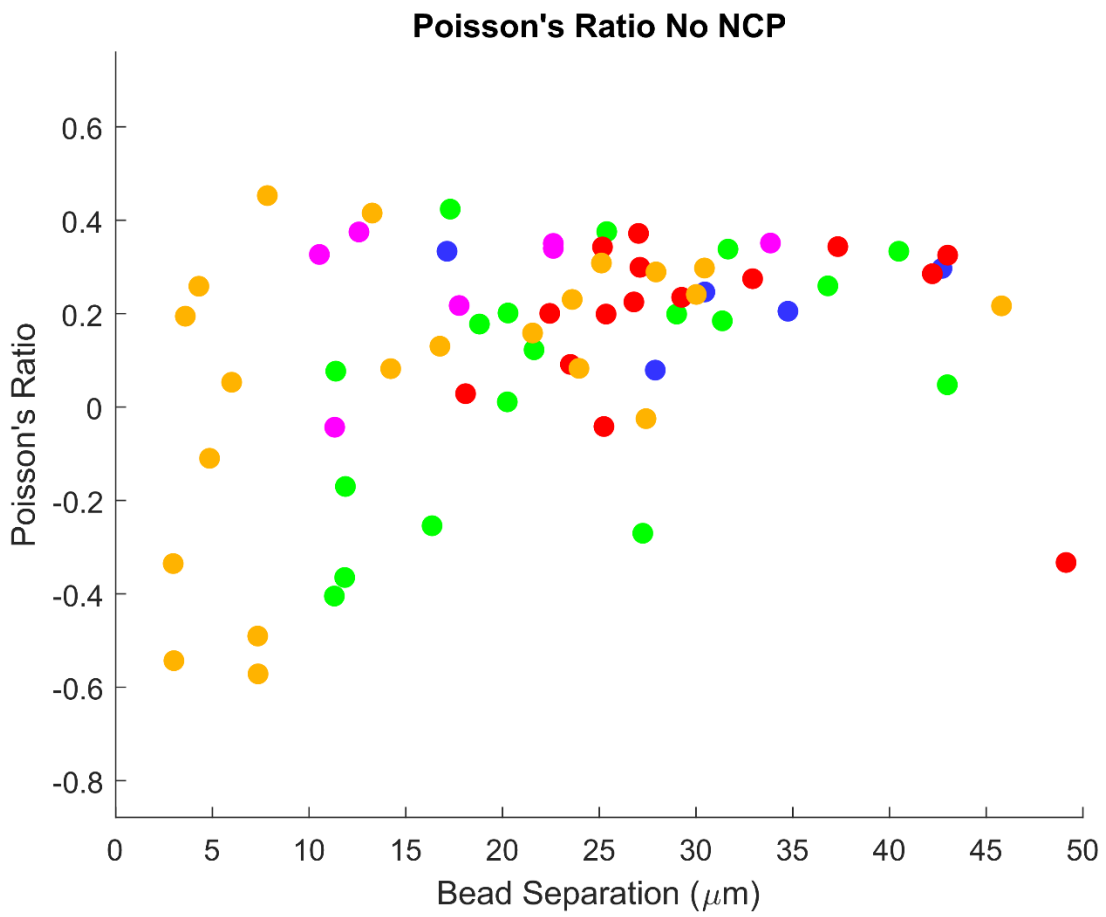

ν in Agarose

In agarose, ν was only observed to have positive values, but scatter in 2P data overshot the upper limit of 0.5 for elasticity theory. None of the linear fits between force and displacement in agarose had fits with r-squared > 0.95, leading to error bars for ν which greatly exceed the observed, already large, scatter.

Figure 8.12: v versus bead separation in agarose gel. Hollow triangles indicate data points for which the fits used to generate coupling matrices had r-squared < 0.95. v cannot be determined experimentally through 1P analysis, so an assumed value of 0.5 is shown for 1P data.

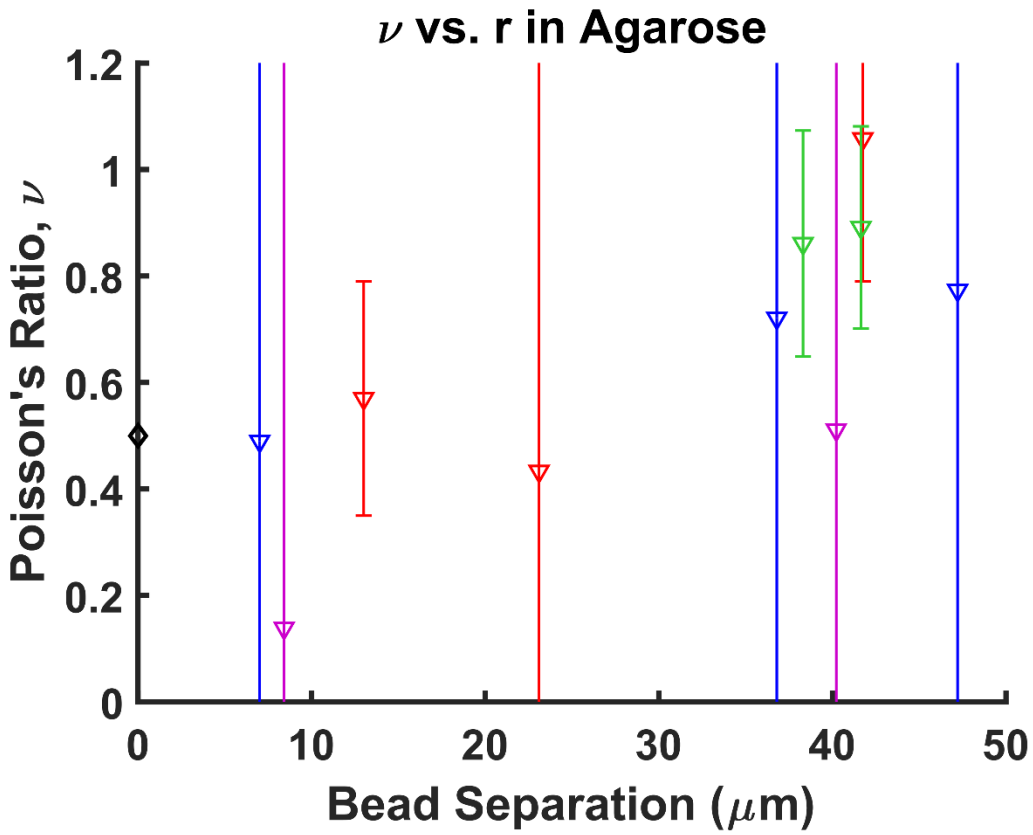

Shear Modulus, G

G in PAA

The purely elastic component of shear modulus, G, was observed not to have trends in mean value versus bead separation in PAA gels for 2P data in the gels with low and medium levels of cross-linking (Figure 8.13 and Figure 8.14), and to plateau in PAA gel with high cross-linking at large bead separation distances (Figure 8.15). However, the highly cross-linked gel shows a sharp increase in G as bead separation distance approaches zero. A statistically significant bias was observed between G from 1P and 2P data at large bead separation for the gel types with low and medium cross-linking, but not for the highly cross-linked gels. In PAA gel with 0.034% bis-acrylamide, G_{1P} = 24.5 ± 2.2 Pa, and G_{2P} = 34.0 ± 3.4 Pa. In PAA gel with 0.05% bis-acrylamide, G_{1P} = 73.4 ±

4.8 Pa, G_{2P} = 97.3 ± 7.6 Pa, and G_{macro} = 93.1 ± 6.9 Pa. This was the only gel for which macroscopic tests were done, and G_{2P} was statistically indistinguishable from G_{macro}. In PAA gel with 0.2% bis-acrylamide, G_{1P} = 457.4 ± 22.6 Pa, and G_{2P} = 507.5 ± 168.6 Pa. Fitting of an exponential to G_{2P} in PAA gel with 0.2% bis-acrylamide yielded a plateau value of G_{2P} = 400 ± 61 Pa.

Figure 8.13: Elastic shear modulus in PAA gels with 0.034% bis-acrylamide, the lowest level of cross-linking.

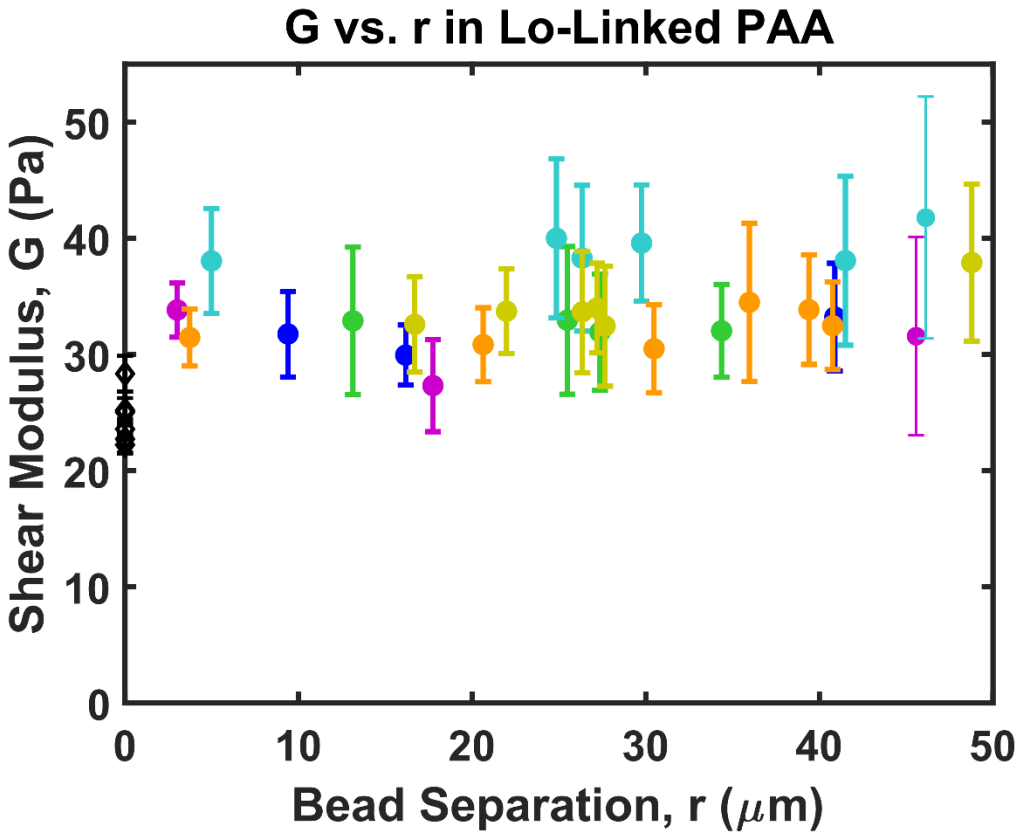

Figure 8.14: Elastic shear modulus in PAA gels with 0.05% bis-acrylamide, the intermediate level of cross-linking.

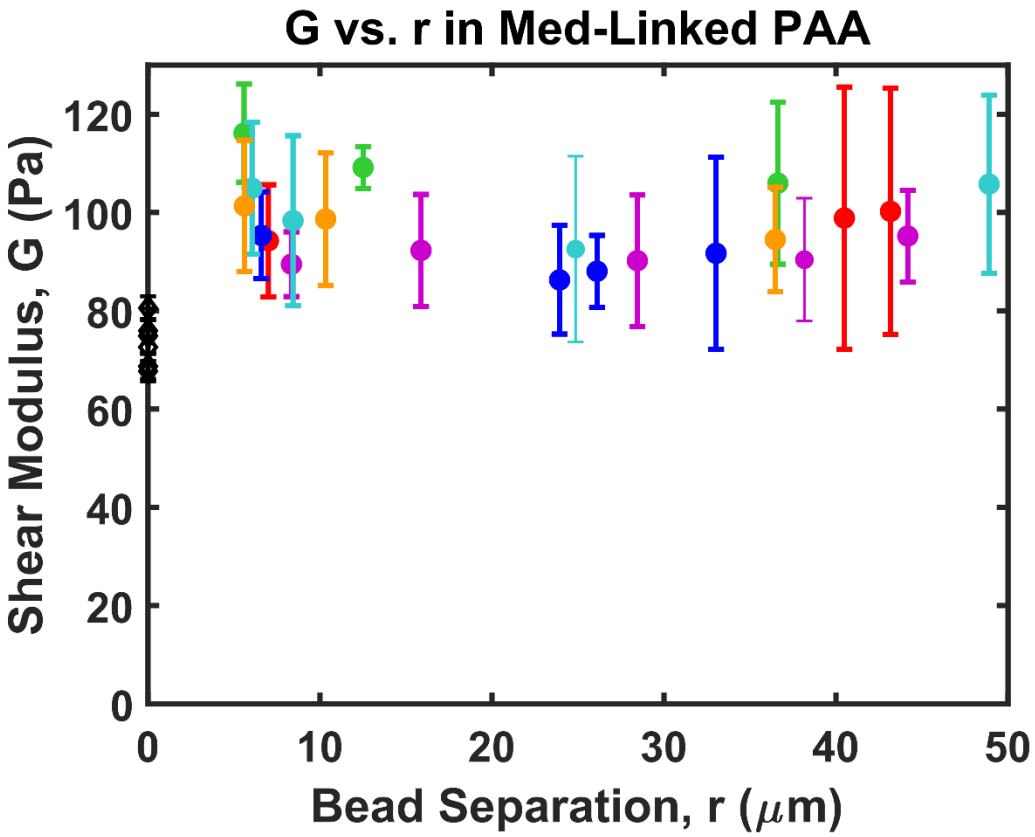

Figure 8.15: Elastic shear modulus in PAA gels with 0.2% bis-acrylamide, the highest level of cross-linking.

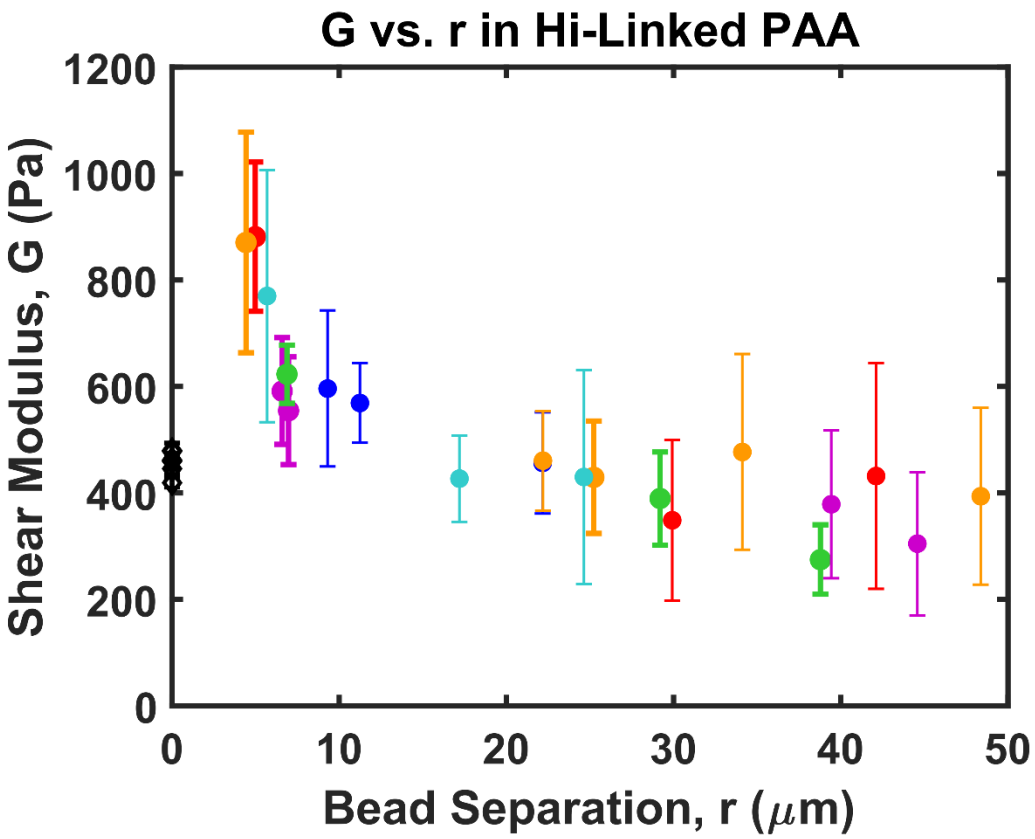

G in Collagen

Elastic shear modulus in collagen gels was found to decay with respect to bead separation in a manner which was well-fitted by an exponential when including both 1P and 2P data. The plateau value of elastic shear modulus in plain collagen gels was within 12% of the value obtained through macroscopic shear rheometry (G_{macro} = 45±2 Pa). To determine whether the rise in G2P with small bead separation could be explained by densification of collagen around beads forming an effectively rigid particle with approximately twice the radius of the bead, material property calculations were performed with bead radius set to double the radius of the

actual beads. The results, shown in Figure 8.17, are a 50% drop in G_{1P} and a nearly negligible drop in values of G_{2P} near the driven bead.

Figure 8.16: Elastic shear modulus in collagen gels without NCPs. A decay in modulus versus bead separation was observed which was well-fit by an exponential using both 1P and 2P data. Different colors represent different samples.

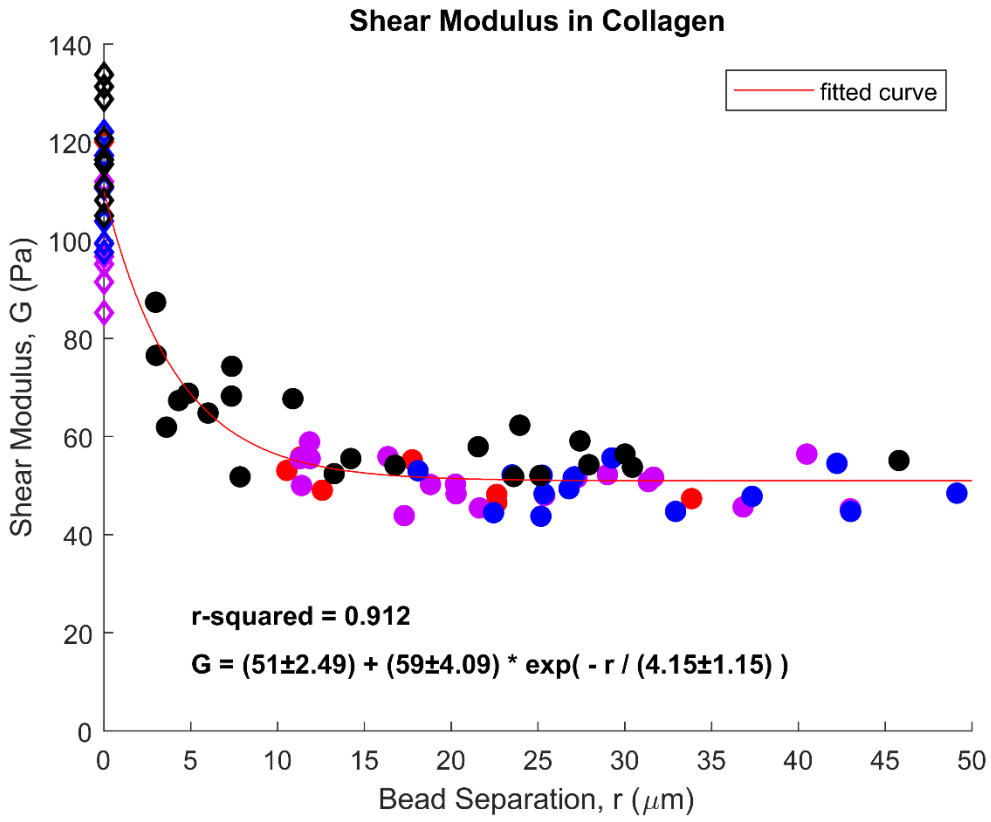

Figure 8.17: G versus r in collagen with bead size doubled in the equation for calculating modulus. The values shown are from the collagen gel sample identified by black dots in Figure 8.16. G_{1P} drops by a factor of two, but G_{2P} still increases as bead separation decreases. Different colors represent different constellations of beads within the same sample.

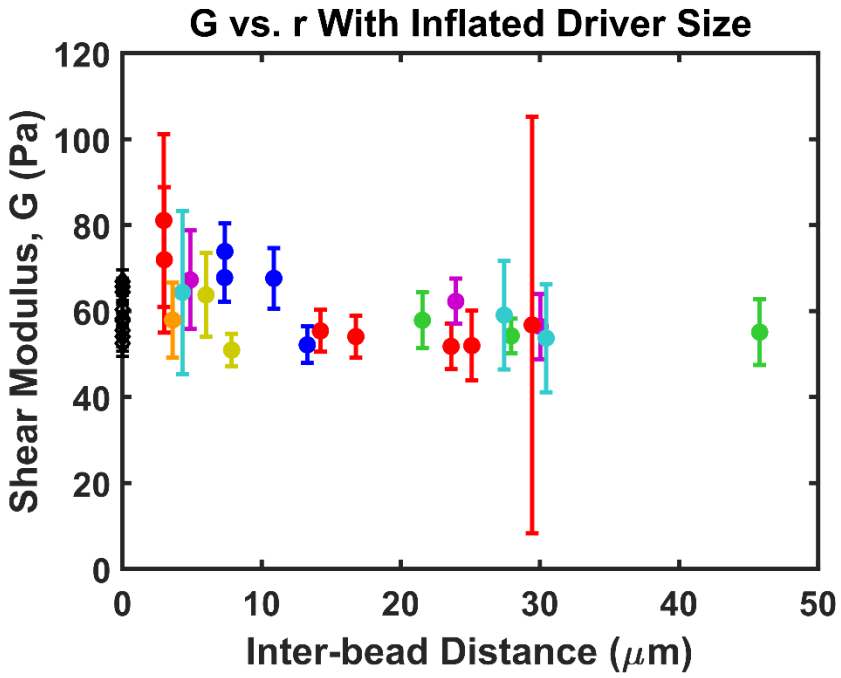

G in Agarose

Elastic shear modulus, G, in agarose was statistically different between 1P and 2P data, with scatter over a factor of 3 in 2P data. G_{1P} was smaller than G_{2P} by over a factor of 5, with G_{1P} = 42 ± 13 Pa and G_{2P} = 233 ± 103 Pa. The value of G_{2P} did not depend on *r* in agarose and had very high standard deviations between bead pairs of similar separations.

Figure 8.18: Elastic shear modulus, G, in agarose gel. A statistically significant difference was observed between 1P and 2P values, although no data point had r-squared ≥ 0.95 for the linear fits used to generate coupling matrices and, subsequently, G.

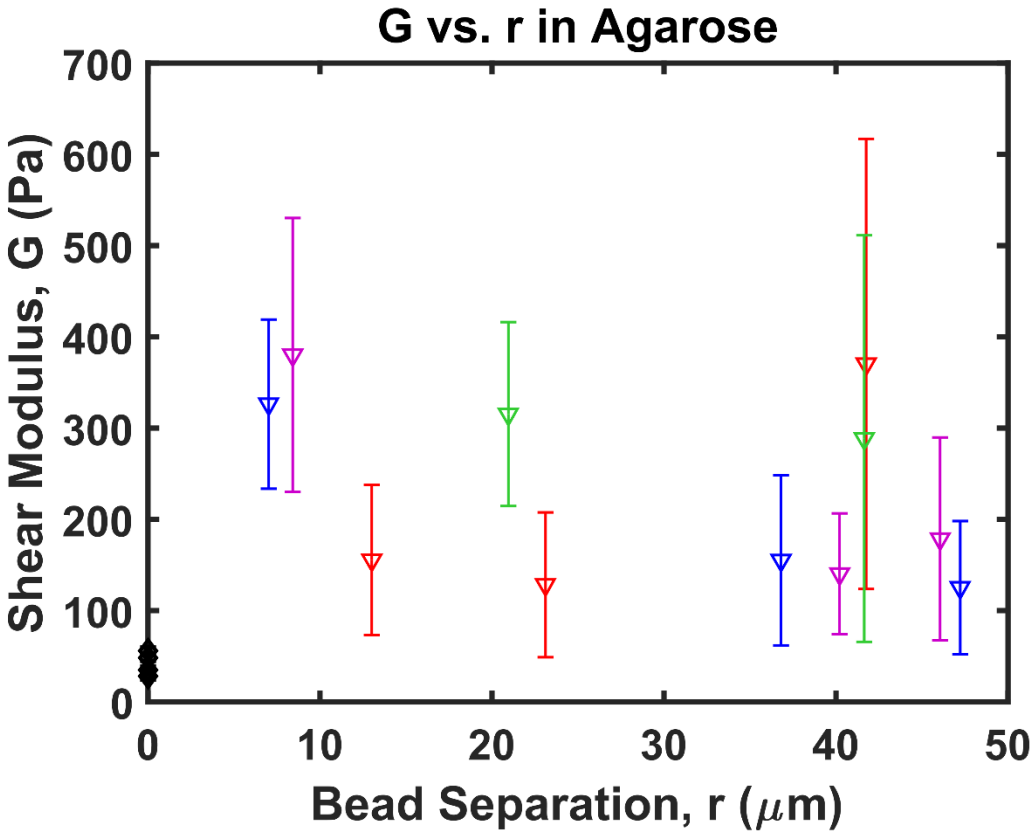

Evidence of Sheaths

The authors hypothesize that the deviation of G_{1P} from G_{2P} and G_{macro} in polyacrylamide is a result of sheaths of material around each bead, softened relative to the bulk material by altered polymer network formation. To test the hypothesis, G_{1P} was measured in finite element (FE) simulations of beads encased in sheaths of thickness *t* and elastic shear modulus G_{sheath} within an otherwise homogenous, linear elastic medium. A model with *t/a* = 0.1 is shown in Figure 8.19a. Increasing *t/a* or decreasing G_{sheath} led to a decrease of G_{1P} relative to G_{bulk} as shown in Figure 8.19b. For each *t/a*, a corresponding value of G_{sheath} was found so that the simulation

results matched the experimentally observed ratio G_{1P}/G_{2P}. This model employed a purely linear elastic material model, and thus could not generate any nonlinear response. This aspect may not reflect the reality of a sheath, which could be compressed and stiffen through densification. An alternative model did not include a sheath but rather a bead-gel interface with zero tensile strength. The results yielded $G_{1P}/G_{2P} = 0.37$, greatly underestimating experimental values.

Also explored was experimental evidence for existence of a sheath in the form of higher harmonics in driven bead displacement. It was found that driven bead displacement was not a pure sine wave at 2 Hz, but instead included a third harmonic with amplitude $A_{6Hz}/A_{2Hz} = 4.0 \pm 2.2\%$. This third harmonic component observed in driven bead displacement, and expressed in Equation 8.15, reflects some combination of nonlinear elasticity of the gel and non-sinusoidal trap force. Nonlinearity was observed in calibrations of the trap force versus trap-bead position offset, but a simulation of the experimental apparatus and a purely linear elastic gel having $G_{1P} = 16$ Pa generated third harmonics with amplitude A_{6Hz}/A_{2Hz} = -0.3%. Thus, nonlinearity of the optical trap marginally increases the amplitude of third harmonics attributable to gel mechanics. Figure 8.19d shows the force-displacement curve for a driven bead with the experimentally observed harmonic ratio, yielding an instantaneous G_{1P} lowest near zero displacement and increasing with displacement in either direction. Third harmonics for receiver beads were statistically indistinguishable from zero. Nonlinearity in driven bead displacement pointed to a localized effect corresponding to a sheath.

$$\boldsymbol{u_X^D = A_{2Hz} \sin(4\pi t) + A_{6Hz} \sin(12\pi t)} \tag{8.15}$$

To further examine the presence of sheaths as a function of gel microarchitecture, gels were prepared with various concentrations of bis-acrylamide, a cross-linking agent. As shown in Figure 8.19c, with increased crosslinking, the amplitude of the third harmonic decreased from $A_{6Hz}/A_{2Hz} = 4.0 \pm 2.2\%$ at 0.76 molar percent crosslinker (0.034% bis-acrylamide) down to $A_{6Hz}/A_{2Hz} = -0.3 \pm 3.2\%$ at 2.98 molar percent

crosslinker (0.2% bis-acrylamide), perfectly matching the harmonics attributable to trap shape. In tandem with this decrease in harmonic amplitude, G_{1P}/G_{2P} increased from 0.78±0.09 to 1.04± 0.16.

Figure 8.19: a) A FE model of a bead in gel with a sheath of different modulus surrounding the bead. b) G_{1P} as a fraction of G_{bulk} for variations of the FE model in panel c with different combinations of sheath thickness and stiffness. Experimentally observed ratios for collagen, polyacrylamide, and agarose gels are overlaid to highlight possible intersections. c) Experimental ratios of 1P to 2P shear moduli, G_{1P}/G_{2P}, and 3rd harmonic amplitude to fundamental amplitude, A_{6Hz}/A_{2Hz}, versus amount of bis-acrylamide (crosslinker). d) Force vs displacement for a bead with a third harmonic in displacement of amplitude A_{6Hz}/A_{2Hz} = 4% under sinusoidal force. The instantaneous slope of the curve gives different values of G_{1P} at different displacements, both higher and lower than the average value of 72 Pa calculated without the harmonic.

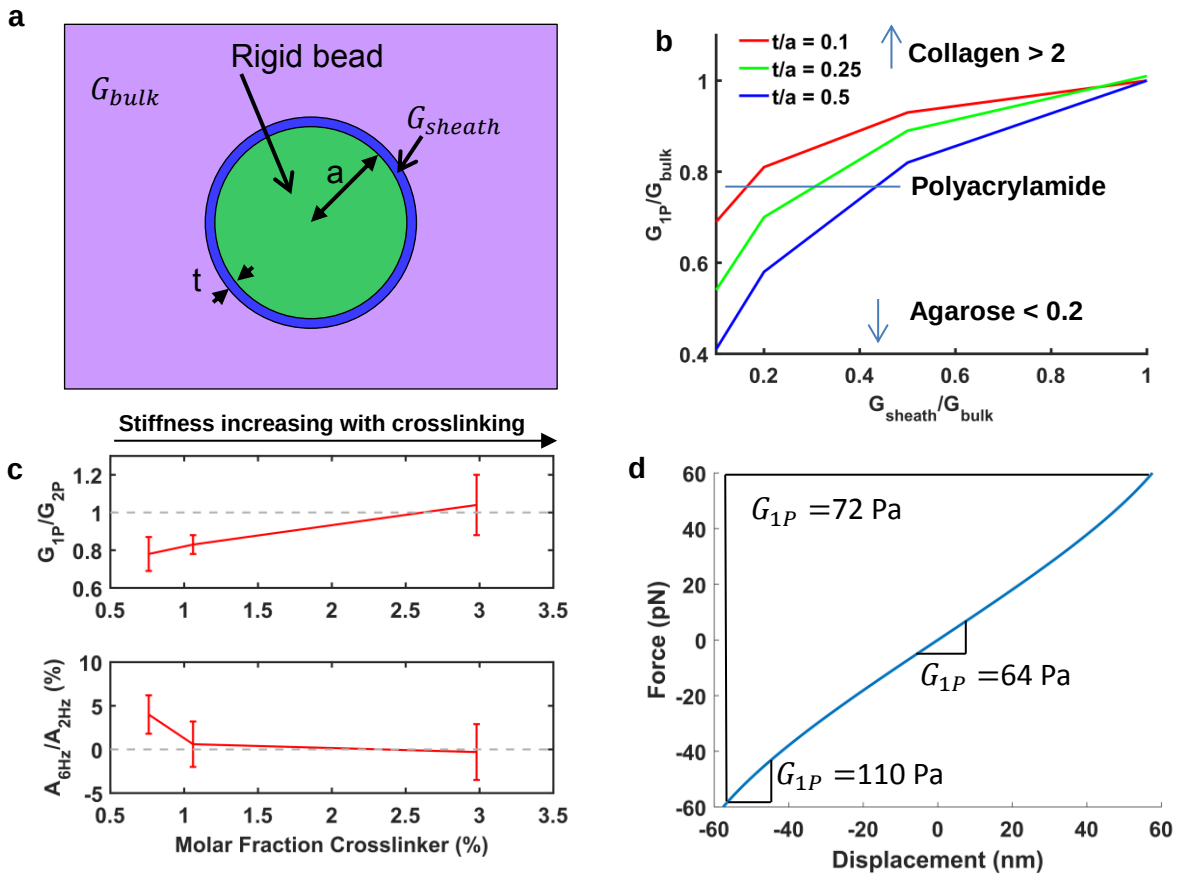

Discussion

The 2P method advances active microrheology to the point of precise, accurate measurement of gel mechanical properties versus the length scale defined by bead separation. Key innovations, laid out in Table 8.1, were necessary for accuracy in measurements, for precision in measurements, and for broadening the set of effective mechanical properties which could be measured. Robust, precise bead tracking through refinement of correlation particle tracking represents a significant increase in precision over the widely used, yet now outdated method described by Crocker and Grier over 20 years ago.[22,23] Large, sinusoidal trap displacements, enabled by trap force mapping, generated large bead displacements well-suited to Fourier analysis. Refinements in the use of Fourier analysis in active microrheology minimized uncertainty and avoided bias in measured amplitudes, as well as defining phase lag and nonlinearity in force-displacement relationships. Force-displacement coupling matrices were generated by fitting bead displacement versus applied force for the multiple angles of force from star driving, which both tested linearity of the relationship and defined viscoelastic material properties. Simultaneous collection of 1P and 2P data, along with pairing of measurements with bead separation, provided the ability to examine length scale effects. The increased ability of the 2P method to characterize material properties is a direct result of the innovations made during its development.

PAA, agarose, and collagen gels were tested using the 2P method to highlight the advances made in the method. PAA has been widely reported as being essentially linear elastic and homogenously isotropic over a large span of strains, making it a model material for demonstrating accuracy and precision of the method.[5,36,49] Agarose was chosen because it is well-known as a heterogeneous material with large pores, providing a counterpoint to the homogeneity of PAA gels.[50–53,60,61] Collagen is of great interest in biomedical research, having a fibrillar structure that leads to both bulk strain stiffening and long distance communication between cells through formation of "stress conduits."[2,4,6,8,9,14,15,30,54,62–67] These features made it a plausible candidate

for novel behavior. A model linear (visco)elastic material, a heterogeneous material, and a nonlinear material provided a broad range of characteristics with which a new microrheology method could be validated.

An immediate validation of the 2P technique was the equivalence of elastic shear modulus in 2P data to the macroscopic value in PAA gel with 0.05% bis-acrylamide. In contrast, the highest modulus produced by the 1P technique was lower than the lowest modulus from macroscopic measurements. This underestimation of modulus in 1P data agrees qualitatively with Dasgupta and Weitz's comparison of single and multi-particle modulus using the same concentrations of acrylamide and bis-acrylamide.[29] Expanding on this, the systematically low values of G_{1P} and the third harmonics of driven bead displacement observed were explained well by a sheath of abnormally soft material encasing each bead. Microrheology practitioners and theoreticians warned almost 20 years ago that single-particle microrheology is susceptible to erroneous results because of these sheaths and should be replaced by two-particle microrheology.[13,16,18,46,47,68] Passive microrheology, the original context in which bias between single-particle and multi-particle modulus was observed, relies on the same fundamental relationship between force and displacement as the 2P active microrheology method presented here. The results presented here not only demonstrate the unpredictable nature of bias in single-particle measurements, but also demonstrate the ability to detect a soft sheath and determine sheath properties through use of harmonic analysis in bead displacement. Conversely, the 2P method was able to independently verify macroscopic measurements specifically because it did not rely on the bonding of beads to the gel or the absence of localized heterogeneities, but instead relied on transmission of force through the bulk material to generate displacement at a distant point. The applied force was calculated without any assumptions about the gel, enabling measurements robust against deceptively large or small displacements of the driven bead. Regardless of other benefits, the insensitivity of 2P measurements to localized property disturbance combined with the ability to quantify those disturbances with data collected as part of the process makes it a clear replacement for solely single-particle measurements.

Beyond providing shear modulus, the 2P technique provides the data necessary for multiple tests of linearity and isotropy, for determination of ν to fully define isotropic material elastic constants, for characterization of viscoelastic effects, and for quantification of all of the above versus bead separation distance and bead pair angle. The ability of multi-particle measurements to obtain Poisson's ratio had been shown previously in studies using some prototype methods, but not at a level of development in which it was practical to make systematic studies.[11,48] Using the 2P method, Poisson's ratio was measured at bead separations from under 3 μm to over 50 μm. Poisson's ratio is especially sensitive to bias or scatter in the different force-displacement coupling modes, so obtaining a value which was statistically indistinguishable from the macroscopic value was an excellent demonstration of both precision and accuracy in measurements. In higher modulus gels for which bead displacement would be decreased for a given applied force and bead separation, longer videos or higher precision optics would both increase precision, and stiffer samples would have decreased thermal displacements, helping to compensate for the decreased displacement signal by increasing precision. Figure 8.20 presents an approximate expectation of material stiffness versus the maximum bead separation which can be probed, neglecting the decrease in thermal displacement amplitude in stiffer materials, or the use of longer data collection times or more precise optics. Compared to the simple stiffness data typically extracted from 1P data, the 2P technique represents a transformative leap in mechanical characterization of 3D matrices.

Figure 8.20: A schematic estimation of the maximum modulus which can be measured at a given bead separation. Approximate moduli for different tissue types were taken from Engler et al. and from Comley and Fleck.[1,69]

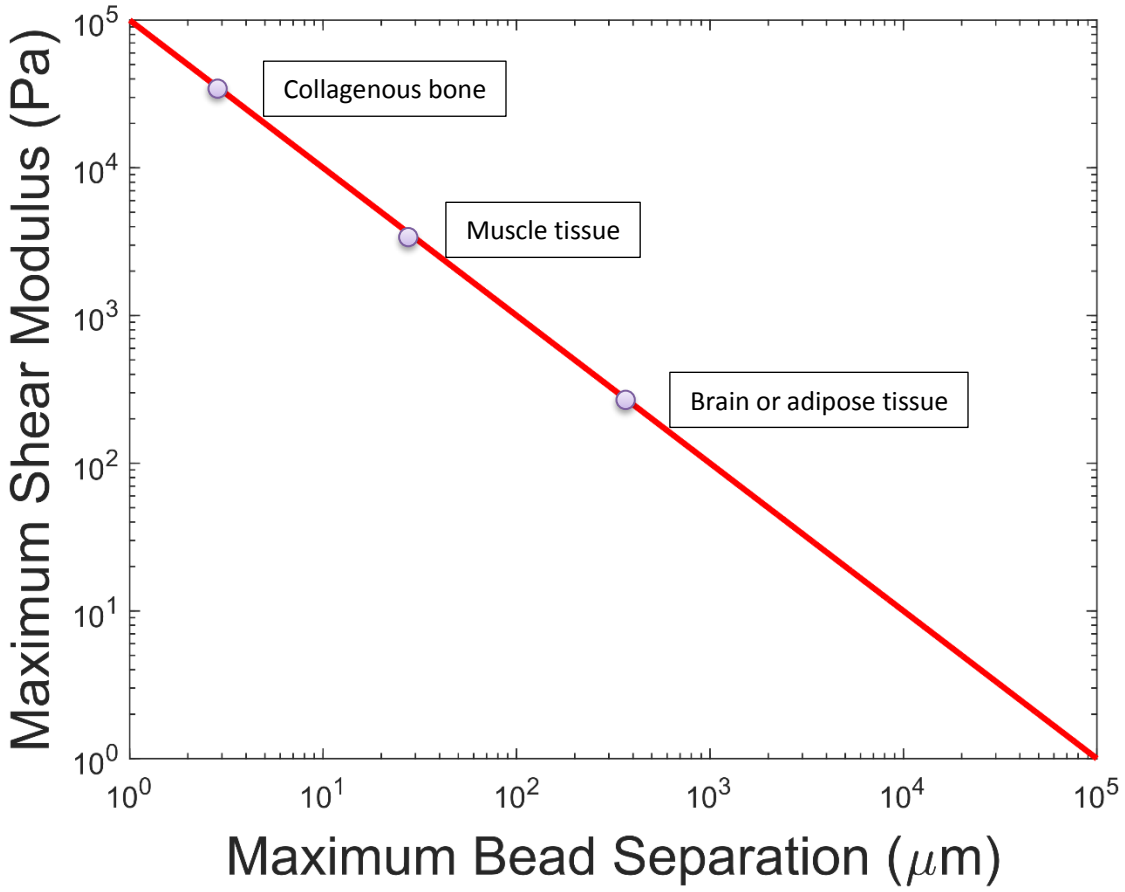

The value of measuring properties versus bead separation was apparent in measurements made on each material. Phase lag was found to increase versus bead separation in both PAA and collagen gels, two very different systems. PAA gels contained 3% PAA in the form of networked single polymer backbones, while collagen gels contained 0.2% collagen in the form of fibrillated triple-helices.[9,36,62] This is especially interesting as the phenomenon has never before been seen, to the authors' knowledge. Data on viscous versus elastic Poisson's ratio was even able to suggest fluid flow through the network as a mechanism for the phase lag

phenomenon in PAA gels. Such a measurement would have been fundamentally impossible with 1P, and practically impossible with either passive 2P methods or less precise/accurate active microrheology. The decay of observed modulus in collagen and highly cross-linked PAA with bead separation was also surprising, and nicely contrasted by the observation of constant modulus versus bead separation in the two PAA gels with lower cross-linking. These observation present the ability to study viscoelastic force coupling, and the material properties those couplings define, as a function of length scale (bead separation distance), allowing exploration of fundamental mechanisms, such as viscous drag between liquid and network components.

Expanding beyond the extensive set of isotropic properties measured, there is the potential to quantify anisotropic material properties. Pan and Chou developed a force-displacement equation for a transversely isotropic material which is analogous to the isotropic equation we used in this study.[70] A transversely isotropic material has five independent elastic constants as opposed to the two constants defining an isotropic material, but a sufficiently dedicated effort should be able to tease out material properties using displacement of multiple receivers. The potential for this advance is laid out in Figure 8.21. First, a transmission matrix is generated as in Figure 8.21a by relating each component of force on a driven bead to the two components of displacement induced in each receiver bead. The relationship between elements of that transmission matrix will vary dramatically with the orientation of the bead pair, as illustrated in Figure 8.21. Noting that $T_{rt} = T_{tr}$ for a transversely isotropic material, there are still 3 independent measurements produced by each bead pair. The 6 independent values of force-displacement coupling strength from two receivers could potentially determine all 5 elastic constants and the material orientation. More complex materials with even more independent elastic constants might also be possible to quantify through numerical models, neural networks, or the development of analytic methods.[71]

There are many potential applications for the ability of the 2P technique to quantify mechanics in a 3D environment, one of them being the characterization of mechanical properties in specific regions of 3D matrices as cells migrate and remodel the matrix. Techniques such as 3D traction force microscopy generate

previously unobtainable maps of cell traction, yet rely on a priori knowledge of matrix mechanics.[72] As cells are known to remodel the matrix via physical realignment of fibers, stress-dependent enzymatic degradation of the existing fibers, and controlled deposition of new matrix, there is every reason to expect future knowledge of mechanotransduction could benefit from 2P measurements of evolving matrix mechanics.[55,62,73–77]

Figure 8.21: a) In isotropic materials, the magnitude (strength) of each force-displacement coupling mode is unchanging with orientation of a bead pair for a given inter-bead distance. b) In anisotropic materials, the magnitude of each coupling mode varies with angle. The relative amplitudes of the different elements are shown for all angles in the material, and highlighted for a particular bead pair orientation.

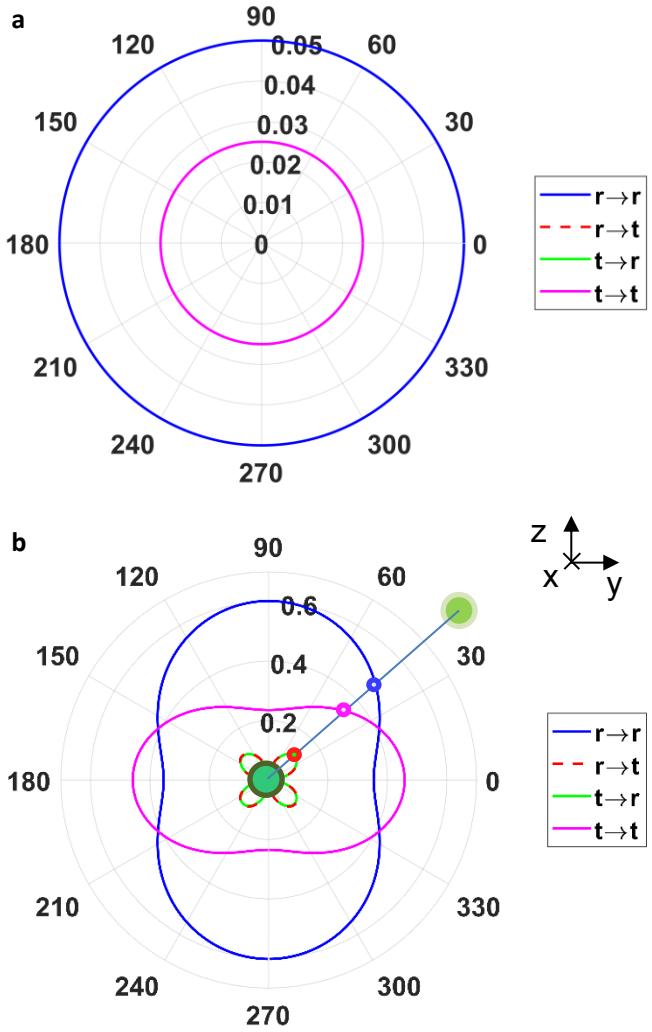

Table 8.2: Findings in probing micromechanics versus length scale with 2P microrheology.

Finding	Description	Impact
G1P was different than G2P at large bead separations	For sufficiently large bead separations, G_{2P} was greater than G_{1P} in PAA and agarose, and less than G_{1P} in collagen.	Different gels have different biases in 1P data. Not only the magnitude, but also the sign of the bias is material specific.
Phase lag increased with bead separation in PAA and collagen gels	Phase lag of bead displacement with respect to trap displacement increased with bead separation	Collagen and PAA gels exhibited nonlinear viscoelasticity, which may relate to fluid flow.
Cross-linking modulates phase lag	Phase lag in PAA increases more rapidly with bead separation when cross-linking is increased.	Trends in phase lag versus bead separation were modulated by changing network structure with constant network density.
Phase lag in PAA increases with decreasing peak strain at constant frequency.	In PAA, phase lag in macroscopic shear rheometry increases with decreasing strain and strain rate at constant frequency, but the strain/strain rate amplitude for this effect is lower than the strain/strain rate for which the phenomena is observed in 2P data.	It is proposed that phase lag rises at larger strain/strain rate in 2P data than in macro shear rheometry due to rate-limited fluid motion through the polymer network.
Elastic 2P data converges with elastic macro data with increasing bead separation	When measuring only displacement/strain in phase with applied force/torque, G_{2P} agrees well with G_{macro} at large bead separations.	Models of 2P data predicted convergence with macro data at large bead separations. This was experimentally corroborated for elastic force-displacement coupling.
Viscous v_{2P} in PAA indicates compressibility	Elastic v_{2P} in PAA was statistically indistinguishable from 0.5, consistent with an incompressible material, but viscous v_{2P} was less than 0.5, consistent with compressibility.	Fluid flow through the network may be the mechanism behind nonlinear viscoelasticity in PAA gels.
Third harmonics in driven bead displacement in PAA gels	Driven bead displacement had third harmonics corresponding to material stiffness increasing with bead displacement. The harmonic amplitude and ratio of G_{1P} to G_{2P} were found to agree with a sheath around the driven bead of a specific stiffness and thickness.	Sheaths of altered material around beads have been known to bias 1P data for nearly 20 years. However, this may be the first time a single experiment has been able to simultaneously define sheath thickness and stiffness.
Third harmonics and bias in G_{1P} decrease with increasing cross-linking in PAA gels	Third harmonics and bias in G_{1P} go to zero in PAA gels with increased cross-linking.	The thickness of the sheath around beads decreased with network mesh size.

Methods

Polyacrylamide Gel Preparation

Polyacrylamide gels were made according to the protocol from Fischer et al.[36] Except where noted, the gels contained 3% acrylamide and 0.05% bis-acrylamide (Sigma-Aldrich, St. Louis). Variations in crosslinker (bis-acrylamide) density were achieved with bis-acrylamide concentrations of 0.034%, 0.05%, and 0.2%. Solutions intended for laser tweezers or tensile testing were mixed in a vial containing a small volume of 2.0 μm, yellow-green, carboxylate-modified Fluospheres (ThermoFisher, Waltham) and placed in a sealed chamber according to the steps in the protocol below. The total volume of beads used was less than 0.02% of the total sample solution volume. Samples for parallel plate rheometry were polymerized in the gap between the rheometer plates and with appropriate sample volume, but otherwise following the same steps. Samples for tensile tests were polymerized in "dogbone" molds having a 25 mm long gage section with a uniformly square cross section 4 mm on a side. Gauze squares were placed in the wide ends of the dogbone samples to facilitate gripping.

Protocol for PAA optical trap samples

Supplies

- 150 mm cell culture dish
- Lifting frame
- 3-4 sheets of gauze
- Microcentrifuge vial
- Precision #1.5 cover slip
- Microscope slide
- 1-2 mm self-adhesive imaging spacer with 20 mm cutout
- Fluosphere solution (Life Technologies Corporation, Carlsbad)

- 40% acrylamide solution (Bio-Rad Laboratories, Hercules), chilled
- 2% bis-acrylamide solution (Bio-Rad Laboratories, Hercules), chilled
- Triple-distilled water (TDW), chilled
- Tetramethylethylenediamine (TEMED)
- 10 wt% ammonium persulfate in triple-distilled water (APS), freshly made

Procedure

1. Stick the imaging spacer to the center of the microscope slide, creating a well.
2. Micropipette Fluosphere solution into the bottom of the microcentrifuge vial. The amount is:
    a. 5-6 µl when using 2 µm beads
    b. 2 µl when using 1 µm beads
3. Place the vial in a microcentrifuge for 5 minutes.
4. Cover the bottom of the cell culture dish with chilled TDW, then add the gauze and the lifting frame.
5. Remove the vial from the microcentrifuge and aspirate the supernatant.
6. Micropipette 75 µl of acrylamide solution into the vial, then pump the micropipette as necessary to distribute beads evenly into the solution without introducing bubbles.
7. Micropipette bis-acrylamide solution into the vial, then pump the micropipette ~3 times to mix the solution without introducing bubbles. The amount is:
    a. 17 µl for 0.034% bis-acrylamide
    b. 25 µl for 0.05% bis-acrylamide
    c. 100 µl for 0.2% bis-acrylamide
8. Micropipette TDW into the vial, then pump the micropipette ~2 times to mix the solution without introducing bubbles. The amount is:
    a. 898 µl for a 0.034% bis-acrylamide solution
    b. 890 µl for a 0.05% bis-acrylamide solution

c. 815 µl for a 0.2% bis-acrylamide solution

9. Micropipette 4 µl of TEMED into the solution, then use the micropipette from step 8 to mix the solution without introducing bubbles by pumping 2-3 times.
10. Micropipette 6 µl of APS into the solution, then use the micropipette from step 8 to mix the solution without introducing bubbles by pumping 5-10 times. This is the final solution and has begun the process of polymerization. There are only several minutes of working time after the APS is added.
11. Micropipette just enough of the final solution into the well formed by the imaging spacer on the microscope slide that the solution surface is very slightly convex.
12. Place the coverslip on top of the imaging spacer and press on the coverslip where it touches the imaging spacer to make a securely sealed chamber.
13. Wipe away excess solution using a low lint tissue.
14. Wait 12-24 hours before testing the sample.

Collagen Gel Preparation

Collagen gels were prepared at a concentration of 2 mg/ml. Samples for use with the optical trap were prepared according to the protocol below. Macroscopic samples were prepares similarly in disk-shaped molds, but without fluorescent beads.

Protocol for collagen optical trap samples

Supplies

- 150 mm cell culture dish
- Lifting frame
- 3-4 sheets of gauze
- Microcentrifuge vial

- Precision #1.5 cover slip
- Microscope slide
- 1-2 mm self-adhesive imaging spacer with 20 mm cutout
- Fluosphere solution (Life Technologies Corporation, Carlsbad)
- PureCol® Type I collagen solution (Advanced BioMatrix, San Diego)
- PBS, chilled
- Triple distilled water (TDW), chilled
- 1 Normal NaOH solution

Procedure

1. Calculate the volume of components to be added. The final concentration should be 2 mg/ml of collagen and 1% 1 Normal NaOH solution, with the rest of the volume being PBS.
2. Stick the imaging spacer to the center of the microscope slide, creating a well.
3. Micropipette Fluosphere solution into the bottom of the microcentrifuge vial. The amount is 1% of the total solution volume when using 2 µm beads, or half that when using 1 µm beads.
4. Place the vial in a microcentrifuge for 5 minutes.
5. Cover the bottom of the cell culture dish with chilled TDW, then add the gauze and the lifting frame.
6. Remove the vial from the microcentrifuge and aspirate the supernatant.
7. Micropipette PBS into the vial, then pump the micropipette as necessary to distribute beads evenly into the solution without introducing bubbles.
8. Micropipette NaOH solution into the vial, then pump the micropipette to mix the solution without introducing bubbles.
9. Micropipette PureCol® solution into the vial, then pump the micropipette for approximately 10 seconds to mix the solution without introducing bubbles. This is the complete solution and has begun the process of fibrillation. Any delay in pipetting will result in clumps of gel forming in the micropipette.

10. Micropipette just enough of the final solution into the well formed by the imaging spacer on the microscope slide that the solution surface is very slightly convex.
11. Place the coverslip on top of the imaging spacer and press on the coverslip where it touches the imaging spacer to make a securely sealed chamber.
12. Wipe away excess solution using a low lint tissue.

Wait 24 hours before testing the sample.

Agarose Gel Preparation

Agarose gels were prepared at a concentration of 0.4% (w/v) according to the protocol below.

Protocol for agarose optical trap samples

Supplies

- 20 ml beaker with magnetic stir bar, plastic wrap seal, and tape.
- 150 mm cell culture dish
- Lifting frame
- 3-4 sheets of gauze
- Microcentrifuge vial
- Precision #1.5 cover slip
- Microscope slide
- 1-2 mm self-adhesive imaging spacer with 20 mm cutout
- Ultra-low melt agarose powder (Affymetrix, Santa Clara)
- Triple distilled water (TDW), chilled
- PBS

Procedure

1. Measure out 0.04 g of agarose powder and empty it into the beaker containing a stir bar.
2. Add 10 ml of PBS to the beaker, then seal it with plastic wrap and tape the plastic wrap around the circumference of the beaker.
3. Place the beaker on a stir plate at 100° C with 200 rpm stirring until the agarose powder has fully dissolved.
4. Place the beaker in a small pan of room temperature water.
5. Stick the imaging spacer to the center of the microscope slide, creating a well.
6. Micropipette Fluosphere solution into the bottom of the microcentrifuge vial. The amount is 1% of the total solution volume when using 2 µm beads, or half that when using 1 µm beads.
7. Place the vial in a microcentrifuge for 5 minutes.
8. Cover the bottom of the cell culture dish with chilled TDW, then add the gauze and the lifting frame.
9. Remove the vial from the microcentrifuge and aspirate the supernatant.
10. Micropipette agarose solution into the vial, then pump the micropipette as necessary to distribute beads evenly into the solution without introducing bubbles. This is the complete solution and will gel if refrigerated.
11. Micropipette just enough of the final solution into the well formed by the imaging spacer on the microscope slide that the solution surface is very slightly convex.
12. Place the coverslip on top of the imaging spacer and press on the coverslip where it touches the imaging spacer to make a securely sealed chamber.
13. Wipe away excess solution using a low lint tissue.

Wait 24 hours before testing the sample.

Optical Trap Apparatus

An optical trap was set up around a Nikon eclipse TE2000-u microscope. The apparatus is shown in Figure 8.22, and a schematic of the light paths is shown in Figure 8.23. A 1064 nm laser was used to generate the trap, and a pair of galvanometric steering mirrors controlled via LabVIEW generating sinusoidal displacement of the trap at any chosen angle within the imaging plane. Bead fluorescence was induced with light from a mercury lamp passed through a FITC cube. Video of beads was captured using a CoolSnap EZ CCD camera (Photometrics, Tucson) controlled using MicroManager.[25] Video framerate was dependent on the field of view captured, but was verified for each bead geometry to be at or above 12 Hz, the minimum for which the Nyquist frequency would be at least 6 Hz, the 3rd harmonic of a 2 Hz driving signal. An exposure time of 10 ms was used during trials on gels and 1 ms during trap force calibrations trials to minimize blurring at higher bead velocities.

Figure 8.22: The optical trap apparatus, centered on a microscope with a piezo-actuated stage. The laser beam which forms the trap passes through an optical diode, a half-wave plate, and a polarizing beam splitter before being reflected off the two galvanometric steering mirrors, expanded in a telescope, and entering the objective lens. The beam is focused to a waist a few hundred micrometers above the objective lens, where it forms the optical trap. Fluorescense is excited light from a mercury lamp passed through a FITC filter. Imaging is achieved by a CCD camera with filters to pass in only light from bead fluorescence.

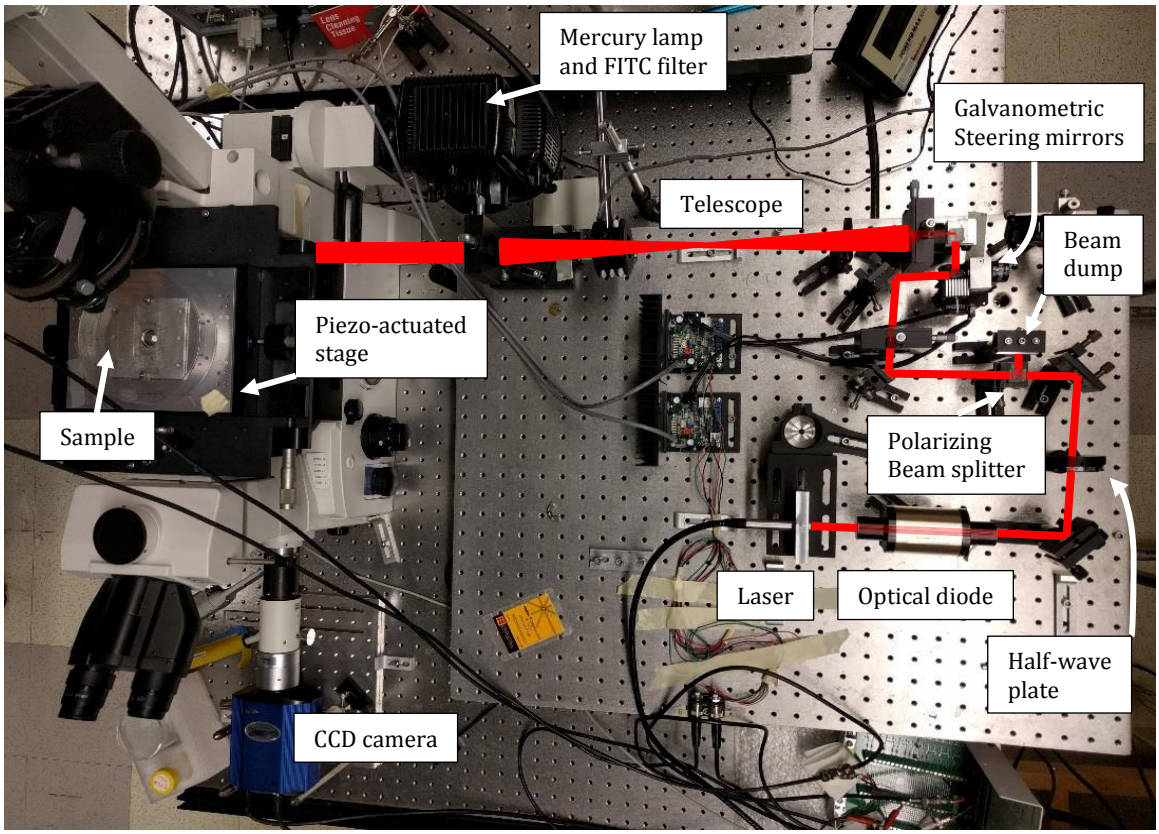

Figure 8.23: Schematic of the apparatus, including optical paths inside the microscope.

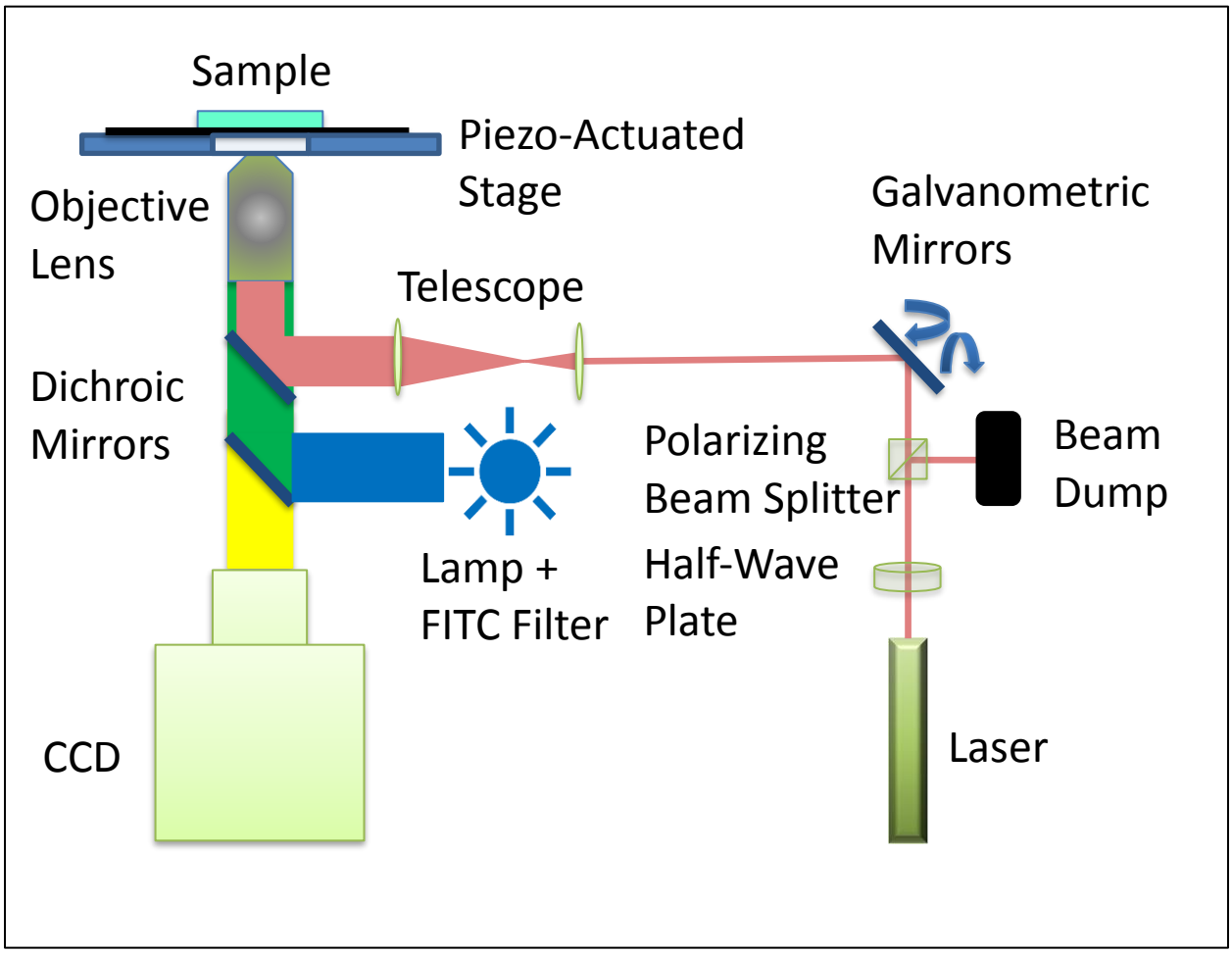

Apparatus Calibration

Pixel Size

Pixel size was calibrated using a slide micrometer along both axes. Images of the micrometer captured by the CCD camera were opened in ImageJ, where the micrometer was used to define pixel dimension.[78]

Stage Displacement

Stage displacement, used during trap force calibration trials, was determined by capturing video of a bead stuck to a coverslip on the stage as the stage was commanded to displace exactly as in trap force mapping. After using centroid particle tracking (because correlation tracking would have difficulty with blurring from relatively high bead velocity), bead position was plotted versus cyclic time. Cyclic time was obtained through a modulo operation on image frame time stamps in which the divisor was the period corresponding to the driving frequency. The data was then fit to a sin series with phase information, as in Equation 8.16.

$$\boldsymbol{X = X_0 + \sum A_i \sin(2\pi f t - \phi_i)} \tag{8.16}$$

Trap Displacement

Trap displacement, used to drive beads within a gel, was determined by capturing video of the laser spot focused on a coverslip surface as the trap was commanded to displace exactly as in bead driving trials. A filter was removed to allow sufficient light from the trap to reach the CCD camera. Trap position was found in each video frame by thresholding the image with a sufficiently high cutoff that only the laser spot was detected, then fitting the brightness in the detected region to a 2D Gaussian. The peak of the 2D Gaussian was determined to be the trap position. Fourier analysis was performed on the resulting position data, and trap displacement was defined 2 Hz displacement, including phase information from “in phase” and “out of phase” displacement of the trap.

Calculation of Trap Force

Trap force versus the bead-beam offset, δ, was calibrated by correlating an applied drag force of known amplitude with the bead-beam offset, δ. A bead in triple-distilled water was trapped, after which the stage, and hence the water surrounding the bead, was oscillated sinusoidally at 2 Hz in either the X or Y direction. Stage motion was generated by piezo actuators controlled by LabVIEW. A half-wave plate was rotated to divert a portion of the beam into a beam dump, reducing trap strength by approximately a factor of 20. This allowed

viscous drag from the oscillating water to pull the bead across the entire range of bead-beam offsets expected during trials on gels. Trap force was also verified to scale linearly with trap power at the emitter, with driven bead displacement divided by laser power being constant, plus or minus 8%. The oscillation was specified to remain at a constant amplitude of 20 μm for the duration of a 5000 frame video. The amplitude of the viscous drag force was calculated using Stokes' law, given in Equation 8.17. In this equation, η is the dynamic viscosity of the water, r the radius of the bead, and v the relative velocity of the water with respect to the bead. Trap force was mapped for the largest span of offsets possible, and an effective spring constant was calculated based on the peak offsets observed during experiments.

$$F_d = 6\pi\eta r v \tag{8.17}$$

Trap Force Mapping Protocol

Supplies

- Precision #1.5 cover slips
- Microscope slide
- Double-sided mounting tape. Gorilla Glue™ clear mounting tape was found to work well.
- Triple-distilled water (TDW)
- Fluosphere solution (Life Technologies Corporation, Carlsbad) diluted ~10,000:1 in TDW

Procedure

3. Map stage displacement and velocity
    a. Place small drops of diluted fluosphere solution onto a cover slip, let them dry out, and place the cover slip on the stage.

b. Command sinusoidal stage displacement of the same amplitude and direction(s) that will be used to generate fluid velocity over a trapped bead in water. Capture video of the bead displacement with the shortest possible exposure time to minimize blurring.

c. Perform particle tracking on the video, plot the resulting position versus cyclic time (time modulo the period of sinusoidal stage displacement), and fit a sin series with phase information (Equation 8.16) to the resulting data. This defines stage position versus cyclic time, and the derivative of the sin series defines stage velocity versus cyclic time.

4. Use a bead trapped in water to correlate drag force with bead position.

   a. Set the trap laser to the power which will be used in microrheology data collection and turn on the lamp used to excite fluorescence in the beads.

   b. Apply a single piece of mounting tape to the microscope, as close to the dimensions of the cover slip as possible. If the mounting tape is less than 1 mm thick, it may be a good idea to apply two thicknesses of tape.

   c. Cut a rectangle in the center of the mounting tape (approximately 10x20 mm) and peel the inner tape away from the slide, leaving a "well" of tape on top of the slide.

   d. Slightly overfill the well with diluted Fluosphere solution and place the coverslip down over the well to create a sealed chamber. Make sure to lower the cove slip evenly so the excess water escapes out the sides without leaving air bubbles in the chamber.

   e. Place the sealed chamber on the stage, cover slip side towards the objective lens.

   f. Capture a floating bead in the trap.

   g. Command sinusoidal stage displacement of the same amplitude used to map trap position and velocity. While using live video view in μManager, rotate the half wave plate upstream of the polarizing beam splitter in the trap beam path until the amplitude of bead displacement is sufficient to cover that range of bead-trap offsets expected in experimental data.[25]

h. Capture video of the bead oscillation during sinusoidal stage displacement, using the shortest possible exposure time to minimize blurring.

i. Measure beam power in the telescope section of the beam path with the half-wave plate at the same angle of rotation used to enable large displacements of the trapped bead. Measure the power again with the half-wave plate rotated to allow maximum power along the branch of the beam path which forms the trap.

j. Perform particle tracking on the video, plot the resulting position versus cyclic time (time modulo the period of sinusoidal stage displacement), and duplicate the data with one period of stage displacement added, creating two cycles of identical bead displacement data.

k. Smooth the two cycles of data in MATLAB using the smooth function with span specified and method set to *rloess*, which is a local regression smoothing method which progressively decreases the weighting used for outliers, reaching zero weight at six mean absolute deviations. Span width should be set to the minimum value possible without generating obvious noise. The smoothing operation has non-ideal performance at the ends of the data set, which is why a second identical cycle is used. With the second cycle, a full cycle of data can be extracted without approaching either end of the data set.

l. Fit a sin series with phase information (Equation 8.16) to the smoothed data starting half a cycle into the data and ending half a cycle before the end of the second cycle. This defines stage position versus cyclic time, and the derivative of the sin series defines bead velocity versus cyclic time.

m. Calculate drag force on the bead according to Stokes' law, with fluid velocity defined by stage velocity minus bead velocity. Multiply this force by the ratio of maximum beam power to reduced beam power found in step i so that the force curve will represent the force at

maximum power, rather than at the effectively reduced power used to enable large bead displacement.

n. Identify the time point in the cycle at which fluid velocity crosses zero. Subtract the corresponding bead position at that time point from all bead position values because this is the resting bead position (position at zero drag force).

o. Plot negative drag force versus bead position. This is trap force versus bead-trap offset. Alternately, plotting negative drag force versus negative bead position will yield trap force versus trap-bead offset.

Fourier Analysis

Fourier analysis was performed on all position data along each axis using Equation 8.18 and 8.19 to calculate "in phase" and "out of phase" displacement amplitude, respectively, at a given frequency. Bias and uncertainty in measured amplitude were minimized by truncating a copy of the signal at the largest possible integer number of periods at the frequency of interest, then subtracting the mean position value from all position values. Performing these steps before applying Equation 8.18 and 8.19 was found to reduce bias to negligible levels.

$$\boldsymbol{A_f = \sum_{i=1}^{N} \frac{2}{N} \sin(2\pi f t_i)\, X_i} \tag{8.18}$$

$$\boldsymbol{B_f = -\sum_{i=1}^{N} \frac{2}{N} \cos(2\pi f t_i)\, X_i} \tag{8.19}$$

Tracking Bead Position vs. Time

Beads were identified in the first frame of each video and tracked in subsequent frames using correlation particle tracking modified from the method described by Cheezum *et al*.[22] The major steps are shown in Figure 7.1. Correlation particle tracking involves comparison of image regions containing particles in each frame to the regions containing the same particle in the first frame. Identification in the first frame consisted of stretching

the image contrast, Gaussian blurring using the “imgaussfilt” function in MATLAB with a standard deviation of 1 pixel, and finally identifying contiguous regions above a brightness threshold which met a minimum area criterion. The coordinates of each bead in the first frame were defined as the centroid of the corresponding region.

The pixel arrangement of each bright region was then used to generate a “kernel” used to track bead position in subsequent frames. Each kernel consisted of the arrangement of pixels in the original frame falling within a single region, the frame being unaltered except for subtraction of background brightness. The pixel arrangement was then compared for goodness of match to identically-shaped regions in subsequent frames, from which background brightness had also been subtracted. Goodness of match was defined as C in Equation 8.20. A mesh of C values was calculated for using a range of integer pixel offsets from the original location in both directions, centered on the location of the bead in the first frame. The precise position of a bead in a particular frame was defined as the peak location of a 2D Gaussian fit to the mesh of C values for that frame. Using this technique, the position of each bead was defined in each frame of a video, to a typical precision of better than 10 nm, with the time of each frame known by association with a recording of the camera shutter signal by LabVIEW.

$$\boldsymbol{C} = \sum_{i=1}^{N} \boldsymbol{p}_i \boldsymbol{p}_{i'} \tag{8.20}$$

Figure 8.24: Major conceptual steps in refined correlation particle tracking. First, a small kernel for each detected bead is cut out from the first frame after background brightness is subtracted. Next, that kernel is compared for goodness-of-match (correlation strength) to subsequent frames across a grid of relative position offsets. F

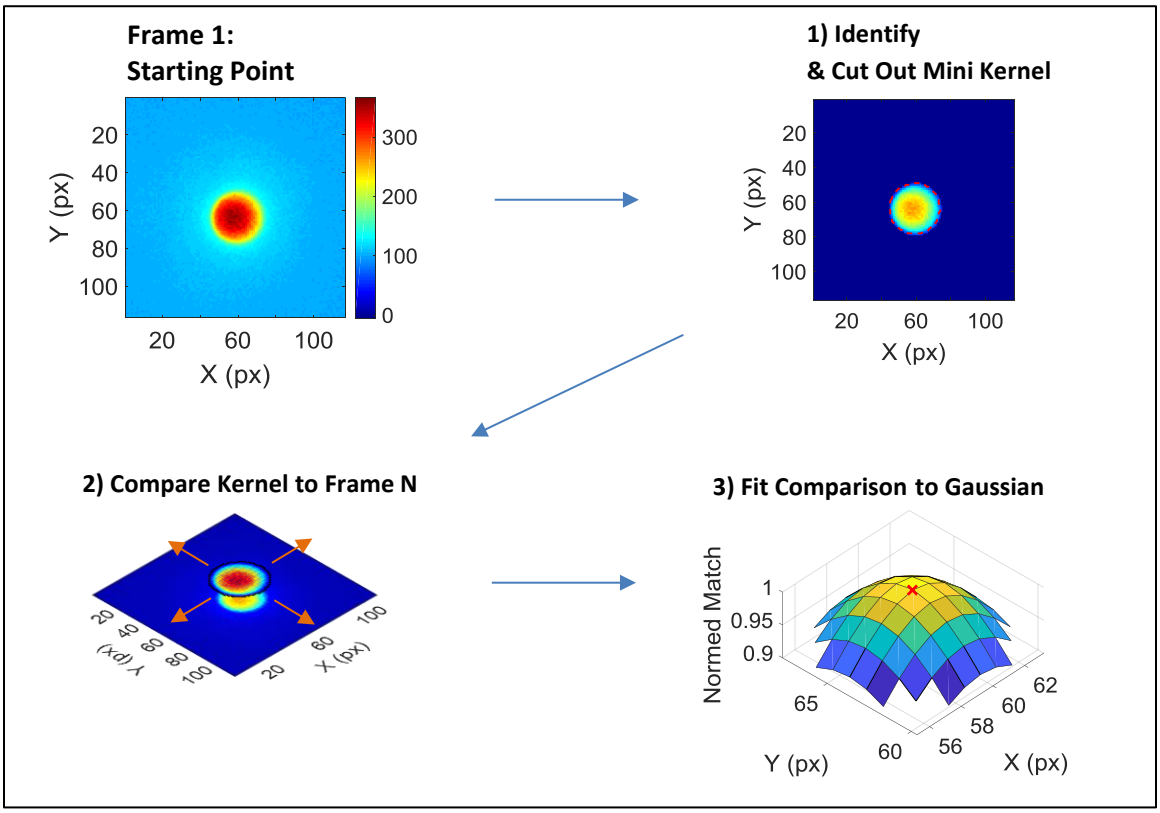

Measuring Amplitude and Phase of Bead Displacements vs. Frequency

The amplitudes of sinusoidal bead displacements in X and Y were calculated separately using Fourier analysis at frequencies spanning from the inverse of the data collection period to the Nyquist frequency defined by the image frame rate. If the exact driving frequency or any harmonics below the Nyquist frequency were not part of the frequency series defined by increments of the data collection period inverse, those frequencies were added to the frequency list for which amplitudes would be calculated. The phase lag of the bead motion with

respect to the commanded laser or stage motion is ϕ in **Equation 13**. These same equations were used to measure displacement amplitudes in frequency spectra ranging the Nyquist frequency down to DC signal. Higher harmonics of the driving frequency were specifically included in the frequency spectra.

$$A_f = \sum_{i=1}^{N} \frac{2}{\mathrm{N}} \sin(2\pi f t_i)\, X_i \tag{10}$$

$$B_f = -\sum_{i=1}^{N} \frac{2}{\mathrm{N}} \cos(2\pi f t_i)\, X_i \tag{11}$$

$$\phi_f = \operatorname{atan}\left(\frac{B_f}{A_f}\right) \tag{12}$$

Statistical Estimation of Displacement Uncertainty via Displacement Frequency Spectra

The noise in displacement amplitude at the driving frequency was taken to be consistent with the noise in frequencies near the driving frequency. To quantify this, the amplitude of each displacement component was measured at frequencies within the ranges 1-1.5 Hz and 2.5-3.46 Hz. These amplitudes were ordered from least to greatest for each displacement component. The noise for the corresponding displacement component was then taken to be the amplitude of the first peak past the 68th percentile mark of the amplitude population, as an estimate of one standard deviation.

Use of Higher Harmonics to Probe Nonlinearity of Bead Displacement vs. Force

For both X and Y displacement of each bead, harmonic ratios were calculated to quantify nonlinearity of the force-displacement response for non-dissipative (elastic) harmonic responses. Harmonic ratios, following the general form of Equation 8.21, measured the signed amplitude A_h of displacement at some harmonic frequency h relative to the signed amplitude of displacement at the fundamental frequency f. Second

harmonics represented beads in which displacement from the resting position was impeded in one direction more than in the other, leading to a smaller, broader peak in one direction and a taller, sharper peak in the other direction. Third harmonics represented a symmetric shortening or extending of the peak displacement with an opposite change in slope near zero displacement. Same-signed third harmonics corresponded to shortened displacement peaks and increased slope near zero displacement. Oppositely signed third harmonics had the opposite correspondence.

The largest third harmonic without being non-physical is 11.1% of the fundamental amplitude, corresponding to infinite material stiffness at peak bead displacement. Larger harmonics would involve bead motion counter to the trend of force displacement, corresponding to negative material stiffness. Only the fundamental response was used in calculating the transmission matrix, and hence in calculating elastic constants. Using a peak displacement with fitted Fourier spectrum amplitudes would result in moduli changing by amplitude approximately equal to H_3. This effect would not explain the observed divergence from unity of G_{1P}/G_{2P}.

$$\boldsymbol{H_{h/f} = A_h/A_f} \tag{8.21}$$

Defining the Transmission Matrix, [T]

Transmission matrices are a novel representation of the relationship between the displacement vector generated at a specific location and a force vector applied to a bead, which is viewed to be at the coordinate system origin. To generate the data required to define that relationship, trials were conducted in which force vectors with a range of orientations were applied to a single driver. For each bead visible during those trials, the displacement was recorded for each trial and paired with the force applied to the driver. The transmission matrices were then generated through linear fits of displacement versus force for each driver-receiver pair, as illustrated in Figure 8.25.

Figure 8.25: Experimental data used to generate element T_{YY} of a force-displacement coupling matrix for a receiver bead. The resulting linear fit is overlaid in red.

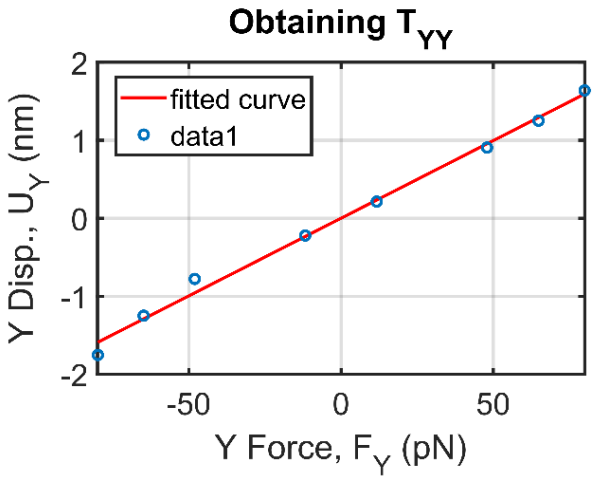

Self-bead transmission matrices, in which the driver was also considered to be the receiver, were calculated in the native coordinate system of the camera. A linear fit of Equation 8.22 was generated for the X component of displacement in each trial versus X and Y force. This was done in MATLAB, which automatically provided an r-squared value and 95% confidence intervals for each fit. An analogous equation was used for displacement along Y. These two fits, in conjunction, defined a transmission matrix $[T]^{DD}$ for the driven bead.

$$\boldsymbol{u_X^D = T_{XX} F_X^D + T_{XY} F_Y^D} \tag{8.22}$$

The r-squared values, obtained by measuring the quality of a linear fit, served as a bound on nonlinearity in the coupling between force and displacement. An r-squared value of at least 0.95 was taken to specify that the coupling was linear or very nearly linear. Decreasing r-squared values would indicate nonlinearity.

Transmission matrices for pairs of beads were generated analogously to those for the driven bead alone, with two major differences. First, the displacement in the equations was that of a bead other than the driven bead. Second, a coordinate system was adopted in which the center of the driven bead at rest was the coordinate system origin and the center of the receiver bead at rest fell along the +X' axis.

The transmission matrix for bead pairs could have been generated in the camera coordinate system, but the coordinate system defined by the bead pair proved to be uniquely intuitive for a mechanical understanding of transmission matrices. With X' corresponding to the direction of $\vec{r}$, the vector from the driven bead to the receiver bead, $T_{X'X}^{RD}$, specified direct coupling, the displacement the receiver would experience along the line connecting the two beads per unit force applied to the driver along that same direction. Similarly $T_{Y'Y}^{RD}$, specified shear coupling, the coupling of force and displacement perpendicular to the vector connecting the two beads. Finally, the off-diagonal elements relate direct force to perpendicular displacement, and perpendicular force to radial displacement. Because an isotropic material only has direct and shear coupling, the magnitude of the off-diagonal elements is a direct indicator of anisotropy in the material mechanically connecting those two beads. In the case that the off-diagonal elements of a transmission matrix could be considered zero for a particular bead pair, the values of the diagonal elements could be directly converted to effective isotropic material elastic constants.

Measuring Anisotropy in [T]

The preferred method for initial quantification of anisotropy in transmission matrices began with a binary filter for isotropy, and followed with definition of anisotropy ratios. The binary test for isotropy was whether zero was within the confidence intervals for off-diagonal elements. If it was, the matrix in question was considered to represent isotropic properties. If not, the matrix was considered to represent anisotropic material properties. The anisotropy ratio, which could be measured even for matrices passing the binary isotropy test, is defined in Equation 8.23. Conceptually, this is the amount of displacement generated perpendicular to the line of force versus parallel to that force when a force is applied directly towards the driven bead. Use of error bounds on the numerator and denominator of an anisotropy ratio would lead to error bounds on the equation as a whole, which confirm the binary results of the binary test for isotropy.

$$\boldsymbol{A_{2P}} = \left(\left(\frac{T_{X'Y'}}{T_{X'Y'}}\right) + \left(\frac{T_{Y'X'}}{T_{Y'Y'}}\right)\right)/\mathbf{2} \tag{8.23}$$

A more relaxed test of isotropy in individual [T] matrices was also used when the conditions of the first test proved stricter than the data could consistently meet. A second variant of **[T]** was generated for bead pairs in the same coordinate system as the generic version, but with off-diagonal elements taken to be zero from the start. This led to radial displacement being fit by Equation 8.24, and an analogous change for fitting of transverse displacement. If the r-squared value for fits of both displacements were at least 0.95, the off-diagonal elements were considered to be zero and the matrix to be isotropic.

$$\boldsymbol{u_R^D = T_{RR} F_R^D} \tag{8.24}$$

Determination of Isotropic Elastic Constants and the Material Stiffness Matrix, [C]

Transmission matrices which passed either of the isotropy tests above were used to directly calculate the isotropic elastic shear modulus, G, and Poisson's ratio, v. These two elastic constants fully defined an effective material stiffness matrix for the region containing the relevant bead pair. G and v were calculated using Equations 8.25-26. The effective elastic stiffness matrix, **[C]**, was then defined by G and v in Equation 8.29.

$$\boldsymbol{\nu_{2P} = \left(\frac{a^2}{3r^2} + 3 - \left(1 - \frac{a^2}{r^2}\right) / \left(\frac{T_{X'X'}}{T_{Y'Y'}} - 1\right)\right) / 4} \tag{8.25}$$

$$\boldsymbol{G = \left(1 - \nu - \frac{a^2}{6r^2}\right) / (4\pi(1-\nu) T_{X'X'} r)} \tag{8.26}$$

$$\boldsymbol{u_R^D = T_{RR} F_R^D} \tag{8.27}$$

$$\boldsymbol{u_R^D = T_{RR} F_R^D} \tag{8.28}$$

$$[\boldsymbol{C}] = \frac{2G}{1-2\nu} \begin{bmatrix} 1-\nu & \nu & \nu & 0 & 0 & 0 \\ \nu & 1-\nu & \nu & 0 & 0 & 0 \\ \nu & \nu & 1-\nu & 0 & 0 & 0 \\ 0 & 0 & 0 & 1-2\nu & 0 & 0 \\ 0 & 0 & 0 & 0 & 1-2\nu & 0 \\ 0 & 0 & 0 & 0 & 0 & 1-2\nu \end{bmatrix} \tag{8.29}$$

Finite Element Models

Bead in a Linearly Elastic Gel with a Soft Sheath Surrounding the Bead

An axisymmetric finite element model was defined in ABAQUS (Dassault Systèmes, Vélizy-Villacoublay) simulating the scenario of a bead encased by a soft sheath in an otherwise homogenous, isotropic, linearly viscoelastic gel. A 2 μm diameter bead was placed at the coordinate system origin, coinciding with the center of a cylinder of material 400 μm long and 400 μm in diameter aligned with the Y axis. Receiver beads were not embedded in the model because receiver beads in the experiments were assumed to displace identically to the corresponding location in an undisturbed gel.

The mechanics of the model were specified to approximate the mechanics observed for optical trap tests in a polyacrylamide gel. The mechanics of the bead approximated the polystyrene of the beads used in experiments with E=3 GPa and ν=0.34. Except for a 0.1, 0.25, or 0.5 μm thick sheath of material surrounding the bead, the cylinder of material had uniform mechanical properties. The sheath surrounding the bead had a Young's modulus of E=15, 30, 150, or 300 Pa and Poisson's ratio of ν=0.495, while the rest of the block had a Young's modulus of 300 Pa and ν=0.495. The circumference of the cylinder was held rigidly, while both ends were free. A 10 pN force was applied to the bead as a body force parallel to the cylinder centerline. G_{1P} and G_{2P} were calculated identically to in experimental data.

Bead in a Linearly Elastic Gel with a Soft Sheath Surrounding the Bead

A FE model was defined similarly to the previous model, but with no sheath and with linearly viscoelastic material properties for the gel bulk. The viscoelastic behavior of the block was defined using a Prony series with G_1=0.2, k_1=0, and τ=0.1 s. A 2 Hz sinusoidal force with amplitude 100 pN was applied to the bead as a body force parallel to the cylinder centerline. Displacement vs time was recorded for the bead and for points

in the gel along the cylinder centerline and along a line perpendicular to that. Phase lag, ϕ, was calculated identically to experimental data.

Imaging Tensile Tests to Determine Macroscopic Poisson's Ratio, ν

Tensile tests were performed in a horizontal custom tensile tester with a water bath. The sample was stretched by displacing one of the grips at a rate of 1 mm/s. A cell phone placed above the tensile tester was used to record video of the test. Visual contrast was enabled by side illumination of the fluorescent beads in the gel and a black electrical tape background in the water bath.

Poisson's ratio was calculated in MATLAB using a linear fit of Equation 8.27 in which ε_x is axial strain of the tensile specimen and ε_y the transverse strain. Both quantities were extracted in each frame of the video relative to the first video frame. The edges of the gage section throughout the video were defined by brightness cutoff values for each edge, set by the operator in the first frame. In each frame, a MATLAB script determined the width of the sample at a preset point near the center of the gage section and at 2-pixel increments in either direction until the width of the sample in that direction was more than 1.3 times the width at the first point measured. The measured length of the sample in each frame was defined as the distance between the midline of each end of the sample, and the width as the mean of all measured widths in the middle 80% of the sample length.

$$\boldsymbol{\nu} = -\boldsymbol{d\varepsilon_y}/\boldsymbol{d\varepsilon_x} \tag{8.30}$$

Parallel Plate Rheometry to Determine Macroscopic Shear Modulus, G

Macroscopic shear modulus was calculated at room temperature using an AR2000 rheometer (TA Instruments, New Castle). Adhesive 600 grit sandpaper (3M, Maplewood) was placed on both the upper and lower plate. Polyacrylamide was allowed to gel between the pieces of sandpaper for 30 minutes before testing. A solvent

trap was placed around the gel during this time to minimize evaporation. When gelation was complete, the rheometer was set to oscillate at 2 Hz with peak strain increasing from 0.001% to 10%. After each sample was tested, the rheometer directly reported shear storage modulus, G', and shear loss modulus, G". The reported shear storage modulus was taken to be G.

Chapter 9 : Modulation of Micromechanics of Collagen Gels by Non-Collagenous Proteins

This chapter is adapted from the following paper:

Yeung, D.*, Gutschick, D.*, Wallace C., Anderson, P.M., Powell, H.M., Lafyatis, G., & Agarwal, G. Modulation of micromechanics of collagen gels by non-collagenous proteins. *In Revision Biophysical Journal. *Co-first authors*

Abstract

Mechanical properties of collagen type 1 networks hold widespread relevance for understanding cellular behaviors. Several matrix proteins are known to modulate the structural and mechanical properties of collagen type 1. In an effort to better understand how the decorin core protein (decoron) modulates the micro-scale mechanical properties of collagen networks, we employed an active optical tweezer micro-rheology approach. We evaluated the coarse-grained mechanical environment between pairs of beads embedded in collagen gels. Inclusion of decoron in the collagen gels led to increased heterogeneity in the matrix environment and an increase in the shear storage modulus. The ability to control the complex collagen micro-mechanical environment by a naturally occurring matrix molecule provides a platform for cell-matrix studies to further understand matrix mechanobiology.

Introduction

Mechanical properties of 3D collagen type I networks have widespread relevance in the field of biomechanics and mechanobiology. Uniaxial and biaxial testing as well as macro-rheology have elucidated how the

mechanical properties of collagen networks (gels) are dependent on several parameters such as the collagen source, concentration, solvent composition, polymerization time, and temperature.[14,79] In recent years, several matrix molecules such glycosaminoglycans (GAGs), proteoglycans and glycoproteins have also been shown to influence the mechanical properties of collagen gels. Matrix molecules, offer an attractive biomimetic approach to modulate the mechanical properties of collagen networks *in vitro* due to their availability as recombinant molecules.

One of the best characterized matrix molecules in this regard is decorin, a proteoglycan widely expressed across various human tissues. Decorin is known to inhibit fusion of collagen fibrils, promote inter-fibril bridges and increase the macro-scale tensile strength of in-vitro generated collagen gels.[80–82] *In vivo* studies have shown how skin and tendon from decorin-deficient mice exhibit increased lateral fusion of collagen fibrils accompanied by a decrease in strength and stiffness of the underlying tissue, as compared to wild type mice.[77,83] In addition, modifying collagen gels with recombinant decorin *in vitro* increased the linear modulus of collagen gels in macroscale uniaxial testing.[81] Similar effects on collagen macro-mechanics have been reported by our group and others when recombinant decoron (core protein of decorin lacking the GAG chains) was employed instead of decorin.[81,84]

While the macro-scale mechanical properties of collagen networks modulated by decoron are well characterized, their micro-scale mechanics are not well understood. This is especially important as local variations in mechanical properties can influence several cellular processes such as cell-matrix interactions, cell migration, differentiation and mechanotransduction events. In this study, we evaluated the micro-mechanical properties of 3D collagen gels created *in vitro* in the presence and absence of decoron. Single beam optical tweezer based micro-rheology was employed to probe the environment around a single particle (bead) (1P) as well as that between pairs of beads (2P) embedded in collagen gels. By utilizing two particle (2P) active micro-rheology approach, we elucidate how micro-scale heterogeneities were enhanced due to decoron. Consistent with earlier macro-mechanical studies, collagen gels containing decoron exhibited increased micro-mechanical

moduli and delayed cell-mediated gel contraction. Modulation of the micromechanical properties by decoron was accompanied by a decrease in the mesh size of the collagen network (assessed using confocal reflectance microscopy). Our study provides novel insights into understanding the 3D collagen network as a homogenous isotropic continuum embedded with local heterogeneities, which could be modulated by matrix molecules.

Table 9.1: Innovations in modulation of micromechanics of collagen gel by non-collagenous proteins.

Innovation	Description	Impact
Quantifying the effect of Non-collagen proteins (NCPs) on shear modulus and Poisson's ratio versus bead separation	NCPs were added to collagen gels with a constant collagen concentration. 1P and 2P data were collected on these gels and examined with respect to bead separation distance.	NCPs are known to alter the fibrillation of collagen gels, which could change mechanical properties and alter structural length scales of the network. Quantification of properties versus length scale can reveal both effects.

Methods

Collagen Gel Fabrication

Collagen solutions (2 mg/ml) were prepared by successive addition of 34.5% phosphate buffer saline (PBS) (7.5 pH), 1% 1N NaOH solution, and 64.5% vol/vol of 3.1 mg/ml bovine dermal collagen type 1 (PureCol from Advanced Biomatrix, San Diego). Collagen gels were also made with or without 0.67 mg/ml of recombinant decoron (a kind gift from FibRx Tissue Repair, Inc., Cambridge, MA) or a control protein, bovine serum albumin (BSA) (Sigma Aldrich, St. Louis) replacing an equal volume of PBS to achieve a protein:collagen ratio of 1:3 w/w.

For micro-rheology measurements 2 μm diameter carboxyl-coated polystyrene microspheres (ThermoFisher) were added to the solution prior to the polymerization process. All components were kept and mixed at 4°C, then pipetted into sterile circular glass molds (a #1.5 precision coverslip with a 20 mm diameter raised well of depth 2 mm), and allowed to polymerize for 24 hours at 37 °C, 5% CO_2, and 95% humidity before testing.

Microrheology

A custom-built single beam optical tweezer instrumentation was employed for active microrheology, as shown in Figure 9.1. Microbeads (of radius: a = 1 μm) embedded in collagen gels were subjected to a sinusoidal force with amplitude $\mathbf{F_i(t)}$ in a direction i, at a frequency of 2Hz using a laser trap with a maximum displacement (Δ) of 500 nm. Effective spring constants of 0.20 pN/nm along X and 0.18 pN/nm along Y were determined from a fit of trap force maps generated from 5000 pairs of bead position and fluid drag force data. The positions $\delta_A(t)$, of the driven bead, A, and $\delta_B(t)$ of the non-driven satellite bead 'B' were monitored by using a correlation method and direct imaging via a CCD camera. The bead displacements $\delta_A(t)$, $\delta_B(t)$ were used to determine A_{2Hz}, the amplitude of the in-phase, 2 Hz, component of the Fourier amplitude spectrum. The maximum bead displacement of the driven (U_i) and satellite bead (u_i) was ascertained from A_{2Hz} of the corresponding beads. Error in satellite bead displacement measurement was estimated as the 68^{th} percentile noise present between 1-1.5 Hz and 2.5-3.46 Hz for a satellite bead and was approximately 0.1 nm. Bead displacement was treated as primarily elastic as the out-of-phase component of the satellite bead displacement was less than 10% of the in-phase amplitude for most satellite beads.

Figure 9.1: The optical trap apparatus, centered on a microscope with a piezo-actuated stage. The laser beam which forms the trap passes through an optical diode, a half-wave plate, and a polarizing beam splitter before being reflected off the two galvanometric steering mirrors, expanded in a telescope, and entering the objective lens. The beam is focused to a waist a few hundred micrometers above the objective lens, where it forms the optical trap. Fluorescense is excited light from a mercury lamp passed through a FITC filter. Imaging is achieved by a CCD camera with filters to pass in only light from bead fluorescence.

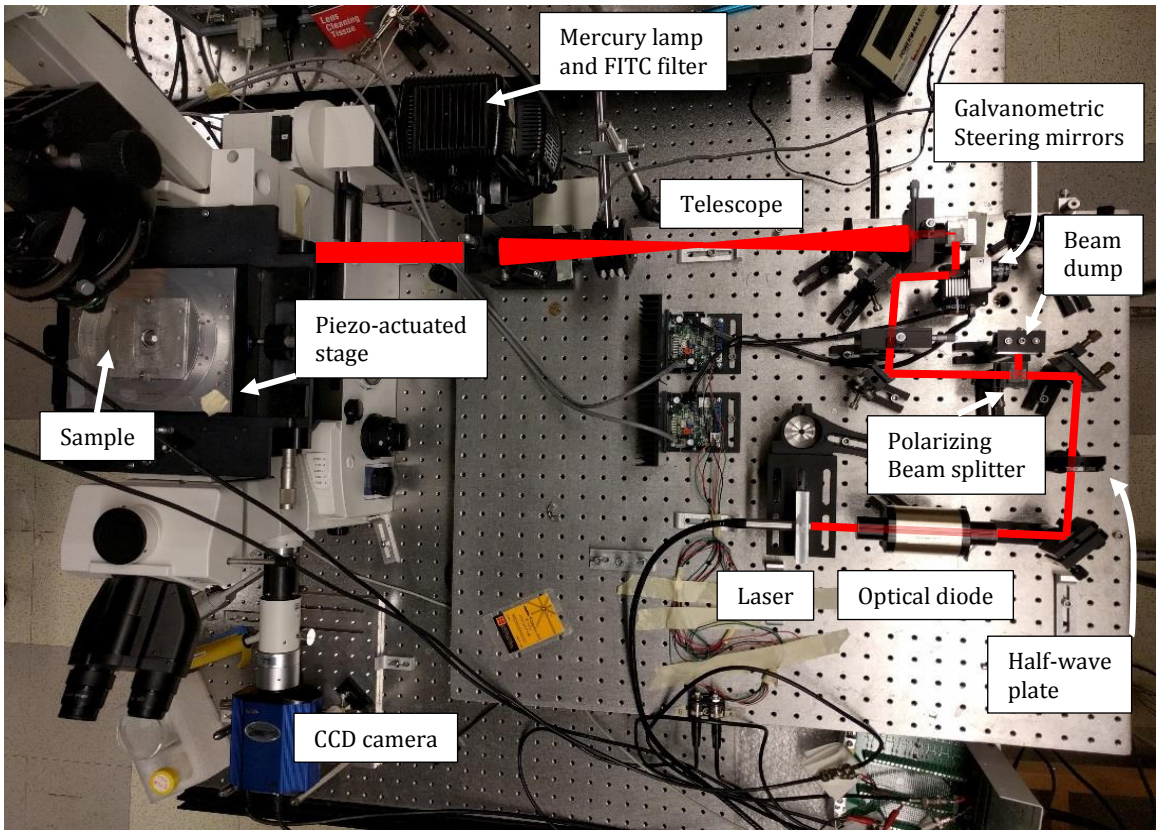

The axis joining the centroids of driven and non-driven bead pair was defined as the vector **r** (Figure 9.2). Each bead was subjected to a sinusoidal oscillation along successive angles by the applied optical tweezer force ($\mathbf{F_{OT}}$). The maximum force (F_i) applied to a driven bead (along a direction *i*) is related to its elastic displacement, U_i in a material by the following equation:

$$\boldsymbol{F_i} = \boldsymbol{F_{OT}} = \boldsymbol{k_{OT}}(\Delta - \boldsymbol{U_i}) \tag{9.1}$$

Figure 9.2: Schematic representing displacement (U: Ux or Uy) of the driven bead, 'A', and the induced displacement (u: ux or uy) of the satellite bead, 'B', separated by a vector r.

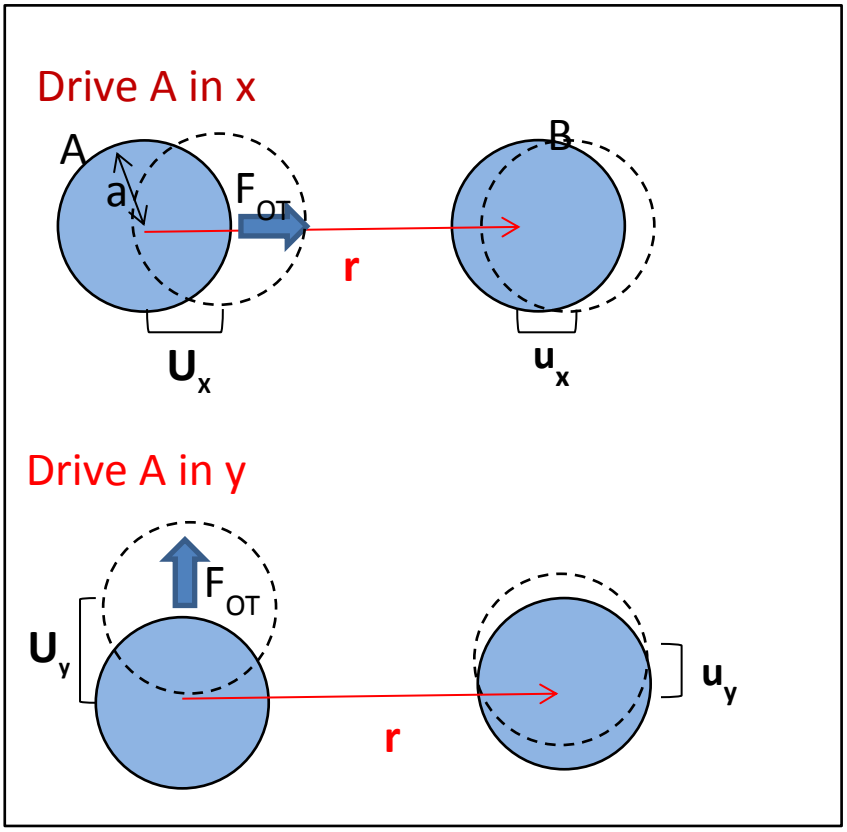

In active two particle (2P) micro-rheology, displacement of the satellite bead (u_i) can be utilized to ascertain the shear storage modulus G between a bead pair AB separated by a distance r, by employing the equation describing the force on a finite sphere (of radius *a*) at the origin of a linear elastic material[85] as follows:

$$u_i = \frac{\left(3-4\nu+\frac{a^2}{3r^2}\right)F_j\delta_{ij}+\left(1-\frac{a^2}{r^2}\right)\frac{(F_j\cdot\bar{r})\bar{r}}{r^2}}{16\pi(1-\nu)Gr} \qquad (9.2)$$

where v is the Poisson's ratio.

For inter-bead distances where, $a^2/r^2 \ll 1$ the displacement field, u_i is expected to show a 1/r dependence for an isotropic homogenous elastic material when normalized with respect to F_i. The Poisson's ratio (v) can be determined from the parallel and transverse components of u_i using equation 9.2.

1P micro-rheology can be regarded as a special case of 2P when $r=a$, and therefore $u_i=U_i$, and the above equation reduces to:

$$\boldsymbol{U_i = F_i \frac{5-6\nu}{24\pi(1-\nu)Ga}} \tag{9.3}$$

G-values ascertained for 1P micro-rheology using equation 9.3 were described using the parameter g.

At least n=8 bead pairs in each sample type were examined using active micro-rheology in parallel (x) and transverse (y) directions to determine U_i and u_i. The distance r between beads in a pair ranged from ~ 3 to 50 µm. For some bead pairs we also evaluated a reciprocal response for storage modulus by switching the role of the driven 'A' and satellite 'B' beads. We calculated a reciprocity index defined as $RI_G = G_{AB}/G_{BA}$ and $R_g=g_A/g_B$.

Confocal Reflectance microscopy

Confocal reflectance microscopy was performed using an incident wavelength of 488 nm on an Olympus FV1000 inverted microscope with a water immersion 40x objective lens with NA 0.8. Stacks of n=26 slices were obtained from each sample with a slice thickness of 1.17 µm. The stacks were processed with an ImageJ plugin, BoneJ, in order to calculate the three dimensional mesh size between the collagen fibrils.[86]

Results

Decoron increases micromechanical heterogeneity in collagen gels

Figure 9.3a shows the displacement (U_x or U_y) of the individual driven beads in the collagen samples. For a fixed laser trap stiffness (k_{OT}) and laser movement (Δ), the optically trapped beads in an isotropic homogenous elastic

material, should all be displaced by a fixed amount in accordance with equation 9.3. However, the scatter in U_i as shown in our data indicates the presence of micro-mechanical heterogeneities in the vicinity of individual beads. This scatter in mean U_i for each bead was quantified by the dimensionless parameter, coefficient of variation (C_v). All collagen samples prepared in PBS, with the control protein BSA or with decoron revealed heterogeneity with C_v between 20 to 25%.

Figure 9.3: Heterogeneity in collagen gels evaluated using (a) displacement (U_i) of driven bead and (b) displacement (u_i/F_i) of the satellite bead as a function of inter-bead distance (r). Solid lines in b indicate power fit of the form $y=ax^b$.

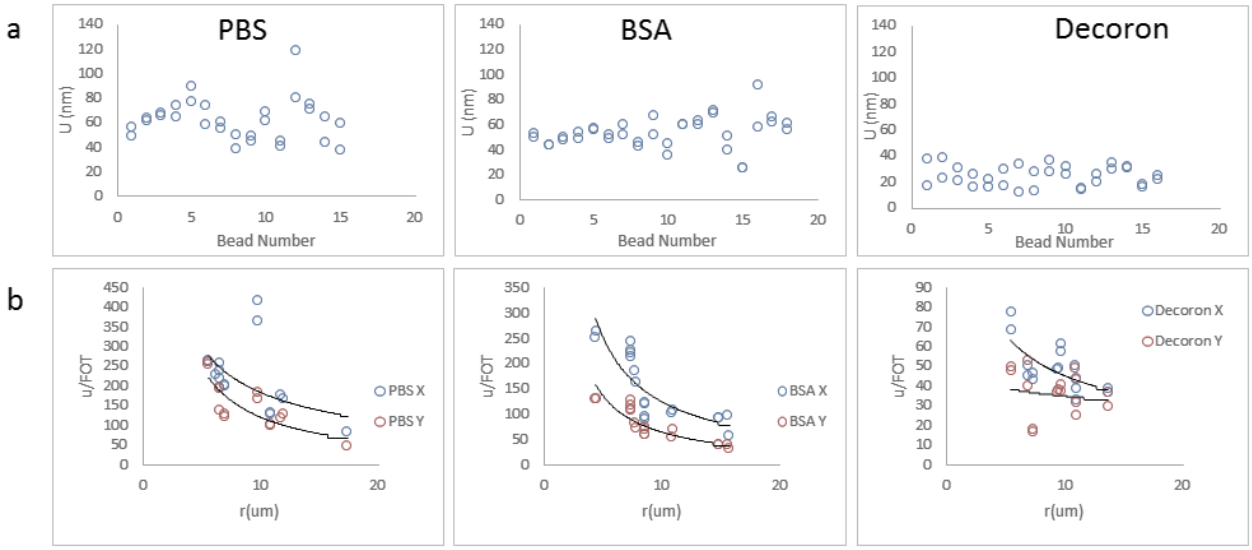

The scatter in driven bead displacement can arise due to (a) heterogeneities in local bead-matrix coupling, or (b) presence of micro-mechanical heterogeneities in the material present in the bead's vicinity. Since analysis of U_i alone fails to reveal the relative contribution of (a) vs. (b), we examined how the effective shear modulus measured using satellite bead displacement depends on bead separation distance, r.

Decoron increases micromoduli of collagen gels

The effective elastic shear moduli (G) were determined for each bead-pair using equation 9.2 for 2P micro-rheology (Figure 9.4). Evaluation of G versus bead separation, as obtained using 2P microrheology, can be used as another measure of micro-mechanical heterogeneities in collagen gels. As seen in Figure 9.4**,** G was dependent on bead separation, r, for all gels studied. The length scale at which the shear modulus became independent of bead separation was different for each chemistry with collagen +BSA reaching a plateau at a bead separation of roughly 2 microns whereas pure collagen and collagen + DDR2 levels off at approximately 4 microns with decoron requiring a bead separation greater than 7 microns before it was independent of bead separation (Figure 9.4).

Figure 9.4: Shear modulus of collagen with and without the addition of non-collagenous proteins. The shear modulus of each gel was dependent on bead separation with the length scale of that dependence varying with gel chemistry.

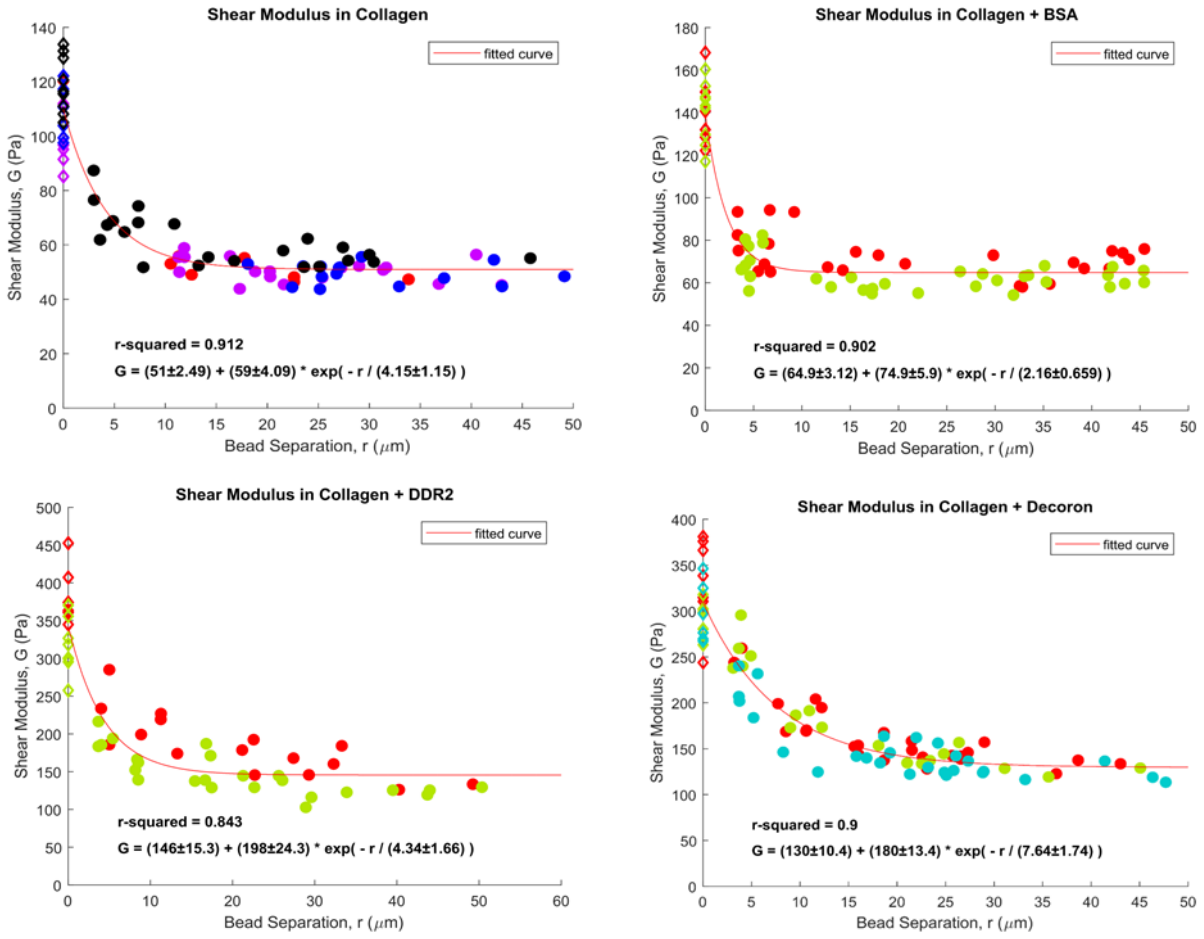

When comparing the relative magnitudes of G across samples, pure collagen gels were the least stiff, while gels with BSA had slightly elevated modulus. However, most strikingly, the average G for gels with decoron or DDR2 was approximately 3 times higher than for pure collagen. To evaluate if the increase in G of collagen gels by decoron or DDR2 was accompanied by changes in its Poisson's ratio (v), we determined v for each bead pair as shown in Figure 9.5**.** The impact of NCPs, and specifically decoron, on Poisson's ratio is not yet understood.

Figure 9.5: Poisson's ratio for pure collagen (PBS) and collagen gels with BSA, DDR2 or decoron additions.

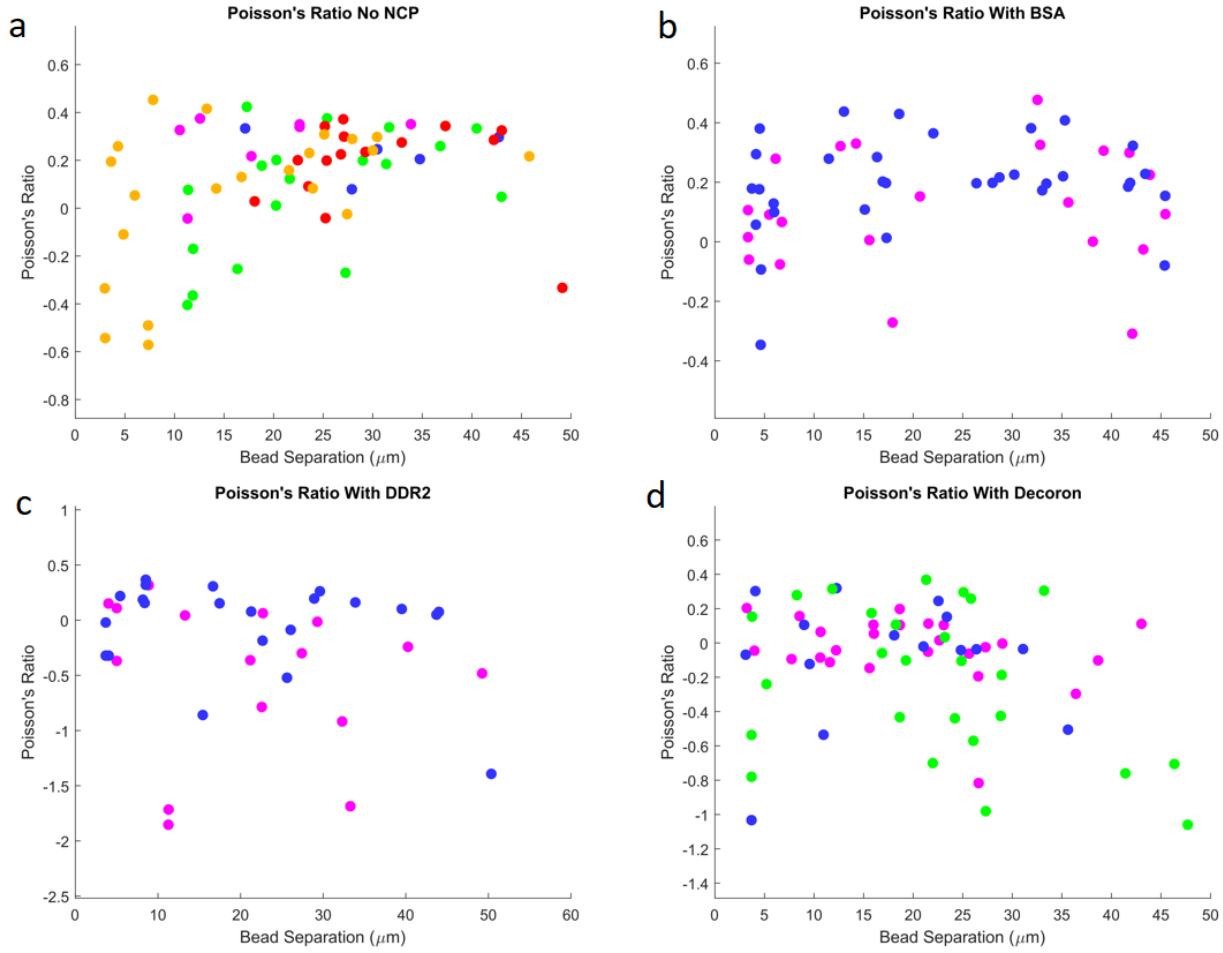

Figure 9.6: Modulus ratio for bead pairs probed in A-B and B-A directions. Modulus ratios of 1 indicate full reciprocity between probing arrangements and increased levels of local homogeneity of structure and mechanics.

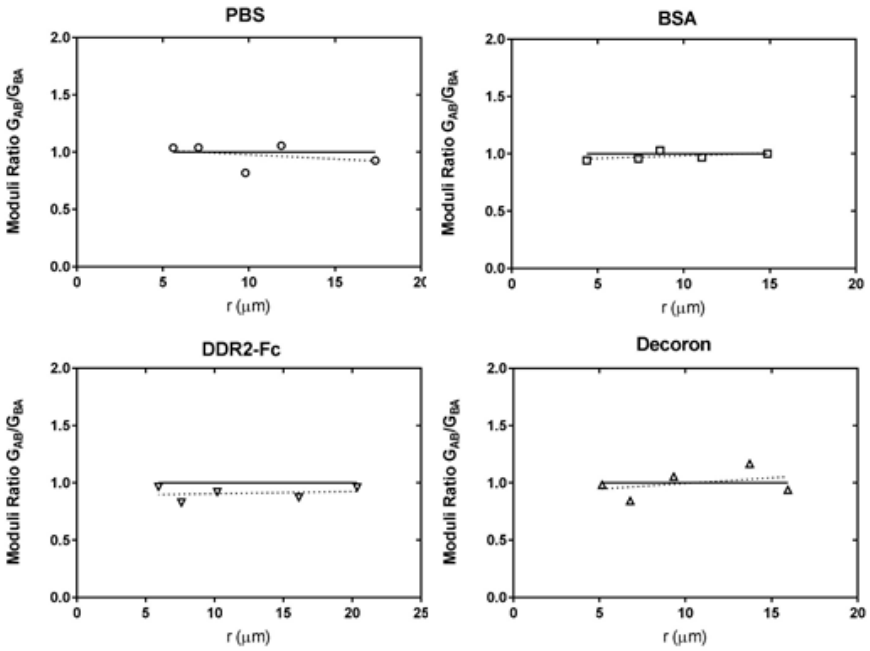

In an effort to examine to what extent G is affected by local bead-matrix coupling, we also compared the reciprocity index (RI) for $G_{AB/BA}$ vs $g_{A/B}$ between bead pairs by switching the role(s) of driven and satellite beads. As seen in Figure 9.6, the RI_G was largely between 0.8 and 1 and was independent of RI_g which varied from 0.5 to 1.5 between beads.

Influence of decoron on collagen microarchitecture and cell-matrix interaction

To evaluate if the increase in micromechanical moduli correlated with structural changes in the collagen network, we examined the collagen gel microarchitecture using confocal reflectance microscopy (Figure 9.7a). As shown in Figure 9.7b, the mesh size of collagen gels was reduced in presence of decoron while BSA showed

no significant change compared to PBS samples. Decoron samples also revealed localized regions of high and low collagen density in agreement with our micromechanical heterogeneity assessments.

Figure 9.7: a) Confocal reflectance microscopy of collagen and collagen + NCP gels. Inset of each picture shows the gel immediately surrounding the bead. B) Quantification of gel structure including intensity distribution, mesh size, and area fraction.

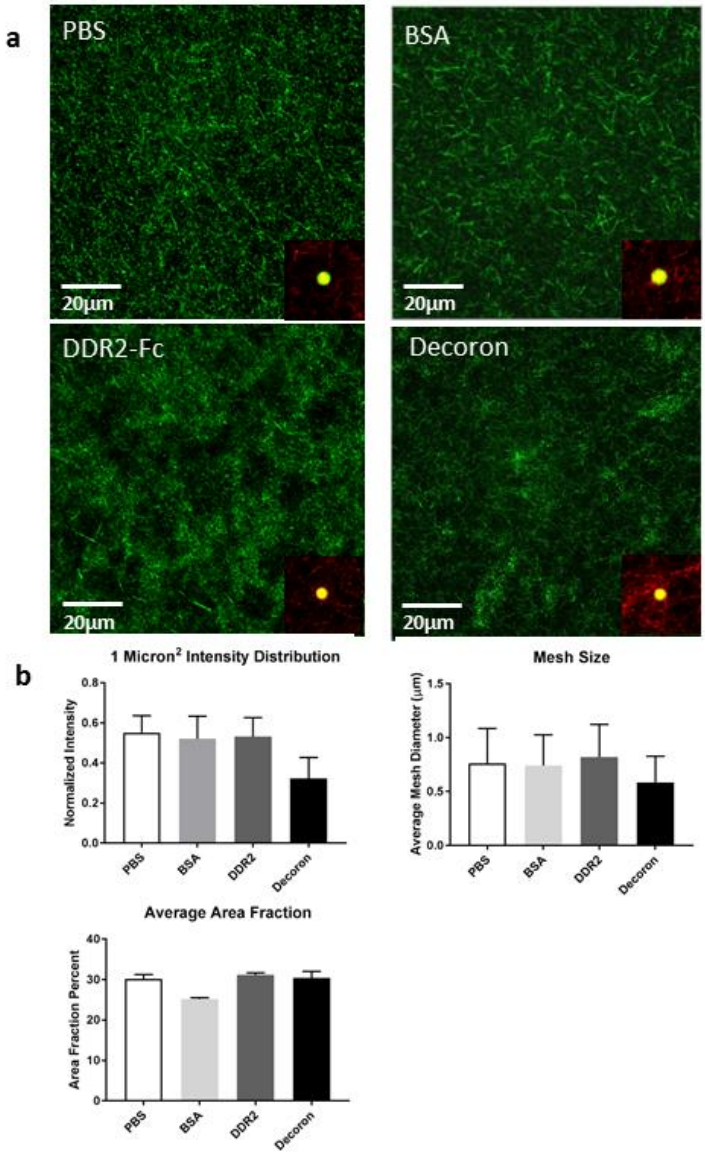

Table 9.2: Summary of findings in modulation of micromechanics of collagen gel by non-collagenous proteins.

Finding	Description	Impact
G has a characteristic decay length scale in 1P+2P data	An exponential curve was fitted against G1P and G2P data and found to have a characteristic length scale with good fit to experimental data.	A smooth curve relating 1P and 2P data connects the two data types in a manner not observed before while the characteristic length scale suggests a corresponding structural length scale. These may have implications for cellular mechanotransduction.
The decay length scale of G is modulated by NCPs	Bovine serum albumin reduced the length scale of G decay and decoron increased the length scale, but any effect from DDR2 was statistically insignificant.	The effects of NCPs on collagen network structure can be observed through length scales of modulus decay. These may have implications for modulating cellular mechanotransduction.
The decay length scale of G is modulated by bead size	The decay length scale of G was shortened by reducing bead diameter from 2 μm to 1 μm in collagen gels containing decoron.	Microrheology data reflects the structure of collagen in a manner that depends on the surface area or volume of the probe used.
BSA, DDR2, and decoron stiffen collagen gels	All three NCPs were found to increase G_{1P} and the plateau value of G_{2P}.	The modulus of collagen gels can be modified in tandem with the length scale of network structure.
Bead surface chemistry was not observed to affect G1P or G2P	Most data was taken using carboxylate-modified beads. A collagen gel containing sulfate-modified beads yielded similar values of G1P and plateau G2P as found with carboxylate-modified beads.	Surface chemistry was not an important factor in microrheology of collagen gels, at least between carboxylate and sulfate modification. Other surface chemistries and/or gel types might interact differently.

Discussion

Micromechanics of collagen gels have thus far been probed using passive or active 1P microrheology. Studies using 1P approaches have yielded a large (sometimes over an order of magnitude) scatter and an overestimation of the storage moduli of the collagen gels.[14,17,30,79,87] Heterogeneities in the local environment

in the vicinity of the beads and bead-matrix coupling effects have been postulated as key factors influencing these 1P measurements.[88] Active and passive 2P micro-rheology approaches offer a significant advantage over 1P micro-rheology as they provide evaluation of the mechanical environment versus the length scale provided by bead separation. This is an extension of the coarse-graining elucidated for multi-particle measurements in actin networks.[11,88] However, limited studies exist on 2P micro-rheology of collagen gels.[89] In this study, we used optical tweezer based active 2P micro-rheology to evaluate the micro-mechanical environment in collagen gels. Our results on comparing G_{macro} (for PBS) with G ascertained using 2P micro-rheology and the reciprocal response between bead-pairs confirm that indeed 2P micro-rheology provides a true measure of coarse grained storage modulus and is independent of local bead-matrix environment. Optical tweezer based 2P active micro-rheology can thus be particularly advantageous to evaluate mechanical properties of precious samples which are limited in availability.

Our 2P micro-rheology approach enabled us to evaluate how DDR2 and decoron modulate the mechanical properties and length scale at which the mechanical properties of a collagen gel reach a plateau. The incorporation of DDR2 and decoron significantly increased the modulus of collagen gels with decoron exhibiting a 3-fold increase in G. The confocal reflectance suggest a smaller structural unit (or mesh size) in tandem with fluctuations in structure over a larger length scale within decoron samples, which was in concert with the rapid plateau of G with increasing bead separation. In prior studies and increase in G was observed in gels with a smaller mesh size. This decrease in mesh size is also consistent with the role of decoron in promoting inter-fibril bridges.[90] In contrast the control BSA only had a minor effect on G, and did not alter the mesh size of collagen gels.

Interestingly, the increase in G by DDR2 and decoron was not accompanied by well-defined changes in its Poisson's ratio, ν. Our 2P micro-rheology furnished a mean value of ν from 0-0.5 across all samples. This estimate of ν is consistent with earlier micro and macro measurements, where ν ranged from 0 to 0.5 for collagen gels.[91–93]

Taken together our results demonstrate that 3D collagen networks can be interpreted as a homogenous materials at large length scale with micro-scale heterogeneities. Collagen binding proteins like DDRs and decoron can impact the shear storage modulus of this network as well as modulate micro-scale heterogeneities. A robust evaluation at the microscale, as presented in our study holds importance to understand the mechanical properties of the complex ECM and how cells perceive their matrix environment.

Chapter 10 : Impact and Future Work

Using the newly developed 2P method, systematic measurements were made of material properties versus bead separation. Novel phenomena were observed in both collagen and PAA gels, and previously discovered phenomena were investigated in ways previously not possible.[13] To the author's knowledge, these were the first such measurements of material properties versus length scale. These novel observations, and the method behind them were only possible with an ensemble of advances in active multi-particle microrheology, some of which are highlighted in Table 10.1.

Table 10.1: Impact of key advances and findings.

Advance or Finding	Impact
Advance: reporting of material properties versus bead separation	The ability to quantify length scale effects in both commonly reported and novel material properties
Advance: trap force landscape mapping and use of large trap displacements	Precise calculations of force at greater force amplitudes than commonly used
Advance: force-displacement coupling matrices	A straightforward representation of the relationship between force and displacement from which material properties can be calculated directly.
Finding: decay of shear modulus versus bead separation with characteristic length scale in collagen gels	This smooth decay is a previously unobserved connection between 1P and 2P data, with potential for informing mechanistic models.
Finding: phase lag increases with bead separation in PAA and collagen gels, modulated by cross-linking in PAA gels	Nonlinear viscoelasticity was uncovered only by examining phase lag versus bead separation, may indicate a novel deformation mechanism.

Establishing a set of apparatus calibrations provided detailed maps of the apparatus response to inputs. In the case of commanded sinusoidal stage displacement, which is used in the calculation of trap force, calibration defined not only the amplitude of the displacement along each axis, but also the amplitude of harmonic components and the time lag of each component. Similarly, commanded trap displacement in 2D was found to be scaled by different amounts along X and Y, to be rotated with respect to the coordinate system of the camera through which all displacements were measured, and to lag the input signal. When making measurements depending on position or velocity of the stage or trap throughout a cycle, apparatus calibrations provided information necessary for accurate results, a fact borne out by improved agreement in shear modulus between large bead separation 2P measurements and macro measurements after thorough apparatus calibration.

Measurement of the trap force was advanced the state of the art calculation of a single spring constant to a landscape.[30] The generation of a detailed map increases precision of force calculations at any displacement and enables use of higher trap forces without compromising the accuracy of force calculations. The ability to precisely know trap force, and to know that force beyond traditional limits, is valuable because every microrheological measurement of material properties depends on the force applied to the driver bead by the trap.

Refinements to correlation bead tracking and displacement measurement increased robustness of tracking near image edges, improved precision and accuracy of amplitudes measured through Fourier analysis of non-ideal signals, and may have improved accuracy over the inherited correlation bead tracking by avoiding correlation of background features, such as out-of-focus beads. Even without these refinements, the baseline method wash shown to have better precision than the most commonly used method.[22] However, improvements were still shown in displacement precision using a tailored, reduced-size kernel for convolution, and the accuracy and precision of the basic explicit Fourier analysis in the inherited method was improved by making minor adjustments to the raw data used. Similar to improvements in trap force measurement,

improvements in displacement measurement are valuable because every microrheological measurement of material properties depends on the displacement of beads in response to force applied by the trap to the driver bead.

Innovations in data collection provide the data to define a relationship between force in 2D and displacement in 2D and enable more precise measurements through larger forces than commonly used and suitability of sinusoidal signals for Fourier analysis. Star driving provides an arbitrarily dense set of X and Y force vector combinations which the resulting bead displacements can be compared against, allowing a 2D relationship between the two quantities to be defined. This includes phase lag and nonlinearity. The use of Fourier analysis was made simple through sinusoidal oscillation of the trap, leading to approximately sinusoidal bead displacements. Fourier analysis can be directly applied to bead displacements to quantify the amplitude, phase, and any nonlinearity of the response to force applied by the trap to the driven bead.

Innovations in data analysis beyond those listed above enabled new insights into material properties. Simultaneous extraction of 1P and 2P data from the same videos allows a comparison and connection to be made between the two data types. Generation of full Fourier spectra with applied force at a single frequency allows quantification of nonlinearity through the amplitude of displacement at harmonics of the driving frequency and also enables estimation of precision through examination of non-harmonic amplitudes. Generation of force-displacement coupling matrices for each driven bead and driver-receiver bead pair specifies the “raw” relationship between force and displacement, and can directly yield material properties such as isotropic elastic shear modulus and Poisson’s ratio, some measure of anisotropy, and even viscoelastic properties such as complex shear modulus or a viscous Poisson’s ratio. Finally, the pairing of all data with the relative position vector between beads allows all material properties to be reported versus bead separation, allowing examination of length scale effects specific to each material. Quantification of force-displacement coupling and material properties versus bead separation has not been performed before to the author’s

knowledge, and the additional insights provided by direct comparison of 1P and 2P data or analysis of nonlinearity add to the novel abilities in the 2P method.

Use of the newly developed 2P method with the advances laid out above has led to observations of novel material properties in PAA and collagen gels. Elastic shear modulus in collagen gels was observed to have a decay well-fitted by an exponential connecting both 1P and 2P data points, with addition of non-collagenous proteins (BSA, DDR2, and decoron), increasing the modulus and altering the characteristic length scale of the exponential decay. Previous studies have found and analyzed differences in shear modulus from single- versus multi- particle measurements, but the smooth connection between the two has never been observed before, to the author's knowledge. A discrepancy in 1P and 2P shear modulus in PAA gels was an unremarkable observation of a long-known phenomenon until third harmonics in driven bead displacement were matched to soft sheaths of specific modulus and thickness, surpassing the abilities of previous studies.[13,16,18,46] Phase lag of bead displacement with respect to trap displacement was observed to increase with bead separation in both PAA and collagen gels. Further study of this phenomenon lead to the observation that higher cross-linking density in PAA gels increased the slope of phase lag versus bead separation, and identified rate-limited fluid flow through the polymer network as a possible mechanism. This host of novel phenomena, which would not have been possible to observe without the advances made in the 2P method, suggest exciting possibilities for further studies.

There are many possible avenues for continued work, both in advancement of the method and in properties to probe. Several are highlighted in Table 10.2. An example of advancing the method would be to combine the data from the 2P method with Z-stack deconvolution or other imaging methods, allowing structural information about the gel surrounding each constellation of beads to be matched with the material properties measured in that location. Combining both advancement of the method and material properties, examination of anisotropy developing in uniaxially stretched collagen gels would be of great interest to the biomedical community but also be best accomplished by development of anisotropic material constant calculations.[63]

Other soft biomaterials, such as fibrin gels, were not studied here but have micromechanical properties which are likely to be viewed with great interest. Returning to advancement of the method, there are many subtle improvements which could be made, such as: direct use of the trap force landscape maps in force calculations, rather than use of an effective spring constant; extension of protocols to quantify the relationships between apparatus inputs and outputs; and theory-informed calculations of measurement uncertainty. The current 2P method has proven capable of many interesting and novel measurements and should be able to make many more novel measurements as-is, but could be made even more illuminating with further advances.

Table 10.2: Remaining topics to continue research on.

Potential topic for further study	Impact
Combine the 2P method with Z-stack deconvolution or other imaging methods	Correlate gel structural information with mechanical properties at the same location.
Measure properties of uniaxially stretched collagen gels	Measure force-displacement coupling in an anisotropic material, providing a practical case for developing methods to quantify anisotropic material properties.
Measure properties of other biomaterials of interest, such as fibrin gels.	Discover new behaviors resulting from different network parameters and fibril properties.
Replace the effective spring constant with force calculated for each bead-trap offset	Increase the accuracy of measurements, specifically with regard to nonlinear material responses.
Develop algorithms to further quantify measurement uncertainty	Provide better error estimates of individual data points.
Develop protocols to further quantify relationship between apparatus/method inputs and outputs	Quantification of possible sources of bias should lead to consistently accurate measurements which can be compared over time and between labs.

References

1. Engler, A. J., Sen, S., Sweeney, H. L. & Discher, D. E. Matrix Elasticity Directs Stem Cell Lineage Specification. *Cell* **126,** 677–689 (2006).

2. Ma, X. *et al.* Fibers in the Extracellular Matrix Enable Long-Range Stress Transmission between Cells. *Biophys. J.* **104,** 1410–1418 (2013).

3. Buxboim, A., Rajagopal, K., Brown, A. E. X. & Discher, D. E. How deeply cells feel: methods for thin gels. *J. Phys. Condens. Matter* **22,** 194116 (2010).

4. Leong, W. S. *et al.* Thickness sensing of hMSCs on collagen gel directs stem cell fate. *Biochem. Biophys. Res. Commun.* **401,** 287–292 (2010).

5. Rudnicki, M. S. *et al.* Nonlinear Strain Stiffening Is Not Sufficient to Explain How Far Cells Can Feel on Fibrous Protein Gels. *Biophys. J.* **105,** 11–20 (2013).

6. Stein, A. M., Vader, D. A., Weitz, D. A. & Sander, L. M. The micromechanics of three-dimensional collagen-I gels. *Complexity* **16,** 22–28 (2011).

7. Wang, H., Nair, A., Chen, C. S., Wells, R. G. & Shenoy, V. B. Long Range Force Transmission in Fibrous Matrices Enabled by Tension-Driven Alignment of Fibers. *ArXiv14096377 Cond-Mat Physicsphysics Q-Bio* (2014).

8. Shi, Q. *et al.* Rapid disorganization of mechanically interacting systems of mammary acini. *Proc. Natl. Acad. Sci.* **111,** 658–663 (2014).

9. Dutov, P., Antipova, O., Varma, S., Orgel, J. P. & Schieber, J. D. Measurement of Elastic Modulus of Collagen Type I Single Fiber. *PloS One* **11,** e0145711–e0145711 (2015).

10. Crick, F. H. C. The physical properties of cytoplasm. A study by means of the magnetic particle method. Part II. Theoretical treatment. *Exp. Cell Res.* **1,** 505–533 (1950).

11. Schmidt, F. G., Ziemann, F. & Sackmann, E. Shear field mapping in actin networks by using magnetic tweezers. *Eur. Biophys. J.* **24,** 348–353 (1996).

12. Shayegan, M. *et al.* Probing multiscale mechanics of collagen with optical tweezers. in **8810,** 88101P-88101P–10 (2013).

13. Levine, A. J. & Lubensky, T. C. Two-point microrheology and the electrostatic analogy. *Phys. Rev. E* **65,** 011501 (2001).

14. Latinovic, O., Hough, L. A. & Daniel Ou-Yang, H. Structural and micromechanical characterization of type I collagen gels. *J. Biomech.* **43,** 500–505 (2010).

15. Parekh, A. & Velegol, D. Collagen Gel Anisotropy Measured by 2-D Laser Trap Microrheometry. *Ann. Biomed. Eng.* **35,** 1231–1246 (2007).

16. Crocker, J. C. *et al.* Two-Point Microrheology of Inhomogeneous Soft Materials. *Phys. Rev. Lett.* **85,** 888–891 (2000).

17. Jones, C. A. R. *et al.* Micromechanics of cellularized biopolymer networks. *Proc. Natl. Acad. Sci.* **112,** E5117–E5122 (2015).

18. Levine, A. J. & Lubensky, T. C. One- and Two-Particle Microrheology. *Phys. Rev. Lett.* **85,** 1774–1777 (2000).

19. Ashkin, A., Dziedzic, J. M., Bjorkholm, J. E. & Chu, S. Observation of a single-beam gradient force optical trap for dielectric particles. *Opt. Lett.* **11,** 288–290 (1986).

20. Ashkin, A. Forces of a single-beam gradient laser trap on a dielectric sphere in the ray optics regime. *Biophys. J.* **61,** 569–582 (1992).

21. Nieminen, T. A. *et al.* Optical tweezers computational toolbox. *J. Opt. Pure Appl. Opt.* **9,** S196 (2007).

22. Cheezum, M. K., Walker, W. F. & Guilford, W. H. Quantitative Comparison of Algorithms for Tracking Single Fluorescent Particles. *Biophys. J.* **81,** 2378–2388 (2001).

23. Crocker, J. C. & Grier, D. G. Methods of Digital Video Microscopy for Colloidal Studies. *J. Colloid Interface Sci.* **179,** 298–310 (1996).

24. Waigh, T. A. Advances in the microrheology of complex fluids. *Rep. Prog. Phys.* **79,** 074601 (2016).

25. Edelstein, A. D. *et al.* Advanced methods of microscope control using μManager software. *J. Biol. Methods* **1,** (2014).

26. Tolić-Nørrelykke, S. F. *et al.* Calibration of optical tweezers with positional detection in the back focal plane. *Rev. Sci. Instrum.* **77,** 103101 (2006).

27. Shayegan, M. Determining local viscoelastic properties of collagen systems using optical tweezers. (Science: Department of Chemistry, 2014).

28. Morphologically open image - MATLAB imopen. Available at: https://www.mathworks.com/help/images/ref/imopen.html?requestedDomain=www.mathworks.com. (Accessed: 14th November 2017)

29. Dasgupta, B. R. & Weitz, D. A. Microrheology of cross-linked polyacrylamide networks. *Phys. Rev. E* **71,** 021504 (2005).

30. Velegol, D. & Lanni, F. Cell Traction Forces on Soft Biomaterials. I. Microrheology of Type I Collagen Gels. *Biophys. J.* **81,** 1786–1792 (2001).

31. Simmons, R. M., Finer, J. T., Chu, S. & Spudich, J. A. Quantitative measurements of force and displacement using an optical trap. *Biophys. J.* **70,** 1813–1822 (1996).

32. K Svoboda & Block, and S. M. Biological Applications of Optical Forces. *Annu. Rev. Biophys. Biomol. Struct.* **23,** 247–285 (1994).

33. Svoboda, K., Mitra, P. P. & Block, S. M. Fluctuation analysis of motor protein movement and single enzyme kinetics. *Proc. Natl. Acad. Sci.* **91,** 11782–11786 (1994).

34. Lim, C. T., Dao, M., Suresh, S., Sow, C. H. & Chew, K. T. Large deformation of living cells using laser traps. *Acta Mater.* **52,** 1837–1845 (2004).

35. Hénon, S., Lenormand, G., Richert, A. & Gallet, F. A New Determination of the Shear Modulus of the Human Erythrocyte Membrane Using Optical Tweezers. *Biophys. J.* **76,** 1145–1151 (1999).

36. Fischer, R. S., Myers, K. A., Gardel, M. L. & Waterman, C. M. Stiffness-controlled three-dimensional extracellular matrices for high-resolution imaging of cell behavior. *Nat. Protoc.* **7,** 2056–2066 (2012).

37. rones. Clipart - Pointing finger by Rones. *openclipart* (2014). Available at: https://openclipart.org/detail/205618/pointing-finger-by-rones. (Accessed: 24th April 2018)

38. TheresaKnott. Clipart - scissors wide open. *openclipart* (2006). Available at: https://openclipart.org/detail/433/scissors-wide-open. (Accessed: 24th April 2018)

39. Sen, S., Engler, A. J. & Discher, D. E. Matrix Strains Induced by Cells: Computing How Far Cells Can Feel. *Cell. Mol. Bioeng.* **2,** 39–48 (2009).

40. Yeung, T. *et al.* Effects of substrate stiffness on cell morphology, cytoskeletal structure, and adhesion. *Cell Motil. Cytoskeleton* **60,** 24–34 (2005).

41. Mason, T. G. Estimating the viscoelastic moduli of complex fluids using the generalized Stokes–Einstein equation. *Rheol. Acta* **39,** 371–378 (2000).

42. Mason, T. G., Ganesan, K., van Zanten, J. H., Wirtz, D. & Kuo, S. C. Particle Tracking Microrheology of Complex Fluids. *Phys. Rev. Lett.* **79,** 3282–3285 (1997).

43. Sonn-Segev, A., Bernheim-Groswasser, A., Diamant, H. & Roichman, Y. Viscoelastic Response of a Complex Fluid at Intermediate Distances. *Phys. Rev. Lett.* **112,** 088301 (2014).

44. Diamant, H. Hydrodynamic interaction in confined geometries. *J. Phys. Soc. Jpn.* **78,** 041002–041002 (2009).

45. Diamant, H. Long-range hydrodynamic response of particulate liquids and liquid-laden solids. *Isr. J. Chem.* **47,** 225–231 (2007).

46. Diamant, H. Response of a polymer network to the motion of a rigid sphere. *Eur. Phys. J. E* **38,** 32 (2015).

47. Atakhorrami, M. *et al.* Correlated fluctuations of microparticles in viscoelastic solutions: Quantitative measurement of material properties by microrheology in the presence of optical traps. *Phys. Rev. E* **73,** 061501 (2006).

48. Lee, M. & Furst, E. Response of a colloidal gel to a microscopic oscillatory strain. *Phys. Rev. E* **77,** 041408 (2008).

49. Boudou, J. & Picart, P. An extended relationship for the characterization of Young's modulus and Poisson's ratio of tunable polyacrylamide gels. *Biorheology* **43,** 721–728 (2006).

50. Arnott, S. *et al.* The agarose double helix and its function in agarose gel structure. *J. Mol. Biol.* **90,** 269–284 (1974).

51. Aymard, P. *et al.* Influence of thermal history on the structural and mechanical properties of agarose gels. *Biopolymers* **59,** 131–144 (2001).

52. Pernodet, N., Maaloum, M. & Tinland, B. Pore size of agarose gels by atomic force microscopy. *ELECTROPHORESIS* **18,** 55–58 (1997).

53. Djabourov, M., Clark, A. H., Rowlands, D. W. & Ross-Murphy, S. B. Small-angle x-ray scattering characterization of agarose sols and gels. *Macromolecules* **22,** 180–188 (1989).

54. Hadi, M. F. & Barocas, V. H. Microscale fiber network alignment affects macroscale failure behavior in simulated collagen tissue analogs. *J. Biomech. Eng.* **135,** (2013).

55. Bhole, A. P. *et al.* Mechanical strain enhances survivability of collagen micronetworks in the presence of collagenase: implications for load-bearing matrix growth and stability. *Philos. Trans. R. Soc. Lond. Math. Phys. Eng. Sci.* **367,** 3339–3362 (2009).

56. Nohava, J., Swain, M. & Eberwein, P. Micromechanical Properties of Polyacrylamide Hydrogels Measured by Spherical Nanoindentation. *Key Eng. Mater.* **606,** 121–124 (2014).

57. Blissett, A. R. *et al.* Regulation of Collagen Fibrillogenesis by Cell-surface Expression of Kinase Dead DDR2. *J. Mol. Biol.* **385,** 902–911 (2009).

58. de Wild, M., Pomp, W. & Koenderink, G. H. Thermal Memory in Self-Assembled Collagen Fibril Networks. *Biophys. J.* **105,** 200–210 (2013).

59. Kuz'menko, V. A. Limiting values of Poisson's ratio. *Strength Mater.* **17,** 1599–1602 (1985).

60. Maaloum, M., Pernodet, N. & Tinland, B. Agarose gel structure using atomic force microscopy: Gel concentration and ionic strength effects. *ELECTROPHORESIS* **19,** 1606–1610 (1998).

61. Normand, V., Lootens, D. L., Amici, E., Plucknett, K. P. & Aymard, P. New Insight into Agarose Gel Mechanical Properties. *Biomacromolecules* **1,** 730–738 (2000).

62. Chang, S.-W., Flynn, B. P., Ruberti, J. W. & Buehler, M. J. Molecular mechanism of force induced stabilization of collagen against enzymatic breakdown. *Biomaterials* **33,** 3852–3859 (2012).

63. Sander, E. A., Stylianopoulos, T., Tranquillo, R. T. & Barocas, V. H. Image-based multiscale modeling predicts tissue-level and network-level fiber reorganization in stretched cell-compacted collagen gels. *Proc. Natl. Acad. Sci.* **106,** 17675–17680 (2009).

64. Hadi, M. F., Sander, E. A. & Barocas, V. H. Multiscale Model Predicts Tissue-Level Failure From Collagen Fiber-Level Damage. *J. Biomech. Eng.* **134,** 091005–091005 (2012).

65. Sander, E. A., Stylianopoulos, T., Tranquillo, R. T. & Barocas, V. H. Image-based biomechanics of collagen-based tissue equivalents. *IEEE Eng. Med. Biol. Mag.* **28,** 10–18 (2009).

66. Aghvami, M., Barocas, V. H. & Sander, E. A. Multiscale Mechanical Simulations of Cell Compacted Collagen Gels. *J. Biomech. Eng.* **135,** 071004–071004 (2013).

67. Chandran, P. L. & Barocas, V. H. Deterministic Material-Based Averaging Theory Model of Collagen Gel Micromechanics. *J. Biomech. Eng.* **129,** 137–147 (2006).

68. Levine, A. J. & Lubensky, T. C. Response function of a sphere in a viscoelastic two-fluid medium. *Phys. Rev. E* **63,** 041510 (2001).

69. Comley, K. & Fleck, N. A. A micromechanical model for the Young's modulus of adipose tissue. *Int. J. Solids Struct.* **47,** 2982–2990 (2010).

70. Pan, Y.-C. & Chou, T.-W. Point Force Solution for an Infinite Transversely Isotropic Solid. *J. Appl. Mech.* **43,** 608–612 (1976).

71. Ting, T. C. *Anisotropic Elasticity: Theory and Applications*. (Oxford University Press, 1996).

72. Legant, W. R. *et al.* Measurement of mechanical tractions exerted by cells in three-dimensional matrices. *Nat. Methods* **7,** 969–971 (2010).

73. Camp, R. J. *et al.* Molecular Mechanochemistry: Low Force Switch Slows Enzymatic Cleavage of Human Type I Collagen Monomer. *J. Am. Chem. Soc.* **133,** 4073–4078 (2011).

74. Abhilash, A. S., Baker, B. M., Trappmann, B., Chen, C. S. & Shenoy, V. B. Remodeling of Fibrous Extracellular Matrices by Contractile Cells: Predictions from Discrete Fiber Network Simulations. *Biophys. J.* **107,** 1829–1840 (2014).

75. Dittmore, A. *et al.* Internal strain drives spontaneous periodic buckling in collagen and regulates remodeling. *Proc. Natl. Acad. Sci.* **113,** 8436–8441 (2016).

76. Bhadriraju, K. *et al.* The relative roles of collagen adhesive receptor DDR2 activation and matrix stiffness on the downregulation of focal adhesion kinase in vascular smooth muscle cells. *Biomaterials* **30,** 6687–6694 (2009).

77. Zhang, G. *et al.* Decorin regulates assembly of collagen fibrils and acquisition of biomechanical properties during tendon development. *J. Cell. Biochem.* **98,** 1436–1449 (2006).

78. Schneider, C. A., Rasband, W. S. & Eliceiri, K. W. NIH Image to ImageJ: 25 years of image analysis. *Nature Methods* (2012). doi:10.1038/nmeth.2089

79. Shayegan, M. & Forde, N. R. Microrheological Characterization of Collagen Systems: From Molecular Solutions to Fibrillar Gels. *PLoS ONE* **8,** e70590 (2013).

80. Raspanti, M. *et al.* Glycosaminoglycans show a specific periodic interaction with type I collagen fibrils. *J. Struct. Biol.* **164,** 134–139 (2008).

81. Reese, S. P., Underwood, C. J. & Weiss, J. A. Effects of decorin proteoglycan on fibrillogenesis, ultrastructure, and mechanics of type I collagen gels. *Matrix Biol.* **32,** 414–423 (2013).

82. Scott, J. E. *et al.* Human Cells Unable to Express Decoron Produced Disorganized Extracellular Matrix Lacking "Shape Modules" (Interfibrillar Proteoglycan Bridges). *Exp. Cell Res.* **243,** 59–66 (1998).

83. Danielson, K. G. *et al.* Targeted Disruption of Decorin Leads to Abnormal Collagen Fibril Morphology and Skin Fragility. *J. Cell Biol.* **136,** 729–743 (1997).

84. Metzler, K. M., Roberts, C. J., Mahmoud, A. M., Agarwal, G. & Liu, J. Ex Vivo Transepithelial Collagen Cross-linking in Porcine and Human Corneas Using Human Decorin Core Protein. *J. Refract. Surg.* **32,** 410–417 (2016).

85. Phan-Thien, N. & Kim, S. *Microstructures in Elastic Media: Principles and Computational Methods*. (Oxford University Press, 1994).

86. Doube, M. *et al.* BoneJ: Free and extensible bone image analysis in ImageJ. *Bone* **47,** 1076–1079 (2010).

87. Leung, L. Y., Tian, D., Brangwynne, C. P., Weitz, D. A. & Tschumperlin, D. J. A new microrheometric approach reveals individual and cooperative roles for TGF-β1 and IL-1β in fibroblast-mediated stiffening of collagen gels. *FASEB J.* **21,** 2064–2073 (2007).

88. Valentine, M. T. *et al.* Colloid Surface Chemistry Critically Affects Multiple Particle Tracking Measurements of Biomaterials. *Biophys. J.* **86,** 4004–4014 (2004).

89. Steinwachs, J. *et al.* Three-dimensional force microscopy of cells in biopolymer networks. *Nat. Methods* **13,** 171–176 (2016).

90. Yang, Y. & Kaufman, L. J. Rheology and Confocal Reflectance Microscopy as Probes of Mechanical Properties and Structure during Collagen and Collagen/Hyaluronan Self-Assembly. *Biophys. J.* **96,** 1566–1585 (2009).

91. Vader, D., Kabla, A., Weitz, D. & Mahadevan, L. Strain-Induced Alignment in Collagen Gels. *PLoS ONE* **4,** e5902 (2009).

92. Tomei, A. A., Boschetti, F., Gervaso, F. & Swartz, M. A. 3D collagen cultures under well-defined dynamic strain: A novel strain device with a porous elastomeric support. *Biotechnol. Bioeng.* **103,** 217–225 (2009).

93. Raub, C. B., Putnam, A. J., Tromberg, B. J. & George, S. C. Predicting bulk mechanical properties of cellularized collagen gels using multiphoton microscopy. *Acta Biomater.* **6,** 4657–4665 (2010).